Solid-state NMR relaxation studies of internal protein dynamics over a wide correlation time range

Dissertation

zur Erlangung des
Doktorgrades der Naturwissenschaften (Dr. rer. nat.)

vorgelegt dem
Institut für Physik
der Naturwissenschaftlichen Fakultät II
der Martin-Luther-Universität Halle-Wittenberg

von
Zinkevich Tatiana
geboren am 10. April 1984 in Kasan (Russland)

Halle/Saale, den 24.03.2014

Gutachter:
Prof. Dr. K. Saalwächter, MLU
Prof. Dr. J. Balbach, MLU
Prof. Dr. B. Luy, KIT Karlsruhe

Table of content

1. Introduction 7

2. State of current research 11

- 2.1. Proteins in different environments: dry and hydrated powders, microcrystalline and solution samples 11
- 2.2. The basics of NMR 13
  - 2.2.1 *Nuclei in magnetic field* 14
- 2.3. Different nuclei in protein NMR investigations 16
- 2.4. Nuclear magnetic interactions 18
  - 2.4.1. *Chemical shift* 18
  - 2.4.2. *Dipolar coupling* 20
  - 2.4.3. *J-coupling* 22
- 2.5. High-resolution techniques in solid-state NMR 23
- 2.6. Solid-state NMR methods essential for the investigation of protein dynamics 25
  - 2.6.1. *Lineshape analysis* 25
  - 2.6.2. *Measurement of motionally averaged dipolar couplings* 26
  - 2.6.3. *Exchange experiments* 26
  - 2.6.4. *Spin-lattice relaxation time in the laboratory and rotating frames* 28
- 2.7. Correlation function and the “model-free” approach 34
- 2.8. Protein dynamics as probed by NMR experiments 38
  - 2.8.1. *Dynamic studies by wide-line NMR spectroscopy* 39
  - 2.8.2. *Proton and deuterium experiments* 39
  - 2.8.3. *Dynamics via low-spectral resolution ssNMR* 40
  - 2.8.4. *Site-specific studies of protein dynamics in the solid-state* 42
  - 2.8.5. *Global fit of site-specific relaxation data* 43

2.8.6. *Probing of millisecond to second motions by exchange NMR spectroscopy* 45

2.8.7. *Concluding remarks* 46

3. The comparison of the hydration response of internal protein dynamics on different time scales 47

3.1. Samples and experimental conditions 48

3.2. The results 49

3.2.1. *Hydration influence on protein spectra* 49

3.2.2. *Relaxation data analysis* 53

3.2.3. *Nanosecond dynamics probed by* $^{13}C\text{-}T_1$ 56

3.2.4. *Microsecond dynamics probed by* $^{13}C\text{-}T_{1\rho}$ 57

3.2.5. *Nanosecond to microsecond protein dynamics probed by* $^{15}N - T_{1,1\rho}$ 58

3.2.6. *Ultra-slow dynamics measured by* ^{15}N *CODEX* 60

3.3. Conclusions 64

4. Microsecond internal molecular motions in fully hydrated microcrystalline proteins studied by relaxation solid-state NMR 66

4.1. Samples and experimental conditions 66

4.2. The results 68

4.2.1. *Relaxation data analysis* 69

4.2.2. *Relaxation rate constants and dynamics* 70

4.2.3. *Correlations* 72

4.3. Conclusions 75

5. General $R_1/R_{1\rho}$ equations in the “model-free” analysis of NMR relaxation data in solids 76

5.1. SPINEVOLUTION simulations 76

5.1.1. *Equation validity* 80

5.1.2. *Limits of applicability* 80

5.2. Conclusions 81

6. Multifrequency quantitative analysis of ^{15}N solid-state relaxation data characterising protein internal dynamics 83

6.1. Experimental data 83

6.2 Data analysis 85

6.3. The fitting strategy 88

6.4. The Akaike Information Criterion (AIC) 89

6.5. Results and discussions 89

6.5.1. *Results of combined data analysis* 89

6.5.2. *Motional amplitudes vs. correlation times and low-amplitude motions* 95

6.5.3. *Alternative minimization protocol* 98

6.5.4. *Dynamics on different timescales* 101

6.5.5. *Detection of slow motion based on the comparison of solution and solid-state derived order parameters* 104

6.6. Conclusions 106

7. Summary 108

Appendix 110

1. *The calculation of z-magnetization of the spin system exposed to the uniform static magnetic field* $\vec{B}_0 = (0,0,B_0)$ 110

2. *The calculation of y-magnetization for the spin system exposed to the uniform static magnetic field* $\vec{B}_0 = (0,0,B_0)$ *and oscillating transverse field* 110

3. *Perturbation theory* 113

4. *Irreducible tensor operators* 113

5. *The comparison of the correlation functions for the "wobbling-in-a-cone" model and the correlation function using the Fuoss-Kirkwood distribution function* 115

6. *Input files for the SPINEVOLUTION simulations of* $T_{1\rho}$ *experiments* 116

a). Input file for the on-resonance ^{15}N-$T_{1\rho}$ relaxation measurements for the CSA mechanism 116 *b)*. Input file for the on-resonance ^{15}N-$T_{1\rho}$ relaxation measurements for the dipolar-coupling mechanism 117

c). Input file for the off-resonance ^{15}N-$T_{1\rho}$ relaxation measurements for the dipolar-coupling mechanism 118

7. *Experimentally measured and simulated relaxation rates and dipolar coupling order parameters with residue resolution* 120

8. *Order parameters and correlation times for "two discrete motions" model.* 124

9. *Order parameters and correlation times for "three discrete motions" model.* 125

10. *Order parameters and correlation times for "two motions with distribution" model* 126

11. *Sum of amplitudes vs. correlation times. "Two motions"* 127

12. *Sum of amplitudes vs. correlation times. "Three motions"* 127

13. *Sum of amplitudes vs. correlation times. "Two motions with distribution"* 128

14. *Limitation of SPINEVOLUTION program* 128

15. *Activation energy limits. Alternative minimization protocol* 129

16. *The RMSD and AIC values table. Alternative minimization protocol* 129

17. *"One motion" dynamic parameters. Alternative minimization protocol* 131

18. *"Two motions" dynamic parameters. Alternative minimization protocol* 132

19. *"Three motions" dynamic parameters. Alternative minimization protocol* 133

20. *"Two motions with distribution" dynamic parameters. Alternative minimization protocol* 134

21. *Final dynamic parameters. Alternative minimization protocol* 135

22. *Sum of amplitudes vs. correlation times. "Two motions". Alternative* 136

minimization protocol
23. *Sum of amplitudes vs. correlation times. "Three motions". Alternative minimization protocol* 136
24. *Sum of amplitudes vs. correlation times. Best fitting results. Alternative minimization protocol* 137
25. *Sum of amplitudes vs. correlation times. "Two motions with distribution". Alternative minimization protocol* 137

Bibliography 138

Eidesstattliche Erklärung 147

Curriculum vitae 148

Acknowledgements 149

List of publications 150

1. Introduction

Proteins are natural organic compounds responsible for many vital processes in organisms. Their diverse and unique functions range from working as chemical catalysts to cell signalling, acting as structural units and providing mechanical properties. A protein molecule consists of many amino acid residues forming a chain, or biopolymer. In contrast to synthetic polymers proteins almost always possess a unique and complex spatial structure. The physical forces that form and preserve specific three-dimensional structures are hydrophobic and electrostatic interactions, hydrogen and disulfide bonds, and the van der Waals interaction. The loss of native structure (denaturation) can result from internal stresses which can include heat, dehydration, freezing, and strong chemical interactions. The loss of structure disables the protein to perform its biological function. Without knowledge of the 3D structures, understanding of how proteins work is hardly possible. Thus, the structural determination of proteins became a key challenge for scientists. Two Nobel Prizes were awarded for the determination of the protein structure one by X-ray analysis (John Kendrew and Max Perutz 1962) and the second by liquid-state NMR (Kurt Wüthrich 2002). A large number of 3D protein structures are now available in the protein data bank (PDB). While structure is a prerequisite for proper function, dynamics are also very important for biological processes. In the native state there is a wide range of internal motions that modulate conformational structure driving functionality.[1–7]

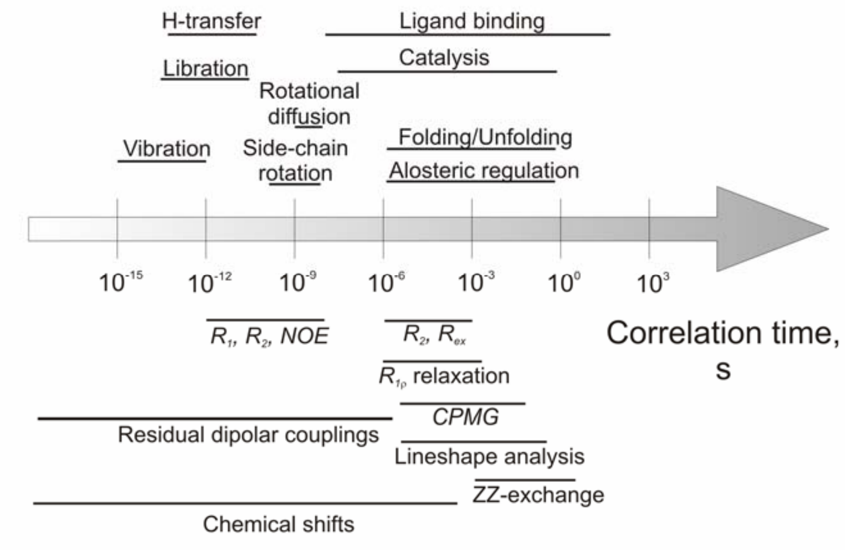
H-transfer
Ligand binding
Libration
Catalysis
Rotational diffusion
Vibration
Side-chain rotation
Folding/Unfolding
Alosteric regulation
10^{-15}
10^{-12}
10^{-9}
10^{-6}
10^{-3}
10^{0}
10^{3}
R_1, R_2, NOE
R_2, R_{ex}
Correlation time, s
$R_{1\rho}$ relaxation
CPMG
Residual dipolar couplings
Lineshape analysis
ZZ-exchange
Chemical shifts

Fig. 1. Protein motions in different timescales and NMR parameters sensitive to them. The origin picture is from Ref. [8].

The timescales of these internal motions are presented in figure 1. The fastest motions occur on the timescale range of picoseconds and even faster. These motions are bond vibrations and librations which rarely extend distances more than 0.5 Å.[9] Nanosecond dynamics typically involve movements of backbone groups and unconstrained side-chain rotation, and have been subject of many investigations. In the μs to s regime there occurs large domain motions. Because the rate of these processes coincide within the same time regime, it is assumed that μs-s dynamics are responsible for protein folding, ligand binding and catalysis.[10,11] Such a broad distribution of motional regimes requires many experimental strategies to investigate all of them. Understanding the specifics (e.g. rates, angles, activation energies) of the entire motional hierarchy would give us a comprehensive picture of how proteins perform their functions. In addition to these internal motions, in solution proteins undergo overall molecular tumbling and translation. Whole molecule tumbling is necessary for accessing the correct orientation for ligand-binding, aggregation and recognition. The timescale of overall tumbling is on the order of nanoseconds, depending on the protein size.

Many groups have investigated internal protein dynamics applying a wide range of experimental approaches to reveal details of mobility on different timescales. These include methods that provide atomic resolution, such as X-ray crystallography and diffraction[9] and nuclear magnetic resonance (NMR) spectroscopy, along with other methods (e.g. Raman, infrared, fluorescence and Mössbauer absorption spectroscopy, neutron scattering) which give information either on probes located in some specific part of the molecule or that detect an ensemble average over the entire molecule. To extract dynamic information from these experimental methods often complicated data analysis must be used. Alternatively, one can use molecular dynamics (MD) simulations which provide the most complete data but are limited in accessing slow motions in large proteins requiring simplifications and approximations.[12,13] Thus, to test the accuracy of simulated data, experimental confirmation is needed which supplies a complete representation of internal motions.[14]

Among all these methods, NMR spectroscopy has particular advantages. The sample preparation is usually non-perturbing to the native state except in cases when isotope enrichment is required. Thus, the dynamical and structural properties and function of the biomolecule are not altered during the experiment. Magnetic nuclei, including ^{1}H, ^{13}C, ^{15}N, are base building-blocks of protein molecules making NMR an ideal experimental approach to explore the entire molecule. Modern NMR techniques can distinguish between signals in the spectra coming from different nuclei. Measuring data for every individual probe provides selective dynamical and structural information. NMR can not only resolve different sites of the molecule, but also offers a number of experimental methods to study dynamics in a wide frequency range (fig. 1). Real-time NMR, performed by the rapid acquisition of NMR spectra, is a powerful and simple approach to detect the dynamics on the order of seconds. ZZ-exchange probes motional processes occurring between conformations in the 10-5000 ms time window. Lineshape analysis is employed to study movements on the micro- and millisecond timescale. To capture motions with correlation times less then 10^{-6} s, relaxation time (T_1, $T_{1\rho}$, T_2) measurements are often used.[7] Although many works employed solution NMR, it has several limitations. For example, there are proteins that are not soluble and, thus, can not be studied in liquid-state experiments. In addition to solubility issues, the molecular mass of the protein can cause poor spectral resolution. While state of the art solution NMR allows for structural determination of heavier proteins, it still remains a restriction. The most fundamental limitation is the presence of overall tumbling of the protein in solution. This whole molecule motion complicates the detection of internal dynamics that happens on the timescale of overall tumbling and slower. Indeed, the overall Brownian tumbling interferes with detecting slow internal protein motions. As a result it is extremely difficult to distinguish between reorientations due to internal motional processes and due to whole molecule rotation. Attempts have been made to increase the overall tumbling rate in order to access these slower dynamics. The two main mechanisms used for this purpose are to increase the viscosity of the solution[15] and employ molecule elongation.[16] Nevertheless, overall tumbling still exists in these samples and “cuts off” all slower motions. An alternative way is to place the molecule in an aligning media.[1,17–21] In the aligning media overall molecule tumbling is no longer isotropic and this provides a possibility to detect slow motions via residual dipolar coupling measurements.[22,23] While this method measures amplitudes of dynamics occurring up to milliseconds, it does not provide the correlation times, and further experiments are needed for a comprehensive picture.

Due to the lack of these complications in solid-state (ss) NMR, it is a promising approach for the purpose of extracting dynamic information. The main drawback of the solid-state NMR used to be the lack of spectral resolution, due to a distribution of fixed molecular orientations creating broad spectral signals, making the resolution of unique resonance lines impossible. With the development of new techniques in ssNMR (such as, magic angle spinning and proton decoupling) this problem was overcome. Now, the resolution of liquid-state NMR can be obtained in solid spectra.[24–29] Furthermore, by measuring in the solid-state, we can access dynamical information via interactions that are averaged in solution NMR. It is also possible to characterise membrane and fibrous proteins in their native conditions by ssNMR. The experimentally measured parameters are free from the influence of the motional fluctuations of the molecule as a whole, opening a way to detect much wider and detailed structural and dynamical information.[30] Thus, modern solid-state NMR combines the advantages of both and can provide a more complete picture of protein dynamics.

The robustness of ssNMR opens the opportunity to solve some specific problems. For instance, we can measure the hydration dependence of motions in a solid protein. The investigation of differently hydrated solid samples makes it possible to study the influence of water on structure and dynamics. This experimental strategy can address important questions, such as: how do internal protein dynamics in dry, hydrated and microcrystalline states coincide with the dynamics in solution; does hydration affect the motions occurring on different timescales; is this influence the same for all regimes, or does each time scale have an unique hydration response? In spite of the large number of the investigations on hydration effects, there is still a lack of detailed information for its influence on the different timescales of motions.

The main aim of this thesis is to investigate internal protein dynamics in different surroundings – lyophilized and hydrated powder samples and in the state of microcrystals. The methods applied during the work provide dynamic information in a wide frequency range starting from picoseconds and up to several microseconds.

After a short description of the protein features in different microsurroundings, I present a brief overview of the NMR basics and the main relevant spin interactions. Then, the implication of these interactions to dynamic studies is discussed. At the end of the second section state of the art ssNMR dynamics for proteins is summarized. The main part of the thesis contains four subsections. In the third part of the thesis I describe the hydration response of internal protein dynamics occurring on different time scales. The applicability of information derived from solid, hydrated samples to explain native motions in proteins is also considered. The fourth part is devoted to investigations of microsecond mobility in a microcrystalline sample with site-specific resolution. The rotary frame relaxation rates were chosen to be a probe of such mobility. The fifth part presents the equations for extracting motional parameters from the raw relaxation rates. These new equations obtained by our group account for the influence of the frequency off-set of spin-lock pulse and comparable values of the MAS and spin-lock frequencies. These equations were validated by simulations with the SPINEVOLUTION[31] program. The last part is dedicated to the quantitative analysis of protein dynamics on timescales from picoseconds to microseconds by means of the global fit of relaxation data.

2. State of current research

2.1. Proteins in different environments: dry and hydrated powders, microcrystalline and solution samples

Water is a native environment for globular proteins. It acts as a matrix and interacts with them in very complex ways. Some proteins use water molecules as structural units, for others they are necessary to mediate interaction with substrate and ligand. In water solutions proteins experience an action of hydrophobic and hydrophilic forces, which form and maintain unique protein structure. These interactions force protein subunits to aggregate in clusters and to form characteristic quaternary structures important for the functionality. Water not only helps the protein to fold into the native structure, but it also weakens interactions between polar protein groups, facilitating vital motions.[32] The notion of water as a lubricant, enhancing protein backbone mobility, is generally accepted, but does not explain all changes occurring upon hydration. The questions concerning hydration processes in biomolecules intrigued scientist to explore the different behaviour of water in the vicinity of the protein versus the bulk.

It has not only been observed that the behaviour of water differs around the protein versus the bulk, but also water molecules surrounding biomacromolecules have different properties. These can be arbitrarily divided in two classes: internal water occupying small polar cavities and clefts, and the surface water molecules forming the hydration shell. The internal water is an integral part of the molecule and has important structural function, while the surface water facilitates dynamics and functionality of proteins.[33–35] At the surface, water has a density which is 10-20% higher than in the bulk. It also was observed that there is a fast exchange between surface and bulk water.[36] The exchange time of water molecules is around several picoseconds. The motions of water molecules in the cavities and clefts are remarkably restricted.[37] Water molecules in deep clefts behave as in the solid state—the time of diffusion out of protein interior reaches microseconds.[38] This is, however, an oversimplified picture, because there is in fact a whole spectrum between “internal” and “external” water.

Another set of interesting questions is how the dynamic and structural properties of proteins depend on different hydration levels ranging from dry to completely hydrated. In this area knowing how much water is necessary for keeping the protein “alive” is an important issue. A large number of papers were devoted to the issue, along with hydrating and dehydrating effects. During freeze-drying proteins progressively lose their water until one finally obtains a sample with a hydration level around zero. The only water that remains is the so-called internal water. The loss of water impairs biological function. Upon dehydration structural distortions in the protein occur. Functional groups in a protein, which interacted with water, now form electrostatic contacts with one another. The protein becomes stabilized with an additional network of interactions and becomes “frozen” in subconformations. The energy barriers between different structural states are high and the protein can hardly overcome them. Thus, in the dehydrated state internal protein dynamics are restricted. Slow motions with a correlation time larger than nanoseconds are significantly hindered and only faster motions are preserved. The diffusive motions of protein domains in dry or slightly hydrated states are characterized by slower correlation times than in the solution.[39] Due to the influence on the structure and dynamics, freeze-drying depresses protein functionality, making the molecule inactive and even denatured.[40]

The hydration (incremental addition of water) of proteins from the dry state to fully hydrated state can be divided into several steps. At hydration levels of around h~0.1-0.2 (h being g of water per g of protein) structural distortions formed during dehydration partially disappear. Water saturates polar and charged sites of proteins lowering energy barriers between subconformations and enabling mobility. This is reflected in an increase of picosecond dynamics and the onset of nanosecond motions.[41] Hydration is most felt by the hydrophilic side chains located on the surface of protein. However, not only do side chains surrounded by water undergo dynamical changes upon the hydration, the hydrophobic core is also sensitive to an increase in water content, reflected by its enhanced dynamics. Even though considerable changes in structure and flexibility of the protein at these hydration levels occur, this amount of water is not enough to restore native dynamics and function[42].

Upon a further increase of the hydration level, the first water shell forms. This shell covers the protein molecule with a monolayer of water, and fast fluctuations between arrangements are close to those in liquid state. At a water content of around 0.4 properties of certain proteins are the same as in solution. It is believed that only slight changes in dynamics and functions take place upon further hydration – additional water only dilutes the system. [41–43] The similarity of properties and dynamics of proteins in fully hydrated states and in solution has been proven by different methods: heat capacity, neutron scattering, EPR and NMR measurements.[42,44–46]

The last issue I would like to discuss here is microcrystalline proteins. It is well-known that the structure in solution and crystals is generally very similar.[47] The same could be said about function: a number of crystalline enzymes are able to “work” with the same efficiency as in water solutions.[48] Water in microcrystalline proteins protects the crystal from collapse and unlocks the electrostatic contacts that appear in dehydrated state. The water content in microcrystals can reach h~0.8,[9,42,49] which is believed to be enough for complete hydration and the occurrence of native-like internal motions on the fast timescale. The contacts that remain between neighbouring molecules restrict the mobility only to the local environment encompassing only a few adjacent atoms. The evidence of liquid-like internal dynamics in protein crystals was suggested by different methods[46,50–52] including NMR spectroscopy.[53–59] It was concluded in these papers that the nanoscale and faster motions are very similar in microcrystalline and solution states, except for motions coming from residues involved in crystal contacts. However, there is insufficient detailed information on longer timescale motions. The reason is a short lifetime for proteins in low-populated excited states. One example investigating μs to ms conformational exchange processes was carried out by Schanda *et al*[60] through Carr-Purcell-Meiboom-Gill relaxation dispersion. They found that the exchange rate in the solid microcrystalline state is slower than in liquids. They attributed this effect to the crystalline environment. This is the only known work where slow motions in solvated and microcrystalline proteins are compared. Thus, there is still deficient information concerning microsecond motions, that should be investigated for complete comparison and a clear picture.

Investigating proteins in the microcrystalline state has certain advantages over studying amorphous powders at different hydration levels. Application of NMR spectroscopy to powders yields broad signals due to the distribution of molecular orientations with respect to the external magnetic field. The incremental water addition reduces the number of protein subconformations and, thus, resonance lines become narrower. However, the spectral resolution in powder samples is far from the one in solution, limiting the observation to certain chemical groups (for example, CH_3, CH_2 and CH groups separately). Unlike powders, microcrystalline proteins have identical microenvironment; thus, there is an opportunity for site-resolved measurements.

The point of my investigation is exploring the dynamics in a wide frequency range occurring in amorphous and microcrystalline systems. There is already evidence that dynamics on different timescales responds differently upon hydration.[41] The hydration response of pico- and nanosecond dynamics has been characterized thoroughly by a variety of methods quite well.[35,43,61,62] There is, however, a lack of information concerning slower motions. The purpose of the work is to expand the breadth of knowledge by exploring these longer timescales.

2.2. The basics of NMR

I will now present the basics of NMR and its application in studying protein dynamics. I will first consider a single spin in a magnetic field, and then the action of an interacting Hamiltonian on the spin system in light of the density matrix. Then, I will briefly discuss the most important interactions that are relevant for studying molecular dynamics in proteins. Here, I will follow a standard treatment of Hamiltonian description in NMR.[63] Finally, I will review the progress of NMR in the investigations of dynamics in biological systems.

2.2.1 *Nuclei in magnetic field*

NMR is a method of investigating matter based on manipulation and measurement of nuclear spins. Spin is an intrinsic property of the nucleus, and can be represented by the spin operator $\hat{\mathrm{I}}$. It defines nuclear magnetic momentum by the equation:

$$\hat{\mu} = \gamma\hbar \cdot \hat{\mathrm{I}} \tag{2.1}$$

here γ is the magnetogyric ratio, which is unique for different nuclear species and $\hbar$ is Planck's constant. The simplest spin system consists of a single isolated spin placed in an uniform and static magnetic field $\vec{B}_0$. In the quantum mechanical picture, the interaction between the spin and magnetic field is described by a Hamiltonian. In the case of a static uniform $\vec{B}_0$ the interacting Hamiltonian is written as:

$$\hat{H}_0 = -\gamma\hbar\,\hat{\mathrm{I}}\,\vec{B}_0 \tag{2.2}$$

Provided that the magnetic field is in the *z*-direction of the Cartesian frame (form of $\vec{B}_0 = \left(0,0,B_z\right)$), the Hamiltonian has a form of:

$$\hat{H}_0 = -\gamma\hbar\hat{I}_z\vec{B}_0 = -\hbar\omega_0\hat{I}_z \tag{2.3}$$

here $\omega_0 = \gamma B_0$ is the Larmor frequency.

Under the influence of $\vec{B}_0$, *z*-magnetization is created. Its magnitude is defined by the difference in the populations of distinct spin states (details in Appendix).

In addition to the static magnetic field, radiofrequency (rf) pulses are usually applied to the spin system, which are describable by a wave $\vec{B}_1\left(t\right)$ that interacts with nuclei. It oscillates perpendicular to *z*-direction at frequency $\omega_1 = \gamma B_1$. Due to the action of this field the state of the spin system becomes time-dependent. It is convenient to operate in a frame rotating about $\vec{B}_0$ with a frequency ω_{rf}. The Hamiltonian of the interaction with an oscillating field directed along *x*-axis of the laboratory frame is:

$$\hat{H}_{rf} = -\gamma\hbar\hat{I}_x B_1 \cos\left(\omega_{rf}t\right) = -\hbar\omega_1\hat{I}_x \cos\left(\omega_{rf}t\right) \tag{2.4}$$

A convenient way to describe the action of interacting Hamiltonians on the spin system is by using the density matrix. We can describe the state of a spin system by a superposition state:

$$\Psi = \sum_{\psi} \sqrt{p_{\psi}}\, \psi \tag{2.5}$$

where p_{ψ} is the probability of being in the state ψ. The possible states of a spin system are in general a combination of a basis set. This set is often represented by Zeeman eigenfunctions for the spin system:

$$\psi = \sum_{i} c_{\psi i} \phi_i \tag{2.6}$$

Then the action of an operator $\hat{A}$ can be written as:

$$\left\langle \hat{A} \right\rangle = \langle \Psi | \hat{A} | \Psi \rangle = \sum_{\psi} p_{\psi} \langle \psi | \hat{A} | \psi \rangle = \sum_{\psi} p_{\psi} \sum_{i,j} c^{*}_{\psi i} c_{\psi j} \langle \phi_i | \hat{A} | \phi_j \rangle \tag{2.7}$$

If we compose the matrix from *ij*-th elements defined as:

$$\rho_{ij} = \sum_{\psi} p_{\psi} c_{\psi j} c^{*}_{\psi i} \tag{2.8}$$

then, we will obtain the density matrix. The corresponding density operator is:

$$\hat{\rho} = \sum_{\psi} p_{\psi} |\psi\rangle\langle\psi| \tag{2.9}$$

The diagonal elements of the density matrix are the average populations of the basis functions. Off-diagonal elements indicate that the superposition state has a mixture of ϕ_i and ϕ_j basis functions. If there is a correlation over time between basis functions (coherence), it will be reflected in non-zero off-diagonal elements.

The density operator of a spin system at thermal equilibrium under the action of the external magnetic field (Eq.(2.3)) is:

$$\hat{\rho}_{eq} = \frac{1}{\mathrm{Tr}\left(e^{-\hat{H}_0/kT}\right)} e^{-\hat{H}_0/kT} \approx \frac{1}{\mathrm{Tr}\left(e^{-\hat{H}_0/kT}\right)} \left(1 + \frac{\hbar\omega_0}{kT} \hat{I}_z\right) \tag{2.10}$$

Here *k* is the Boltzmann constant and *T* is a temperature in K.

Any additional interactions will change the state of the system described by the density matrix. This change can be derived from the Schrödinger equation:

$$\frac{d\hat{\rho}}{dt} = -i\left[\hat{H}, \hat{\rho}\right] \tag{2.11}$$

the solution of which is:

$$\hat{\rho}(t) = e^{-i\hat{H}t}\hat{\rho}(0)e^{i\hat{H}t} \tag{2.12}$$

The result of any NMR experiment accounting for all of the relevant case interactions can be found by determination of the density matrix of the spin system at the desired time point.

The simplest NMR experiment consists of just one on-resonance x-pulse which is applied to the spin system in the external magnetic field. It is useful to calculate the influence of the pulse on the density matrix:

$$\begin{aligned}\hat{\rho}(t) &= e^{i\omega_1\hat{I}_x t}\hat{\rho}(0)e^{-i\omega_1\hat{I}_x t} = e^{i\omega_1\hat{I}_x t}\left(\frac{1}{Z}+\frac{1}{Z}\frac{\hbar\omega_0}{kT}\hat{I}_z\right)e^{-i\omega_1\hat{I}_x t} = \frac{1}{Z}+\frac{1}{Z}\frac{\hbar\omega_0}{kT}e^{i\omega_1\hat{I}_x t}\hat{I}_z e^{-i\omega_1\hat{I}_x t} = \\ &= \frac{1}{Z}+\frac{1}{Z}\frac{\hbar\omega_0}{kT}\left(\hat{I}_z\cos(\omega_1 t)-\hat{I}_y\sin(\omega_1 t)\right)\end{aligned} \tag{2.13}$$

here $Z = \mathrm{Tr}\left(e^{-\hat{H}_0/kT}\right)$. Thus, the y-magnetization is given by:

$$\left\langle \mu_y(t)\right\rangle = \mathrm{Tr}\left(\hat{\mu}_y\hat{\rho}(t)\right) = \gamma\hbar\,\mathrm{Tr}\left(\hat{I}_y\hat{\rho}(t)\right) = -\frac{1}{2}\gamma\hbar\frac{1}{Z}\frac{\omega_0\hbar}{kT}\sin(\omega_1 t) \tag{2.14}$$

If the $\omega_1 t = \frac{\pi}{2}$, then it follows that the magnetization is along y-axis (more details are in Appendix).

2.3. Different nuclei in protein NMR investigations

Before the description of interactions that are important in case of NMR spectroscopy, I would like to discuss advantages and disadvantages of measuring different nuclei in proteins. There are several factors which influence the choice of the probe nucleus. These are: natural abundance, NMR sensitivity, the distribution of chemical shifts, and the location of the probe nucleus. The most often measured nuclei in proteins are ^{1}H, ^{2}H, ^{13}C, and ^{15}N. Sometimes there is also work done on ^{17}O.

The most attractive nuclei in NMR investigation are protons, ^1H. ^1H is found at almost 100% natural abundance and is very sensitive, making experiments on protons fast and easy to perform. However, proton experiments are limited in providing selective information, because there is a large number of protons in the sample. This leads to strongly dipolar coupled proton networks causing considerable line broadening and fast spin-diffusion. Spin diffusion limits the reliability of dynamic information (a more detailed description of the phenomenon is presented below). Another limitation of proton experiments is the narrow chemical shift dispersion which causes overlapping signals of different chemical groups. Thus, protons are rarely measured for selective dynamics, but are important for enhancing the signal of other nuclei (^{13}C, ^{15}N) through cross-polarization in the solid state.

Deuterium is often used in solid state investigations, despite the low natural abundance and narrow chemical shift dispersion. Its advantage is its strong quadrupolar interaction, which is strongly dependent on the molecule orientation. Deuterium measurements are well suited for registering motions with correlation times on the order of $10^{-4} – 10^{-6}$ s via lineshape analysis.

^{13}C nuclei have several advantages which make them convenient for the dynamical studies of proteins, despite the low natural abundance. The chemical shift dispersion is broad, giving well-resolved spectra. Thus, dynamical information can be tracked for every group independently. To overcome the problem of low natural abundance and increase sensitivity ^{13}C isotope doping can be employed.

Nitrogen has the same disadvantage as carbon – its natural abundance is only 0.37%. Isotope enrichment is also often important for ^{15}N experiments. The experiments on ^{15}N combine the advantage of the broad chemical shift dispersion and the convenience of the nuclei locations in the protein chain—almost every amino acid residue bears an amide group. Thus, it is easy to measure residue-resolved dynamical information through relaxation, exchange experiments and lineshape analysis.

The choice of the probe nucleus depends on the information of interest. Of course, making cross-correlations between measurements on different nuclei gives the most complete picture; this can be a very time-consuming strategy and does not necessarily provide new information. The employment of one type of nucleus in a wide variety of different experiments often proves to be a better approach.

2.4. Nuclear magnetic interactions

Up to this point, I have only considered the interaction of the spin system with two types of the magnetic fields, $\vec{B}_0$ and $\vec{B}_1$. However, there are also local magnetic interactions defined by molecular structure and dynamics. The interactions of interest in this work are chemical shift, dipolar coupling and *J*-coupling. These interactions are sensitive to dynamics because of their orientation dependence. Here, I will discuss these interactions in the framework of Hamilton operators.[63]

2.4.1. *Chemical shift*

The nucleus is always surrounded by electrons. The motion of electrons in the external magnetic field $\vec{B}_0$ causes a local magnetic field. This local field shields the nucleus from the external field, and as a result the nucleus feels a slightly different field. The resulting field is strongly dependent on the chemical environment of the nucleus. This is reflected by a difference of Larmor frequencies for different nuclear species seen in an NMR spectrum. The chemical shielding Hamiltonian acting on a spin *I* is:

$$\hat{H}_{CS} = -\gamma \hat{\mathrm{I}} \cdot \underline{\sigma} \cdot \vec{B}_0 \tag{2.15}$$

Here, $\underline{\sigma}$ is the second-rank chemical shielding tensor:

$$\underline{\sigma} = \begin{pmatrix} \sigma_{xx} & \sigma_{xy} & \sigma_{xz} \\ \sigma_{yx} & \sigma_{yy} & \sigma_{yz} \\ \sigma_{zx} & \sigma_{zy} & \sigma_{zz} \end{pmatrix} \tag{2.16}$$

It is convenient to transform the chemical shielding tensor via Euler rotations into the principal axis frame (PAF). In this frame the chemical shift tensor is diagonal, and the numbers along main diagonal of a new tensor are the principal values of the chemical shielding tensor. In NMR spectroscopy instead of these values the isotropic value δ_{iso}, anisotropy Δ_{CS} and asymmetry η_{CS} are often used. These are defined as:

$$\begin{aligned}
\sigma_{iso} &= \frac{1}{3}\left(\sigma_{xx}^{PAF} + \sigma_{yy}^{PAF} + \sigma_{zz}^{PAF}\right) \\
\Delta &= \sigma_{zz}^{PAF} - \sigma_{iso} \\
\eta &= \frac{\sigma_{xx}^{PAF} - \sigma_{yy}^{PAF}}{\Delta}
\end{aligned} \tag{2.17}$$

Practically we do not measure absolute frequencies (ω's) but ones referenced to a standard substance. Thus, it is more convenient to refer to the chemical shift instead of chemical shielding defined as:

$$\begin{aligned}
\delta_{iso} &= \frac{\omega - \omega_{ref}}{\omega_{ref}} \\
\delta_{\alpha\beta} &= \frac{\sigma_{\alpha\beta}\left(ref\right) - \sigma_{\alpha\beta}}{1 - \sigma_{\alpha\beta}}
\end{aligned} \tag{2.18}$$

where $\sigma_{\alpha\beta}$ is the $\alpha\beta$ element of the shielding tensor of the nucleus, and *ref* denotes the reference frequency. Analogously the chemical shift anisotropy and asymmetry can be written as:

$$\begin{aligned}
\Delta_{CS} &= \delta_{11}^{PAF} - \delta_{iso} \\
\eta_{CS} &= \frac{\delta_{33}^{PAF} - \delta_{22}^{PAF}}{\Delta_{CS}}
\end{aligned} \tag{2.19}$$

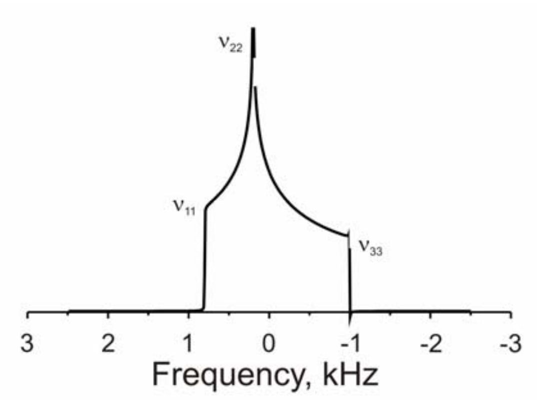

Fig. 2. Simulated CSA powder pattern (simulation performed with SPINEVOLUTION[31] program, $\Delta_{CS} = 1kHz, \eta_{CS} = 0.6$)

From the spectrum we can easily find the principal values δ_{11}^{PAF}, δ_{22}^{PAF}, and δ_{33}^{PAF}.

In solid-state spectra the chemical shift anisotropy leads to appearance of powder patterns (see fig. 2). These arise because different crystallites in powder samples are oriented differently with respect to the external magnetic field. Each orientation contributes one sharp line the superposition of which results in a powder pattern.

The chemical shift anisotropy strongly depends on the presence of molecular motions. If the molecular motion changes the molecule's orientation, then it changes the spectral frequency corresponding to the nucleus as well. Providing the molecular motion is on the appropriate timescale (similar to the width of the powder pattern), distortions in the powder pattern occur. The resultant spectrum contains information about the rate of the motion and its geometry.

2.4.2. *Dipolar coupling*

The dipolar coupling is another important interaction that occurs between two neighbouring nuclear spins. Each nuclear spin possesses magnetic properties and generates a local magnetic field. This local magnetic field influences neighbouring spins which now feel the simultaneous action of external and local fields. Neighbouring spins influence each other equally making the dipolar coupling mutual.

The dipolar Hamiltonian represented as a tensor in the Cartesian frame is written as:

$$\hat{H}_{dd} = -2\,\hat{\mathrm{I}}\cdot\underline{\mathrm{D}}\cdot\hat{\mathrm{S}} \tag{2.20}$$

Here $\underline{\mathrm{D}}$ is the dipolar coupling tensor with principal values *–d*/2, -*d*/2, +*d*. The dipolar coupling constant *d* is calculated by:

$$d = \hbar\frac{\mu_0}{4\pi}\frac{1}{r^3}\gamma_I\gamma_S \tag{2.21}$$

where μ_0 is the vacuum permeability, γ_I and γ_S are magnetogyric ratios of both spins, $\hbar$ is the reduced Planck’s constant and *r* is the distance between spins. $\underline{\mathrm{D}}$ describes how the magnetic field generated by the spin *S* varies according to the orientation of the *I* – *S* internuclear vector. Thus, the strength of the interaction between two spins depends on the internuclear vector orientation with regards to $\vec{B}_0$ and the inter-spin distance. The dipolar coupling tensor is traceless making the isotropic value equal to zero. This tensor is axially symmetric in a frame which has its principal axis along the vector between spins *I* and *S*. Dipolar interaction can either be homonuclear or heteronuclear.

To see the influence of the homonuclear coupling on an NMR spectrum it is better to transform into the rotating frame at Larmor frequency and to use average Hamiltonian theory. In strong magnetic fields, local interactions felt by nucleus are small by comparison. Thus, according to first-order perturbation theory only the secular part of the Hamiltonian persists. The equation describing homonuclear interactions can then be written as:

$$\hat{H}_{dd}^{homo} = -d \cdot \frac{1}{2}\left(3\cos^2\theta - 1\right)\left[3\hat{I}_z\hat{S}_z - \hat{\mathrm{I}}\cdot\hat{\mathrm{S}}\right] \tag{2.22}$$

where θ is the angle between the vector connecting interacting spins and the external magnetic field $\vec{B}_0$ and $\hat{\mathrm{I}}\cdot\hat{\mathrm{S}}=\hat{I}_x\hat{S}_x + \hat{I}_y\hat{S}_y + \hat{I}_z\hat{S}_z$.

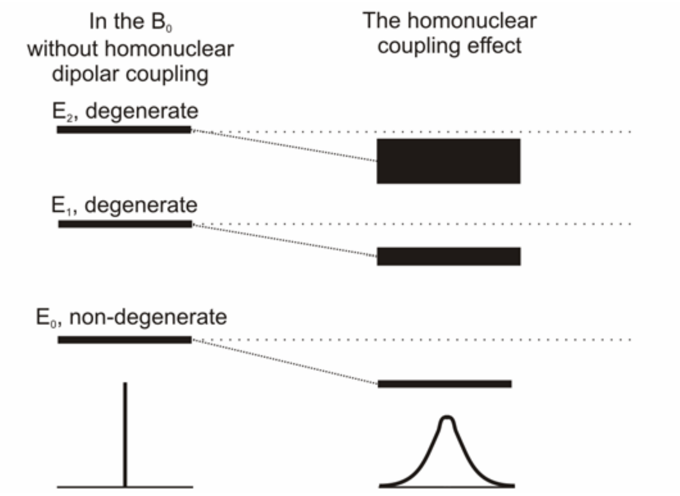
In the B$_0$ without homonuclear dipolar coupling
The homonuclear coupling effect
E$_2$, degenerate
E$_1$, degenerate
E$_0$, non-degenerate

Fig. 3. The effect of homonuclear dipolar coupling on the energy levels of the spin system and ssNMR spectrum.[63] The lowest energy level is non-degenerate, the upper two have different degeneracies

The first term of the equation ($\hat{I}_z\hat{S}_z$) acts on the spin system by shifting the energy of all states. The second term, $\hat{\mathrm{I}}\cdot\hat{\mathrm{S}}$, mixes degenerate Zeeman levels. Thus, the energy of the previously degenerate states are now split, this gives rise to the existence of multiple transition frequencies. This effect is reflected in the broadening of the resonance signal. If the number of spins is sufficient then the Gaussian form of the line appears in the NMR spectrum (Fig. 3).

An important phenomenon that occurs due to homonuclear coupling between neighbouring protons is spin diffusion.[64] This phenomenon is very efficient in a system of strongly coupled protons. The spatially inhomogeneous distribution of *z*-magnetization is equalized by ^{1}H-^{1}H dipolar coupling. Statistically, this can be described by the following: during a period of time neighbouring protons exchange their magnetization. The overall magnetization stays constant but the process leads to the disappearance of an inhomogeneous distribution of the magnetization in the sample. The physics of the phenomenon consist of well known “flip-flop” transitions. If one proton in a pair changes its orientation, then the second orients in the opposite direction to avoid energy loss.

In some cases, spin diffusion can be very useful. For example, it can be used to determine molecular distance of up to 200 nm.[65] However, measuring dynamics of different ^{1}H species becomes complicated because spin diffusion averages all measured dynamic parameters. The rate of spin diffusion strongly depends on the distance between coupled spins and does not contain information about motions.

First-order perturbation theory can be used in the same way for the heteronuclear case. Then the interacting Hamiltonian is given by:

$$\hat{H}_{dd}^{hetero} = -d\left(3\cos^2\theta - 1\right)\hat{I}_z\hat{S}_z \qquad (2.23)$$

The effect of heteronuclear coupling in the spin system is similar to the homonuclear case in that it shifts the energy of the states; however, in contrast, the states do not mix. The lineshape for a spin *I* in a heteronuclear two-spin system is depicted in fig. 4. For a multispin system this interaction broadens the signal line.

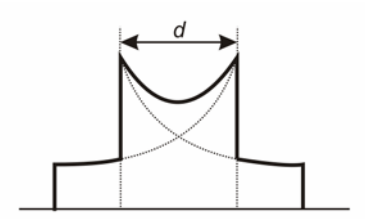

Fig. 4. The form of the spectrum for spin *I* in the heteronuclear two-spin system.[63]

Similar to the case of the CSA, dipolar coupling is affected by internal molecular motions. Changes in the orientation of the internuclear vector can average the apparent dipolar coupling measured by NMR. By comparing of the apparent (motionally averaged) dipolar couplings with the value in the rigid system, it is possible to derive amplitudes (or angles) of motions.

Proton-driven spin diffusion (PDSD) can also occur in the heteronuclear case. This phenomenon is mediated by the coupling of X nuclei to the proton reservoir. In the absence of a ^{1}H network, X nuclei of different groups possess different transition frequencies due to the chemical shift. These differences forbid the process of magnetization transfer. However in the presence of protons a distribution of spectral frequencies exists. These distributions can be so broad that they overlap for different chemical groups. This overlap enables magnetization exchange between nuclei belonging to different groups. PDSD is of great importance in experiments for protein structure determination, however, makes dynamic studies impossible.[20,65–67] Proton-driven spin diffusion distorts relaxation experiments by equalizing the relaxation rates for different sites of the molecule, making the retrieval of site-specific information practically impossible. It also has a significant effect on exchange experiments. If the timescale of the probed motion is the same as speed of the PDSD then it is hard to distinguish between the effects from each other in a resultant NMR exchange spectrum.[68]

2.4.3. *J-coupling*

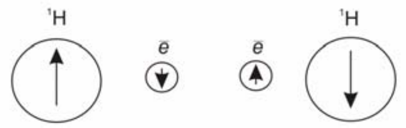

Fig. 5. Illustration to *J*-coupling. Such orientation of the spins corresponds to the low energy of the state.

The last interaction I would like to discuss is *J*-coupling, or the indirect spin-spin coupling. The cause for this interaction arises from the coupling between two nuclei mediated by bonding electrons.[69]

Here I present a simplified model explaining this indirect spin-spin interaction. Let us, first, consider a pair of

J-coupled ^{1}H spins. The preferential orientation of an electron relative to the nucleus, from the energetic point of view, is antiparallel. Thus, the electron orients itself in the opposite direction of the first proton. The Pauli principle dictates that the second electron must be oppositely oriented. The second electron then interacts with the second proton (Fig. 5). In this way, the second proton indirectly "feels" the first proton via bonding electrons. The energy of the system depends on the relative orientation of coupled protons. The Hamiltonian expressing this *J*-coupling has the form:

$$\hat{H}_J = 2\pi \hat{\mathrm{I}} \cdot \underline{\mathrm{J}} \cdot \hat{\mathrm{S}} \tag{2.24}$$

where $\underline{\mathrm{J}}$ is the 3x3 matrix of the *J*-coupling tensor that depends on the molecular orientation. In the liquid state the anisotropy of this interaction is averaged by fast molecular motions. In solids, however, the anisotropy of indirect spin-spin interaction persists. The magnitude of this anisotropy is quite small and is often ignored. Thus, the Hamiltonian of the *J*-interaction is equal to:

$$\hat{H}_J = 2\pi J \hat{\mathrm{I}} \cdot \hat{\mathrm{S}} \tag{2.25}$$

where J is the scalar coupling constant $J = \frac{1}{3}\left(J_{xx} + J_{yy} + J_{zz}\right)$.

In contrast to dipolar couplings, *J*-coupling possesses an isotropic component, which appears in the spectrum.

All described interactions in ssNMR spectroscopy exhibit anisotropy, that is, they have orientation dependence. This dependence is successfully used in dynamic studies, focusing in rotational motions. Measurements of the NMR parameters sensitive to motions can elucidate the details of molecular dynamics. Modern NMR methods can measure different parameters with a high degree of accuracy, providing an abundance of information on dynamics. State of the art NMR provides the possibility to measure residue-resolved information in proteins via these interactions. I will now discuss techniques used to obtain high-resolution in ssNMR.

2.5. High-resolution techniques in solid-state NMR

Now, I would like to discuss the routinely used techniques for the increasing sensitivity and resolution of solid-state NMR spectra. These are: magic angle spinning (MAS), heteronuclear decoupling and cross-polarization. Also I will give some attention to novel high-resolution techniques used in protein ssNMR, such as dynamic nuclear polarization, ultra-high MAS and protein deuteration.

In the liquid NMR the anisotropic parts of the spin interactions are averaged out by fast molecular motion. The idea behind magic angle spinning is basically the same. If we fast rotate a solid sample around a fixed axis tilted at the angle 54.7° relative to the direction of the external magnetic field, then anisotropic (CSA, dipole-dipole) interactions are averaged out. The angle 54.7° is referred to as the “magic angle” which arises from the $\left(1-3\cos^2\theta\right)$ orientation dependence of these interactions. For the effective averaging of the interaction the spinning frequency ω_R should exceed the strength of interaction in frequency units. Cross-polarization enhances the sensitivity of the dilute X spins (^{13}C, ^{15}N). The effect of cross-polarization is based on the magnetization transfer from the abundant (^{1}H) spins to rare X spins via dipolar coupling under the condition of Hartmann-Hahn matching $\gamma_H B_1(^1H)=\gamma_X B_1\left(X\right)\pm n\omega_R$. In ssNMR combining cross-polarization and MAS is often employed with heteronuclear decoupling. High power decoupling breaks the dipolar coupling between rare nuclei and the network of abundant spins (^{1}H) by forcing protons into a different state where they cannot interact with the rare spins. Care should be taken with high power decoupling in protein samples. In addition to the magnetic component of decoupling field used in NMR experiments, an electric component (E) also exists. The electric component causes heating of a protein sample, which can result in denaturation of the protein. Thus, alternative low-power heteronuclear decoupling pulse schemes must be used. Another possibility is using probes with special coils possessing low electric component. New "low-E" probe reduce the amount of heat produced in the sample.[70]

Implementation of these techniques to such complicated systems as proteins is still not enough to obtain high resolution for assignable spectra with good signal-to-noise ratio. Further tricks must be employed. For example, we can take advantage of the high proton sensitivity to detect rare nuclei via indirect detection schemes. Further we can employ homonuclear decoupling[71–74] which can reduce the linewidth to 150-300 Hz. With state of the art MAS (60 kHz) and high NMR fields (1GHz)[75] 200 Hz linewidths are achievable. An alternative technique to provide liquid-state like resolution in microcrystalline proteins is ^{1}H isotope dilution.[24,76–82] This can achieve linewidths around 20 Hz.

One more promising method to enhance the sensitivity of X nuclei is the incorporation of the dynamic nuclear polarization into pulse sequences.[83,84] This method consists of magnetization transfer from electron to nuclear spins through strong coupling between them. This approach provides signal enhancement of around 100-1000. The disadvantage of this method is that it requires low temperatures and specially equipped NMR spectrometers.

2.6. Solid-state NMR methods essential for the investigation of protein dynamics

As was already stated spin interactions (chemical shift and dipole-dipole coupling) in ssNMR are dependent on the orientation of the molecule with respect to the applied magnetic field. The strength of these interactions changes upon molecular motion giving the possibility to use nuclear spin interactions as a probe of dynamics. Employing specifically designed pulse sequences we can choose a particular interaction and monitor its time-dependence. The NMR observables seldom contain direct information about the motions requiring the application of special approach. One way is to perform molecular dynamics simulations and compare these results with observables.

In this section I would like to discuss the following methods for protein dynamic investigations in ssNMR:

a) *lineshape analysis*—where it is possible to register motions through changes in a directly measured anisotropic interaction;
b) *measurements of motionally averaged dipolar coupling* characterising the amplitude of motions faster than the inverse magnitude of the dipolar coupling constant;
c) *exchange experiments* –characterising slow molecular motions by monitoring the time-dependence of the isotropic chemical shift, CSA tensor or dipole-dipole interaction;
d). . $T_1/T_{1\rho}$ *relaxation measurements*—which are sensitive to changes in the magnitude of the heteronuclear dipolar coupling and/or CSA.

2.6.1. *Lineshape analysis*

Lineshape experiments are quite simple. Their pulse sequences consist of only one rf-pulse turning the magnetization to the *xy*-plane, then a spectrum is acquired. The powder patterns in these experiments result as a superposition of signals coming from different crystallite orientations in the sample. The spectral frequency of each nucleus depends on the orientation of its corresponding molecule. If some motion changes the molecule's orientation, then the frequency will also change. This leads to distortions in the powder pattern. Motions detected by lineshape analysis have correlation times less than the inverse width of the powder pattern. Lineshape experiments can be performed statically or under magic angle spinning. The analysis of the powder patterns required the implementation of the lineshape simulations. By comparing results of simulations with those obtained experimentally, it is possible to obtain dynamic information.

One should be aware about some limitations of lineshape analysis. First, as with any method based on fitting experimental data to calculated analytical results, it is hard to select between different models, because fitting quality is often similar. Sometimes, additional measurements can give a hint about which model of the motion is most suitable. However, each fitted model could be a possibility. Moreover, it is likely that in complex systems more than one type of motion exists. Often, the probe nucleus undergoes several motional processes with different geometries on different timescales simultaneously. This significantly complicates the analysis, and sometimes makes it impossible to extract unambiguous information about all types of motions.[63] Even if only one motional regime is inherent for the probe nucleus, the selective labelling or 2D experiments are strongly important. Otherwise signals coming from different groups overlap and make the analysis too ambiguous.

2.6.2. *Measurement of motionally averaged dipolar couplings*

The method that gives direct information about the amplitudes of the motions occurring on timescales up to several microseconds is measuring motionally averaged dipolar couplings. The idea of the method consists of measuring dipolar coupling between directly bonded nuclei and then comparing this value with the value of the rigid-limit. The rigid-limit value is known from the bond length. The ratio between the motionally averaged dipolar coupling and the rigid-limit value gives direct access to the so-called order parameter $\langle S \rangle = D^{exp} / D^{rigid}$. This parameter contains the amplitudes of all the motions occurring with correlation times $\tau_C \ll 1/D^{exp}$. The relationship between the order parameter and the amplitude of motions will be discussed for different models later. There are many different pulse sequences designed to measure heteronuclear dipolar coupling. Some of these are Spin-Echo DOuble Resonance SEDOR,[85] Rotational-Echo DOuble Resonance REDOR,[86] DIPolar chemical SHIFT correlation DIPSHIFT[87].

2.6.3. *Exchange experiments*

Exchange experiments are very important for the investigation of ms-s dynamics in solid proteins. In contrast to liquid-state NMR, where only the exchange between states of different isotropic chemical shifts can be registered, in ssNMR slow reorientation of the CSA tensor[88] and the dipolar coupling[89,90] tensor can also be detected. The basic form of the exchange pulse sequence is presented in Fig. 6. The evolution of magnetization during the encoding period begins after its establishment in the transverse plane. During this encoding period the dephasing of spins occurs under the action of a certain spin hamiltonian (e.g. chemical shift or dipolar coupling). In this time interval a frequency is initially labelled. Then the magnetization is placed along the *z*-direction initializing the second important period – the mixing time τ_m. During this interval, a motional process could occur. If this is the case, then the strength of the probing interaction could change. This is reflected in a change of resonance frequency from the probe nucleus. In the third time interval a second frequency labelling occurs with the recording of the FID (free induction decay) of the signal. Initially, exchange experiments were designed in the 2D fashion, where a two dimensional dataset provided a correlation spectrum. In these spectra, frequencies measured in two time intervals t_1 and t_2 are compared. If the motional process occurs during the mixing time, off-diagonal signals in correlation spectra appear, otherwise, the spectra will contain only diagonal peaks.

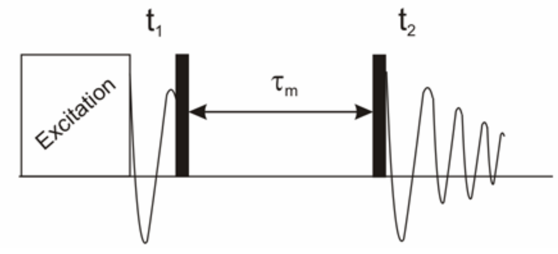

Fig. 6. The scheme of an exchange pulse sequence.[63]

Exchange experiments in solids can be measured under MAS. In these experiments it is important to reintroduce the desired interaction by some pulse train (“recoupling”). Furthermore, the pulses must be synchronized with the period of sample rotation. Otherwise, it would be impossible to distinguish between reorientation due to internal motion and due to sample rotation.

2D exchange experiments are typically time-consuming. Now, there are also 1D versions of the pulse sequences sparing a lot of time and retaining the same dynamic information as the 2D versions (e.g. Centerband-Only Detection of EXchange CODEX[88] and Time-Reverse ODESSA[91]). In 1D exchange experiments a sequence (Fig. 7) of spectra are recorded at different durations of τ_m. The phase cycling is of great importance in these experiments. In the first step we acquire the cosine component of the magnetization during t_1 and t_2. Then secondly we detect the sine component. The resultant signal is:

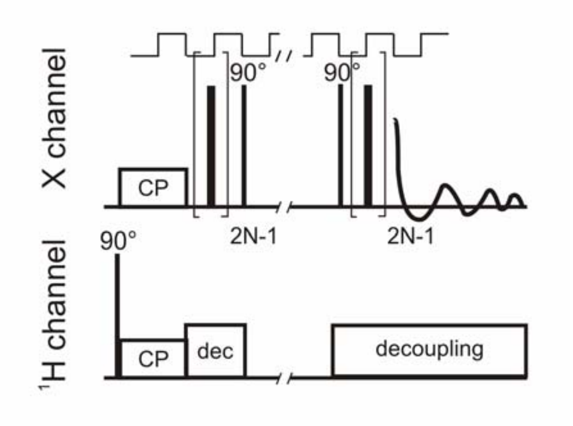

Fig. 7. The schematic representation of the CSA CODEX pulse sequence in 1D fashion under MAS.[88]

$$I \sim I\left(\cos\phi_1 \cos\phi_2 + \sin\phi_1 \sin\phi_2\right) = I\cos\left(\phi_1 - \phi_2\right) \tag{2.26}$$

here ϕ_1 and ϕ_2 are the phases acquired during t_1 and t_2, respectively. The action of motion occurring during the mixing time leads to a disparity of the phases and a loss of signal intensity is observed. Thus, by measuring the signal intensity versus the mixing time we directly obtain the correlation function of motion without any assumptions. The correlation time and amplitude of motion is usually obtained from fitting the experimental decays to an exponential function or combination thereof. Moreover, the number of exchanging sites can be found by measuring at different encoding times, providing a mixing time longer than the correlation time of the motion.

2.6.4. *Spin-lattice relaxation time in the laboratory and rotating frames*

NMR relaxation is a powerful tool for studying molecular dynamics in proteins. Relaxation is reflected in a change of time in a given spin system's density matrix during its return to thermal equilibrium. Longitudinal (spin-lattice) relaxation restores the populations of the Zeeman levels determined by the Boltzmann distribution through the interaction with the spin lattice. Spin-spin (transverse) relaxation describes the rate of dephasing for the spin system in the plane perpendicular to the static magnetic field. This phenomenon arises due to loss of the coherence via energy exchange between spins. For our measurements, relaxation is mainly governed by fluctuating magnetic fields as a result of local molecular motions. By studying relaxation behaviour we can monitor molecular dynamics.

I will now describe spin-lattice relaxation in the frame of Hamiltonians.[92–95] To calculate the rate of spin-lattice relaxation it is necessary to solve the equation that describes the evolution of the density matrix under a certain Hamiltonian:

$$\frac{d\hat{\rho}}{dt} = -\int_0^\infty \left[\hat{H}(t), \left[\hat{H}(t+\tau), \rho\right]\right] d\tau \tag{2.27}$$

A Hamiltonian acting on the system in the laboratory frame can be written as:

$$\hat{H}(t) = \hat{H}_0 + \hat{H}_1(t) + \hat{H}_{SL}(t) \tag{2.28}$$

here, H_0 represents the Zeeman interaction, $H_1(t)$ is the interaction with the applied rf field, and H_{SL} is the interaction of the spin system with the lattice, which contains the motional contribution.

Now, I will consider the case when spin-lattice relaxation is governed by heteronuclear dipolar coupling between spins *I* and *S*. The Hamiltonian of Eq. (2.28) transforms into:

$$\hat{H}(t) = \omega_I \hat{I}_Z + \omega_S \hat{S}_Z + \omega_1 \hat{I}_x \cos\omega t + \hat{H}_{IS}(t) \tag{2.29}$$

We are not obliged to use spin operators to express the Hamiltonians. The other possibility is to use spherical tensor operators (details in Appendix). The heteronuclear Hamiltonian in terms of irreducible spherical tensor operators $\hat{T}_{2q}$ is given by:

$$\hat{H}_{IS} = -\sqrt{6}\frac{\hbar\gamma_I\gamma_S}{r^3}\sum_{q=-2}^{2}(-1)^q \tilde{D}^{(2)}_{0,-q}\left(\Omega_{PL}(t)\right)\hat{T}_{2q}\left(\hat{\mathrm{I}},\hat{\mathrm{S}}\right) \tag{2.30}$$

We separate for convenience random motion and MAS by introduction of transformations: "the principal axis frame→ the rotor frame" (PR) and "the rotor frame→ the laboratory frame" (RL). Mathematically it can be written by the combination of Wigner matrix elements:

$$\tilde{D}^{(2)}_{0,q}\left(\Omega_{PL}\right) = \sum_{n=-2}^{2} D^{(2)}_{0,n}\left(\Omega_{PR}\right) D^{(2)}_{q,n}\left(\Omega_{RL}\right) \tag{2.31}$$

Equation (2.31) describes the time dependence of the spatial part of the Hamiltonian. Ω_{PR}, which defines the orientation of the internuclear vector and its possible random changes. Ω_{RL} specifies the sample rotation due to MAS. $D^{(2)}_{nq}$ are the Wigner rotation matrix elements. The rf field influences spin *I* only. Thus, the equation (2.30) can be rewritten as:

$$\hat{H}_{IS} = -\sqrt{6}\frac{\hbar\gamma_I\gamma_S}{r^3}\sum_{p,q=-1}^{1}(-1)^{p+q}\left\langle 11pq\middle|2(p+q)\right\rangle \tilde{D}^{(2)}_{0,-(p+q)}\left(\Omega_{PL}(t)\right)\hat{T}_{1p}\left(\hat{\mathrm{I}}\right)\hat{T}_{1q}\left(\hat{\mathrm{S}}\right) \tag{2.32}$$

$\left\langle 11pq\middle|2(p+q)\right\rangle$ are the Clebsch-Gordan coefficients. Now, a transformation to the frame where only the heteronuclear Hamiltonian is considered, is convenient. This transformation results in:

$$\tilde{\hat{H}} = \hat{U}\hat{H}\hat{U}^{-1} + i\left[\frac{\partial}{\partial t}\hat{U}\right]\hat{U}^{-1} \tag{2.33}$$

The operator $\hat{U}$ is a sequence of the rotations in spin space. After these transformations we end up with a heteronuclear Hamiltonian as follows:

$$\begin{aligned}\hat{\tilde{H}}_{IS}(t) = \hat{U}\hat{\tilde{H}}_{SL}(t)\hat{U}^{-1} = -\sqrt{6}\frac{\hbar\gamma_S\gamma_I}{r^3}\cdot \\ \cdot\sum_{p,q=-1}^{1}(-1)^{p+q}\left\langle 11pq\middle|2(p+q)\right\rangle D^{(2)}_{0,-(p+q)}\left(\Omega_{PL}(t)\right)\hat{\tilde{T}}_{1,p}\left(\hat{\mathrm{I}}\right)\hat{\tilde{T}}_{1,q}\left(\hat{\mathrm{S}}\right)\end{aligned} \tag{2.34}$$

And for the density operator the equation in this frame is given by:

$$\frac{d\tilde{\rho}}{dt} = -\int_0^{\infty} \left[\hat{\tilde{H}}_{IS}(t), \left[\hat{\tilde{H}}_{IS}(t+\tau), \hat{\tilde{\rho}} \right] \right] d\tau \tag{2.35}$$

The equation (2.35) can be used to calculate relaxation rates. An analogous treatment can be used in the case for relaxation governed by the chemical shift. This mechanism becomes increasingly important at high magnetic fields.

After solving Eq. (2.35) with Eq. (2.34) the spin lattice relaxation rate can be written as:

$$\begin{aligned} R_1 = \frac{1}{T_1} = \frac{1}{10} \left(\frac{\mu_0}{4\pi} \frac{\gamma_I \gamma_S \hbar}{r_{IS}^3} \right)^2 \left\{ J_0(\omega_I - \omega_S) + 3J_1(\omega_S) + 6J_2(\omega_I + \omega_S) \right\} + \\ + \frac{2}{15} \left(\omega_S (\Delta_{CS}) \right)^2 J_1(\omega_S) \end{aligned} \tag{2.36}$$

where $J_{0,1,2}(\omega)$ are the spectral density functions of the order 0, 1, 2, ω_I and ω_S are the angular resonance frequencies of I and S nuclei, respectively, and Δ_{CS} is the chemical shift anisotropy. Spectral density functions come from the application of equation (2.35) to the heteronuclear Hamiltonian and are defined as follows:

$$J_n(\omega) = \int_{-\infty}^{\infty} \left\langle D_{o,n}^{(2)}(\Omega_{PR}(t)) D_{0,-n}^{(2)}(\Omega_{PR}(t+\tau)) \right\rangle d\tau = \int_{-\infty}^{\infty} C_n(t) e^{-i\omega\tau} d\tau \tag{2.37}$$

The angular brackets denote the ensemble average.

Thus, the spectral density function is the Fourier-transformation of the correlation function $C_n(t)$. In the next section, I will explicitly address the correlation function.

The abovementioned treatment is also used for calculating the relaxation rate in the rotating frame. Relaxation in the rotating frame is mainly due to heteronuclear dipolar coupling:[96]

$$R_{1\rho} = \frac{1}{T_{1\rho}} = \frac{1}{20} \left(\frac{\mu_0}{4\pi} \frac{\hbar \gamma_I \gamma_S}{r_{IS}^3} \right)^2 \left(4J(\omega_e) + J(\omega_I - \omega_S) + 3J(\omega_I) + 6J(\omega_S) + 6J(\omega_I + \omega_S) \right) \tag{2.38}$$

Equation (2.38) does not take into account the possible resonance off-set, which can be very important, and arbitrary values of the spin-lock pulse frequency ω_e and MAS frequency ω_R. New formulae for the relaxation caused by dipolar coupling and CSA which account for these complications were derived by our group according to the same approach. For the heteronuclear dipolar couplings mechanism it can be written as:

$$
\begin{aligned}
R_{1\rho}^{IS} &= R_1^{IS} + \sin^2\beta_\rho\left(R_{1\Delta}^{IS} - \frac{1}{2}R_1^{IS}\right)\\
R_1^{IS} &= \mu_S{}^2\left(J_0\left(\omega_I-\omega_S\right)+3J_1\left(\omega_I\right)+6J_2\left(\omega_I+\omega_S\right)\right)\\
R_{1\Delta}^{IS} &= \mu_S{}^2\left(3J_1\left(\omega_S\right)+\frac{2}{3}\sum_{\substack{n=-2\\ n\neq 0}}^{2}\frac{1}{|n|}J_0\left(\omega_e+n\omega_R\right)\right)
\end{aligned}
\tag{2.39}
$$

where β_ρ is an angle between B_0 and the effective spin-lock field B_{1e}, $\mu_S=\frac{\hbar\gamma_I\gamma_S}{r^3}\sqrt{\frac{S(S+1)}{3}}$ (γ_I and γ_S magnetogyric ratios of the interacting *I* and *S* spins, $\hbar$ is the reduced Plank constant, *r* is the distance between interacting spins), $J_n(\omega)$ are spectral density functions, ω_I, ω_S, are angular resonance frequencies of *I* and *S* spins, ω_e, ω_R are angular frequencies of the effective spin-lock pulse and of MAS rotation, respectively.

In the case of the CSA relaxation mechanism, the equation defining the relaxation time can be written as:

$$
\begin{aligned}
R_{1\rho}^{CSA} &= R_1^{CSA} + \sin^2\beta_\rho\left(R_{1\Delta}^{CSA} - \frac{1}{2}R_1^{CSA}\right)\\
R_1^{CSA} &= \frac{3}{4}\left(\delta\omega_I\right)^2 J_1\left(\eta,\omega_I\right)\\
R_{1\Delta}^{CSA} &= \frac{1}{6}\left(\delta\omega_I\right)^2\sum_{n=-2,n\neq 0}^{n=2}\frac{1}{|n|}J_0\left(\eta,\omega_e+n\omega_R\right)
\end{aligned}
\tag{2.40}
$$

where $\delta=\delta_{zz}-(1/3)\left(\delta_{xx}+\delta_{yy}+\delta_{zz}\right)$ is a reduced anisotropy and η is the shielding asymmetry ($\eta=\left(\delta_{xx}-\delta_{yy}\right)/\delta$). The same equation determines both R_1 and on-resonance $R_{1\rho}$ relaxation rates. If the angle between B_{1e} and B_0 is equal to 0° and 90°, then the equation converts to the standard R_1 and $R_{1\rho}$ definitions, respectively.

T_1 relaxation is most sensitive to motions whose frequency is close to the nucleus Larmor frequency. $T_{1\rho}$ relaxation is most effective in the case when the inverse motional correlation time coincides with the frequency of the applied spin-lock field pulse.

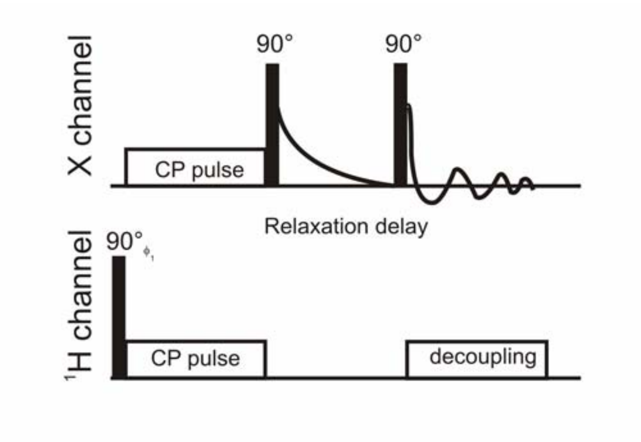

Fig. 8. The pulse sequence for T_1 relaxation time measurements.[97] ϕ_1 is a proton pulse phase.

One pulse sequence designed for R_1 measurements (Fig. 8) was developed by Torchia.[97] It begins with turning the proton magnetization into the *xy*-plane. Then, the contact pulse is applied simultaneously on the X and ^{1}H channels under the Hartmann-Hahn match condition, when polarization transfers to the rare nuclei. Then X magnetization is placed along the z -axis, thereafter polarization decay due to spin-lattice relaxation occurs during the variable relaxation delay. To register the signal, X magnetization is flipped back to the *xy*-plane. By varying the duration of the relaxation delay, we sample different points of the magnetization decay. The phase cycle of the proton pulse phase ϕ_1 (there is a shift in 180° during the first and second repetition of the pulse sequence) of the suggested pulse sequence helps avoid problems with unwanted X magnetization which does not arise from cross-polarization. Thus, the derived magnetization is free from the equilibrium magnetization term.

Another way to measure dynamics is by $T_{1\rho}$ relaxation. However, there is a problem that complicates these experiments. In addition to pure $T_{1\rho}$ relaxation, one also measures another contribution, namely the spin-spin contribution. It arises due to the coupling between the X nuclei and the proton dipolar reservoir, and does not contain any dynamic information. At weak to moderate amplitudes of the spin-lock field, the spin-spin contribution prevails.[98] In this case the experimentally measured $1/T_{1\rho}^*$ rate has a form of:

$$\frac{1}{T_{1\rho}^*} = \frac{1}{T_{1\rho}} + \frac{1}{T_{XH}} \tag{2.41}$$

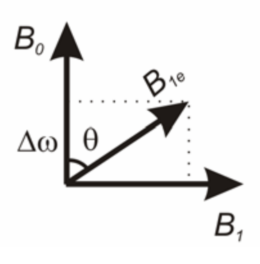

Fig. 9. Illustration of the effective spin-lock field.

The most straightforward way to reduce the efficiency of the spin-spin contribution is to increase the spin-lock field. However, this requires long and strong pulses which could heat the sample and damage the NMR probe-head. There were attempts to take into account this contribution by measuring the B_1 field dependence of $T_{1\rho}$[99] or by its suppression through homonuclear decoupling.[100] These methods are not always easy to implement.

Another suggested possibility is to increase the effective field felt by the nuclei through the resonance off-set of the spin-lock pulse frequency. Also heteronuclear decoupling breaks the interaction between the X nuclei and the ^{1}H dipolar reservoir.[93] The first method helps to achieve greater effective fields without a dangerous increase of the transmitter power (Fig 9):

$$B_{1e} = \sqrt{B_1^2 + \Delta\omega / \gamma_X} \tag{2.42}$$

The pulse sequences for these measurements are depicted in Fig. 10. This is a modification of the abovementioned Torchia sequence. The additional part is the embedded spin-lock pulse, which has a frequency offset flanked by two adiabatic increment pulses instead of a relaxation delay. These two flanked pulses are needed to place the magnetization along the effective spin-lock field B_{1e} and then back to the z-axis.

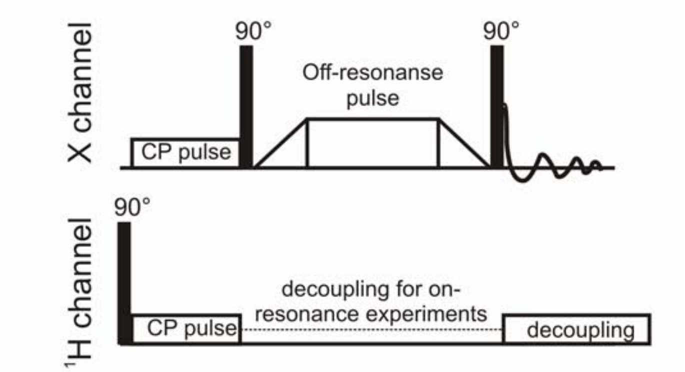

Fig. 10. Pulse sequence for the rotating frame relaxation rate measurements with a spin-lock pulse frequency off-set.[93] In the case of the on-resonance mode, ^{1}H decoupling during ^{13}C spin-lock field pulse is usually used, and just a spin-lock pulse on X channel is applied immediately after cross-polarization magnetization transfer (both 90° pulses on X channel as well as flanked pulses are omitted).

In the case that there is heteronuclear decoupling during the spin-lock pulse, we increase the T_{XH} time (Eq. (2.41)) and, thus, decrease the efficiency of the spin-spin contribution. The important issue is to avoid the Hartmann-Hahn matching condition. Otherwise, another pathway arises for the relaxation which interferes with the pure $T_{1\rho}$ relaxation.

One more problem which can significantly complicate the analysis of $T_{1\rho}$ relaxation arises when $\omega_e \approx n\omega_R$ ($n = 1, 2$). Matching of this condition is said to be a rotary resonance. In the case of rotary resonance, the reintroduction of the MAS averaged dipolar coupling between I and S spins occurs.[63,101] Analogously, the chemical shift anisotropies can be recoupled at the rotary resonance condition.[102] The effect of the rotary resonance is reflected in the form of the relaxation decay and brings a complex behaviour.

2.7. Correlation function and the "model-free" approach

The relaxation rates can be described as some combination of the spectral density functions (Eqs.(2.36) and (2.38)), which are Fourier-transforms of the correlation functions of motion (Eq. (2.37)):

$$C_n(\tau) = \left\langle D_{o,n}^{(2)}\left(\Omega_{PR}(t)\right) D_{0,-n}^{(2)}\left(\Omega_{PR}(t+\tau)\right)\right\rangle \qquad (2.43)$$

where:

$$\begin{aligned} D_{0,0}^{(2)} &= \frac{1}{2}\left(3\cos^2\theta - 1\right) \\ D_{0,\pm1}^{(2)} &= \sqrt{\frac{3}{2}}\sin\theta\cos\theta e^{\pm i\varphi} \\ D_{0,\pm2}^{(2)} &= \frac{\sqrt{6}}{4}\sin^2\theta e^{\pm 2i\varphi} \end{aligned} \qquad (2.44)$$

The correlation function of an anisotropic motion contains the most abundant information about all motions in which the probe nucleus takes part in. Thus, the determination of this correlation function is a main goal of dynamical studies through relaxation rates measurements. According to equation (2.43), the correlation function measures the fraction of the nuclei that do not change their orientation and position during the observation time τ. If most of the nuclei change their position then the $C_n(t)$ has a small value as a result of the distribution of $D_{0,-n}^{(2)}(t+\tau)$ values. If no motion occurs during τ then the correlation function has large value. The correlation function decays with an increase in τ. The longer the time interval the more molecules in the sample can change their position. In the simplest case of isotropic motion of a spherical particle, the correlation function has the exponential form:

$$C(t) = \exp\left(-t/\tau_C\right) \qquad (2.45)$$

where τ_C is the correlation time of the motion. In reality, especially in complex systems, the correlation function of the motion is much more complicated. A single relaxation time cannot provide enough information for the restoration of the correlation function. It is necessary to measure detailed temperature and frequency dependences of the relaxation parameters. Then, one uses a certain model to describe the experimental parameters to get amplitudes (angles) and correlation times of the motions. There are different models of motions and the choice of one is equivocal. Moreover, different models often give different results that describe experimental data equally well. Without any additional knowledge, there is no reason to prefer one over the other. A specific treatment is to use a well-known "model-free" approach[103,104]. According to this approach the correlation function of motion is divided into time-dependent and non-averaged parts:

$$C(t) = S^2 + \left(1 - S^2\right)\exp\left(-t/\tau_C\right) \tag{2.46}$$

here, S^2 is an order parameter defining the non-averaged part of the correlation function. The order parameter serves as a measure of the amplitude of motion and the relative populations of the states involved in dynamics. It ranges between 0 which means absolutely isotropic motion and 1 corresponding to the absence of the motion.

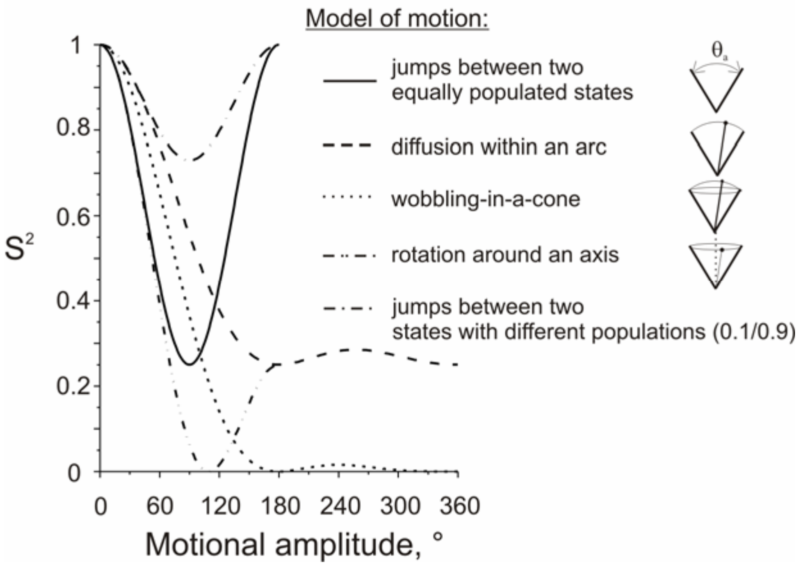

Fig. 11. Order parameter as a function of the amplitude of motion for different dynamic models.[96]

The term "model-free" comes from the fact that in this approach the averaging of the anisotropy of interaction can be represented by different models. If the model of motion is known, then we can unambiguously define S^2, but the inverse task is impossible to fulfil. The examples of S^2 dependencies on motional amplitude (angle) are shown in Fig. 11.

The order parameter for relaxation measurements can be represented as:[105]

$$S^2 = \int_0^{\pi}\int_0^{2\pi}\int_0^{\pi}\int_0^{2\pi} \rho(\theta_1,\varphi_1)\rho(\theta_2,\varphi_2)\frac{3\left(\vec{n}(\theta_1,\varphi_1)\cdot\vec{n}(\theta_2,\varphi_2)\right)^2-1}{2}d\varphi_1 d\theta_1 d\varphi_2 d\theta_2 \qquad (2.47)$$

here, $\rho(\theta,\varphi)$ is an orientation distribution function of the internuclear vector or symmetry axis of the CSA, $\vec{n}(\theta,\varphi)$ is a unit vector, the orientation of which is determined by the angles θ and φ. Some distribution functions for the most popular models are listed in the Table 1.[105]

Table 1. Orientation distribution functions for different motional models.[105]

Motional models	***Orientation distribution function***
"Two-site jumps"	$\rho(\theta,\varphi)=\delta(\varphi)\left(p_1\delta(\theta)+p_2\delta(\theta-\theta_a)\right)$
Diffusion within the arc	$\rho(\theta,\varphi)=\frac{\delta(\varphi)}{\theta_a},\quad \mathit{if}\ 0<\theta<\theta_a$ $\rho(\theta,\varphi)=0,\quad \mathit{if}\ \theta_a<\theta<\pi$
"Wobbling-in-a-cone"	$\rho(\theta,\varphi)=\frac{\sin(\theta)}{2\pi(1-\cos\theta_a)},\quad \mathit{if}\ 0<\theta<\theta_a$ $\rho(\theta,\varphi)=0,\quad \mathit{if}\ \theta_a<\theta<\pi$

In these functions θ_a defines the angular amplitude and $p_{1,2}$ are the populations of different sites ($p_1+p_2=1$ for "two-site jumps").

It should be noted that values of order parameters close to 1 do not necessarily imply small amplitudes of motion. It could also indicate large difference between populations of exchanging sites.[10] This is illustrated by the simulation, according Eq. (2.47), of the order parameter (i.e. apparent motional amplitude) for "two-site jumps" with varying populations, as plotted in Fig. 12.

Taking the Fourier-transform of the correlation function (2.46) we obtain the spectral density function:

$$J(\omega)=\left(1-S^2\right)\frac{\tau_C}{1+\left(\omega\tau_C\right)^2} \qquad (2.48)$$

Usually, dynamics in complex protein molecules include not only a single motional regime, it can be characterised by several distinct motional modes with different correlation times. If the nucleus simultaneously undergoes several independent motional processes, then the correlation function is expressed by:

$$C(t)=\prod_{i=1}^{N_m}\left[S_i^2+(1-S_i^2)\cdot\exp(-t/\tau_i)\right] \tag{2.49}$$

Here, N_m is the number of motional processes, S_i^2 and τ_i are the order parameter and the correlation time of the *i*-th process.

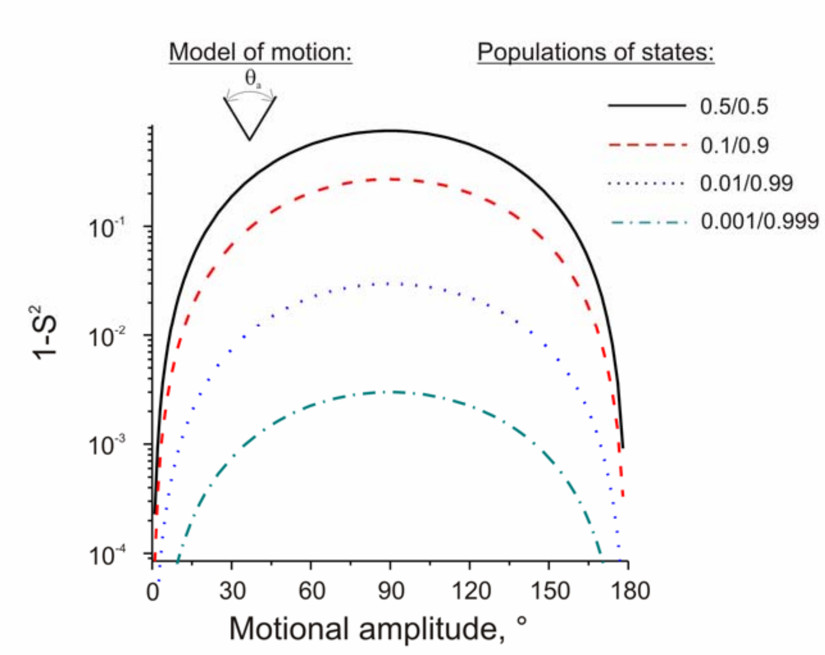

Fig. 12. Dependence of 1-S^2 on the angle for a “two-site” jump model when relative site populations are different.

The exponential form of the correlation function is not always adequate in describing molecular motions. There could be two main origins of the non-exponentiality – a homogeneous distribution of the correlation time and non-homogeneous distribution. The former is due to intrinsic non-exponentiality of the correlation function for special types of motion (for example, “wobbling-in-a-cone” gives non-exponential correlation function especially at large values of the angular amplitude). The latter is related to the possible difference in correlation times for the nuclei placed in different surroundings within the sample. To account for both origins of the complexity of the correlation function, a distribution of the correlation times should be considered. One possible distribution is the phenomenological Fuoss-Kirkwood distribution function:[106]

$$\rho\left(\frac{\tau}{\tau_C}\right)=\frac{\beta}{\pi\tau}\frac{\cos\left(\frac{\pi\beta}{2}\right)\cosh\left(\beta\ln\frac{\tau}{\tau_C}\right)}{\sin^2\frac{\pi\beta}{2}+\sinh^2\left(\beta\ln\frac{\tau}{\tau_C}\right)} \tag{2.50}$$

here β is a distribution width parameter; its value can be in the range between 0 (infinitely broad distribution) and 1 (no distribution of correlation times). The effect of different β values on the distribution of correlation times is depicted in Fig. 13.

The spectral density function assuming a Fouss-Kirkwood distribution has a particular simple form and can be written as:

$$J(\omega) = \frac{\beta}{\omega} \cdot \frac{(\omega\tau)^{\beta}}{1+(\omega\tau)^{2\beta}} \tag{2.51}$$

This distribution describes the NMR data quite well. For example, its correspondence to the "wobbling-in-a-cone" model is rather good (see Appendix).

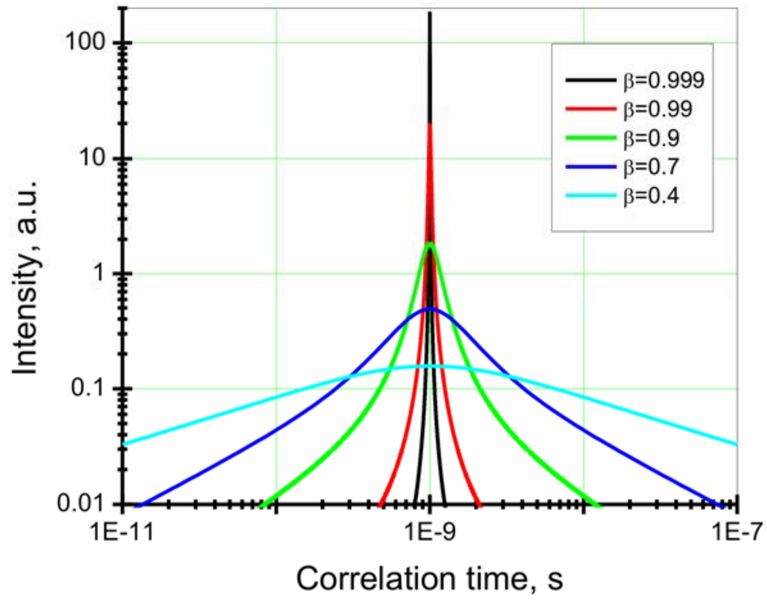

Fig. 13. Fuoss-Kirkwood distribution functions at different values of the distribution width parameters β.[107]

2.8. Protein dynamics as probed by NMR experiments

The conformational dynamics of proteins is a popular subject of NMR investigations. The first dynamic studies were carried by liquid-state NMR spectroscopy. A broad spectrum of correlation times for dynamics was suggested on the basis of a variety of liquid-state experiments.[2,4,5,7,8,108–111] Despite the poor resolution of ss-spectra, the studies of dynamics in amorphous and crystalline states also deserve attention. The main virtue of solid-state spectroscopy for protein dynamics is the absence of overall tumbling. This can be exploited to explore the slower dynamics which are more biologically significant.

2.8.1. *Dynamic studies by wide-line NMR spectroscopy*

The first ssNMR experiments on proteins were performed in 1960-70's. One such work was the investigation of the ribonuclease and bovine serum albumin by means of proton wide-line NMR spectroscopy.[112] The experimental conditions investigated were varying temperature from -140°C to 180°C and also different hydration levels starting from 0 to 0.2. The linewidth of the spectrum and its second moment served as a measure of dynamics in this work. Because this study relied on the wide-line regime, all motional information was averaged for all protons in the sample. Nonetheless, important conclusions were made by the authors. First, proteins are not static and rigid systems. That is, motions of the backbone and side-chains occur even at the lowest temperatures (-140°C) and even in dry proteins. Secondly, they detected different types of motions. The onset of the second type of motion reflected in abrupt line narrowing was observed at 20°C for bovine serum albumin and at higher temperature for the ribonuclease. Blears and Danyluk concluded that dried proteins are motionally stabilized by the network of contacts restricting biomolecules mobility, and that a water matrix which appears upon hydration facilitates motional changes in the proteins.

2.8.2. *Proton and deuterium experiments*

The existence of mobility in proteins for a variety of environmental conditions was also confirmed by other groups. Andrew and co-workers published a series of works devoted to the investigation of molecular dynamics in solid polypeptides and proteins by means of proton NMR relaxometry at different temperatures.[113–118] From T_1 relaxation time measurements at different field strengths, it became clear that the main source of proton relaxation is the rotation of CH_3 groups. This type of motion can be detected at very low temperatures (90 K), and it provides the most efficient relaxation mechanism. The activation energy of this type of motion was found to be quite similar for different proteins, and its value is around 10 kJ/mol. The correlation time of the CH_3 rotation was found to be on the order of $5 \cdot 10^{-13}$ s. Measured relaxation times and second moments of the signals also showed the existence of additional slow motions. These could be side-chain reorientations or segmental motions restricted by hydrogen bond network.

Proton NMR is, of course, a simple and fast method to extract dynamic information. However, the lack of resolution prevents more specific investigations. Deuterium is another possible nucleus to carry out dynamic measurements. The main contribution to the deuterium lineshape is the quadrupolar interaction. All motions faster than several microseconds affect the lineshape. This was successfully employed by a number of works.[10,119] Mack *et al*[119] explored the temperature dependence of the motions in a fully hydrated microcrystalline lysozyme. Lineshape analysis and relaxation time measurements lead to the conclusion that a single type of motion cannot adequately describe the dynamics of amide sites in the protein. They performed "model-free" fitting of the relaxation times measured at different temperatures suggesting two independent motional regimes with distinct correlation times. The defined parameters for the fast motion were the order parameter (S^2) ~0.9 and a correlation time τ_C~15 ps. Those for the slow motions were S^2 ~0.98 and τ_C ~10^{-7}-10^{-6} s.

Williams and McDermott[10] employed deuterium NMR spectroscopy to investigate the loop motions in triseophosphate isomerase. The experimental methods, including T_1 anisotropy, lineshape analysis and inversion-recovery experiments, supplied information on a very broad dynamical range spanning from 10^{-10} s up to several seconds. Special labelling techniques allowed them to monitor motions restricted to the loop. Again two types of motions were detected: nanosecond local reorientations of side chains and an "opening-closing" event in the loop. The rate of the loop motion was found to be close to the inverse of the enzyme turnover time 10^4 Hz.

2.8.3. *Dynamics via low-spectral resolution ssNMR*

By combining dynamic information obtained from different nuclei it is possible to gain better insight into internal protein motions. Such a combined analysis superposes the advantages of measuring different nuclei (e.g. the simplicity of experiments performed on protons with the "group" resolution obtained in the amorphous samples through ^{13}C NMR measurements). Yoshioka *et al*[120] employed such a strategy to investigate bovine serum γ-globuline by T_1 and $T_{1\rho}$ measurements at different hydration levels. The results of their study on hydrated samples proved the existence of at least three types of molecular motions with different correlation times. Their activation energies were found to be 33.5, 10.47 and 4.2 kJ/mol and their correlation times were $2\cdot10^{-10}$, $5\cdot10^{-9}$ and $9\cdot10^{-13}$ s, respectively. They attributed the motion with $\tau_C = 5\cdot10^{-9}$ s to methylene groups and $\tau_C = 2\cdot10^{-10}$ s to methine groups. Similar work was performed by Fedotov *et al*[121] on lysozyme at different temperatures and at two humidity levels. Multiple ^{1}H and ^{13}C relaxation times were measured in the laboratory and rotating frame and analyzed by a "model-free" approach. The temperature dependence of the relaxation rate profile in hydrated lysozyme showed several minima. This demonstrated the existence of a number of motional processes in the protein. The fastest motion, which was attributed to the CH_3 group rotation around its symmetry axis, occurred on the picosecond timescale with an activation energy $E_a = 12$ kJ/mol. Nanosecond motions, involving all groups of the backbone and side chains, were characterized by broad distribution of correlation times. Assuming the "wobbling-in-a-cone" model, the amplitude of the motion was found to be around 10°-15°. Finally, the slowest motion was seen only in wet samples and had a correlation time in the range of microseconds. In addition, the authors tested the behaviour of the motional parameters versus dehydration. They found that CH_3 rotation did not depend on the humidity level. However, other motions demonstrated a hydration response. The largest effect upon water increase was observed for the slowest motions. Later Krushelnitsky and Reichert[122] expanded the obtainable information on hydration induced dynamic changes by measuring $T_{1\rho}$ relaxation times. These measurements allowed them to better characterise slow dynamics up to hundred microseconds. An important result were nearly invariant correlation times of CH and CH_2 groups upon hydration. In contrast, motional amplitudes showed a significant increase upon hydration. In addition, they characterised the nature of the observed motions and described their peculiarities for side chains and the backbone separately. Detailed humidity dependencies were not measured within this work; therefore, more specified conclusions about hydration response of protein dynamics were not possible.

Huster *et al*[123] employed a variety of ssNMR experiments to detect mobility in colicin Ia channel-forming domain on different timescales (ps-s). Their aim was to investigate the differences of the domain dynamic behaviour in soluble and membrane-bound states. Motionally averaged ^{13}C-^{1}H dipolar couplings were measured for the backbone residues and side chains. These measurements showed variations of the amplitudes for different structural units and for soluble vs. membrane-bound states. The mobility of side chains was increased compared to those of the backbone. Similarly, membrane-bound proteins possessed more pronounced dynamics. The same results were obtained by ^{15}N CSA measurements. The reduction of the linewidth due to molecular motions in the soluble state is slightly larger than in a membrane complex. To describe dynamics on the microsecond scale they performed proton $T_{1\rho}$ measurements. They found the correlation time of such motions to be around 0.8 – 1.2 μs depending on the membrane binding. As it follows from previous studies[122,123] by including $T_{1\rho}$ experiments, it is possible to explore a wider range of motions. However, microsecond motions are not the limit of accessibility for ssNMR. Better insight into slow protein dynamics can be achieved by exchange spectroscopy. There are examples of such investigations in proteins by ssNMR. The first work was published by Krushelnitsky *et al,*[124] where they investigated polypeptide (polyglycine) and protein barstar. Using time-reversed ODESSA they observed slow motions on the millisecond timescale with rather large angular amplitudes (~18°) and high activation energies (40-120 kJ/mol). These dynamics are found only in the wet barstar suggesting the relevance of motions for biological protein function. They further revealed the existence of a correlation time distribution. Because the information obtained here was averaged for all protein molecules, a distribution appears because of different correlation times inherent to different protein domains.

Huster *et al*[123] performed another exchange experiment, CSA CODEX, on colicin Ia channel-forming domain, and revealed that no motions occur in the time window of the exchange method. They concluded that this particular protein exhibits no millisecond motions.

Experiments performed with "group" resolution are undoubtedly more informative than those obtained by unresolved wide-line techniques. It is preferable to monitor each distinct residue in the protein, obtaining dynamic information exactly for the part of interest.

2.8.4. *Site-specific studies of protein dynamics in the solid-state*

Concerning early site-resolved studies, I would like to pay special attention to the work carried out by Cole and Torchia[30]. They performed ^{15}N relaxation rate measurements in crystalline staphylococcal nuclease. Due to the broad distribution of chemical shifts in the ^{15}N NMR spectrum and the similar environment for all the crystallites, they explored dynamics with chemical resolution. They resolved signals of different valine residues in the backbone and measured the relaxation rates for each of them separately. The most important observation of this work was that ssNMR is much more informative than the solution state in investigating motions on the nanosecond timescale and slower. They also revealed the similarity of the protein structure in liquid and fully-hydrated states. In the case of solution NMR backbone relaxation rates are rather uniform for different parts of the protein. However, the authors detected large variations in ^{15}N relaxation rates throughout the protein backbone. This proved that dynamic inhomogeneity exists in the protein backbone. Relaxation rates measured at 5.9 and 11.8 T were fitted according to the "model-free" approach. The fitting indicated that the correlation times of the motions are in the range of 0.2-4 ns. However, by investigating motionally averaged ^{15}N CSA powder patterns, the existence of more than one motion with a distinct correlation time was also found.

Site-specific resolution opens a new era in the investigations of protein dynamics. The measurements of NMR parameters with site-specific resolution reveal that the dynamics for specific sites occurs on different timescales.[53,55,58,125–134] The main parameters measured in all these papers are relaxation rates (T_1, $T_{1\rho}$, cross-correlated relaxation), motionally averaged dipolar couplings, and sometimes chemical exchange rates. Some of the authors performed simultaneous analysis of a range of experimental data to extract amplitudes and correlation times for the individual proteins. Different proteins, of course, have different dynamics. However, on the basis of the experimental literature, we can conclude that there are characteristic features that are similar for different microcrystalline proteins.

^{15}N and ^{13}C relaxation rates measured by different groups[53,55,125,127,128,131–134] showed the same tendencies. In general, residues located in the loops, turns and C and N termini of the protein showed increased spin-lattice relaxation rates, while residues involved in secondary structures (β-sheets and α-helices) posses smaller relaxation rates. In addition, within the secondary structures the relaxation rates also vary. The relaxation is usually more pronounced at the ends of the β-sheets and α-helices and is less efficient in the centre of these "rigid" structure elements. Thus, generally, the R_1 dispersion profile tracks secondary structure. The increased relaxation rates for adjacent structural units indicate that there is correlated motion involving different parts of protein simultaneously. Not only backbone residues show the variation in relaxation rates along the molecule, side chains at different positions also undergo relaxation processes with different rates. One more peculiarity in the slow/fast R_1 alterating pattern was detected by Schanda *et al.*[132] The residues bonded to side-chains pointing towards the hydrophobic protein core possess smaller relaxation rates. Consequently, their motions are restricted compared to the residues bonded to the external side-chains.

The variations in mobility along protein molecules were studied by measurements of motionally averaged dipolar couplings.[53,58,126,129,132] Similar dynamical features were found. Despite the difference in the stiffness of various proteins, general observations were made. Dipolar couplings are more averaged by motions in the loops and termini of the proteins than within the secondary structural units. For the residues involved in secondary structures the measured dipolar couplings were close to the rigid limit value.

Site to site variations in protein mobility on different timescales were also confirmed by the measurement of other ssNMR parameters, for example, dependencies of signal intensities and motional averaged CSA on temperature,[53] and measurements of the asymmetric dipolar couplings.[58]

2.8.5. *Global fit of site-specific relaxation data*

In the last few years several papers reporting on global fits of different NMR parameters which are sensitive to the molecular motions were published.[128–133] Such works relate NMR observables to physical quantities (amplitudes/angles, activation energies and correlation times) describing internal protein dynamics. The first work I would like to discuss was done by Reif and co-workers.[129] They quantify the molecular dynamics of the microcrystalline chicken α-spectrin SH3 domain. The experimental data included for the global analysis in the frame of a "extended model-free approach"[103,104,135] were ^{15}N T_1 relaxation times at two different field strengths, ^{15}N CSA and ^{1}H-^{15}N dipole cross-correlated relaxation rates, and ^{1}H-^{15}N motionally averaged dipolar couplings. The "extended model-free" approach assumes the existence of two components for the correlation function. They found the correlation times for the fast component to be in the picosecond time range, and the slow component to be in the nanosecond region. However, they found that there are six residues which show unusually large values of correlation times (the slow one close to microseconds). The possible explanation of such behaviour comes from restrictions which prevent faster fluctuations. This assumption was confirmed by the values of the order parameters obtained for these six residues. Another work[130] published by the same authors was devoted to the simultaneous analysis of solution- and solid-state data (^{15}N T_1 at 500, 600 and 900 MHz in solid and solution states, R_2 and NOE data) measured in SH3 domain. Assuming the similarity of solution and solid-state dynamics, they again detected two types of mobility in the nanosecond and picosecond ranges, where the nanosecond dynamics was found to have smaller amplitudes. A resulting residue-to-residue comparison of motional parameters obtained by the two approaches demonstrated that the inclusion of additional NMR parameters sometimes significantly changes the values of amplitudes and correlation times.

The next work employing global fit analysis of solid-state NMR parameters (including ^{1}H-^{15}N dipolar couplings, up to five ^{15}N relaxation rates measured at different field strengths) measured in ubiquitin was carried out by Schanda *et al.*[132] The "extended model-free" approach applied to the experimental data suggested the existence of two types of motions in ubiquitin. The fast motion was characterised by picosecond correlation times and rather uniform distribution of order parameters, while for the slow (nanosecond) motions, the order parameter followed the secondary structure of the protein. Loops between regular secondary structural elements possessed more prominent dynamics both on nanosecond and picosecond timescales. In the same way as in the abovementioned paper,[129] the slowest motions detected here were in the sub-microsecond time window.

The "model-free" approach is not the only one which was employed as a combined analysis of experimentally measured relaxation rates. Giraud *et al*[128] performed the fitting of the spin-lattice relaxation rates measured at two different fields (11.74 T, 16.45 T) according to the "diffusion-in-a-cone" model with a single motional regime. They estimated diffusion times for 15 residues to be in the range $5\cdot10^{-8}$–$5\cdot10^{-7}$ s (corresponding to correlation times on the nanosecond timescale) and a cone opening angle ranging from 5° to 20°.

To extend the time range described by the combined analysis one could include the $T_{1\rho}$ relaxation rate, which is sensitive to microsecond dynamics. This was done by Lewandowski *et* *al* for the protein GB1.[131] They treated their experimental data (R_1 and $R_{1\rho}$ measured at a single magnetic field) in the framework of two models: "wobbling-in-a-cone" and "Gaussian axial fluctuations" with just a one motional regime for each residue. Both models gave the same result for the correlation time of motion (10-20 ns) and for the order parameters. The alteration of the order parameters tracked the secondary structure. Again, in general, amplitudes of motions were found to be larger at the edges of sheets and helices compared to the middle of secondary structural units. The experimental data set was later expanded by the addition of dipolar couplings and the comparison with MD simulations.[133] Some discrepancies of the motional parameters found from the combined analysis and determined by MD simulations were observed. One of the possible explanations is a low number of experimental data points used in the fitting procedure (four R_1 at two different field strengths, $R_{1\rho}$ and ^{1}H-^{15}N dipolar couplings).

2.8.6. *Probing of millisecond to second motions by exchange NMR spectroscopy*

Not only relaxation has been measured with high resolution in proteins. To probe slow motions on the millisecond-second timescales, exchange experiments were also employed. DeAzevedo *et al*[136] applied ^{13}C-detected ^{15}N-CODEX experiments to study slow-motions in a ^{13}C and ^{15}N labelled protein (ubiquitin) and a genetically engineered multidomain protein hydrogel that contains two leucin-zipper domains (ASA). In ubiquitin there was no significant intensity decay which would indicate to the existence of slow motions. Thus, ubiquitin hardly possesses large-amplitude millisecond motions. In contrast, the presence of a significant amount of slow mobility was detected in the zipper domain. All residues in the domain reveal intensity decay due to exchange, indicating that the entire domain moves as a whole. The correlation time of the motion was determined to about 80±8 ms. Later this group of authors published more detailed information about motions in ASA[137] by measuring the exchange decays for various sites. Moreover, the temperature dependence was examined to gain more insight into the nature of the domain dynamics. They found that slow motions are thermally activated as their correlation times are temperature dependent. The measured correlation times were uniform for different residues (~80 ms); thus, the conclusion that the domain moves as a rigid body was confirmed. The amplitude of motion was determined to be around 50°.

The abovementioned examples[136,137] using solid-state exchange NMR in proteins registered changes in the CSA tensor. It is also possible to monitor the reorientation of the dipolar coupling vector. Krushelnitsky *et al*[138] applied solid-state dipolar CODEX NMR to capture millisecond to second motions in the SH3 domain of chicken α-spectrin. Slow motions in this work were observed for approximately half of the residues. Most of these residues were in the terminal parts of the domain or in the region between S36 and R49. Between these residues there is a loop with adjacent secondary structural elements (β-sheets). The analysis of the correlation times ($\tau_C \sim 1-3$ s) of all the residues undergoing slow motion suggested that there is one dominant motional regime.

2.8.7. *Concluding remarks*

Thus, as was reported in the literature, there are different motions inherent to proteins:

-fast rotation of the end groups (CH_3 and NH_3) and backbone vibrations with picosecond correlation times;

-nanosecond motions with small amplitudes, which vary for different sites along the backbone and side chains;

-slow microsecond to millisecond motions specific for protein unique function;

-and ultra-slow motions on millisecond to second timescales, requiring large scale rearrangements of the protein structure. These motions do not necessarily occur.

The mobility differs from site to site following the secondary structural elements. Loops, turns and N and C termini are, in general, more mobile than helices and sheets. The motions in the centre of "regular" structures are the most restricted, while at the edges one expects fewer spatial constraints. Sometimes slow motions involve not only one structural unit but also adjacent loops and other units. Thus, large parts of proteins can take part in correlated motion. Such motions are believed to be at the heart of biological relevance.

Besides the fact that protein dynamics is a popular subject of many investigations, there is still a lack of information characterising slow microsecond timescales. The main methods employed to investigate such types of mobility were the measurements of motionally averaged dipolar couplings and CSA interaction. However, these quantities sample the averaged information over the time region up to μs. The extraction of exactly microsecond mobility parameters is quite a challenging task. Measurements of $T_{1\rho}$ relaxation rates are especially sensitive to this time window. The current work implements $T_{1\rho}$ relaxation rate measurements into the experimental methodology, covering the gap where information is needed.

3. The comparison of the hydration response of internal protein dynamics on different time scales

As was already mentioned in the introduction, one of the most important questions arising in the investigation of globular proteins in the solid-state is the influence of intermolecular forces. It is reasonable to ask whether or not information derived from solid-state experiments is valid in exploring biological properties of proteins, which are natively in the dissolved state. The structure of proteins in fully-hydrated and solution states is quite similar[46,47,139–141] except for flexibly disordered surface regions involved in crystal contacts. However, even these contacts are felt by only a few adjacent residues and do not propagate into the hydrophobic inner part of the globule.[55] There is also evidence that protein functionality in the hydrated state (around a humidity level h=0.2-0.3) corresponds to that in solution.[42,43,46,141,142] Thus, it seems that internal protein mobility is the same in these two states. Up to the present moment, a number of studies have been dedicated to the investigation of hydration response of protein motions.[32,33,41–43,46,61,143–146] It is believed that at the hydration level of h~0.4 (g water per g protein) the dynamics of proteins strongly resemble or are even the same as in solution. A further increase of the water content above this level effects motions only slightly. However, most of the work devoted to hydration response was concentrated on high frequency movements (correlation times on the range of ps-ns), and just a few monitored the slower but more important motions.[60,147]

The widely used techniques for the investigation of protein dynamics are neutron scattering and NMR. From neutron scattering we obtain information about proton displacements on the picosecond to nanosecond timescale. One of the most rigorous investigations was made by Roh et al.[41] They studied protein dynamics and found that in addition to fast methyl rotation two more motional processes occurred. Fast conformational fluctuations increase rapidly at low humidity (h<0.2), while at higher levels they only slightly depend on water content. Slow relaxation processes which are not activated at low humidity levels (h~0.2) increase sharply at 0.2<h<0.4. Methyl rotation was found to be insensitive to incremental water addition.

In this section we compare the hydration response of internal protein dynamics not only on the ps to ns timescale but on longer timescales as well. Application of ^{15}N and ^{13}C T_1 and $T_{1\rho}$ relaxation time measurements provides such information from backbone and side chains independently. These experimental parameters are sensitive to motions in different time windows; thus, we can capture motions corresponding to different motional regimes. In addition to relaxation time measurements, ^{15}N exchange experiments probing dynamics on millisecond to second timescales were used. As a result of the performed experiments, it is possible to describe the hydration dependence of different types of motions in a wide frequency range. The results presented in this chapter were obtained by our group and published.[148] My own contribution to this work was performing a part of the experiments, analysing all experimental data and drawing a part of the conclusions.

3.1. Samples and experimental conditions

Samples used in these experiments were ^{15}N enriched lysozyme from bacteriophage T4 and human αB-crystallin. The first protein breaks down the peptidoglycan to release phage particles from cell walls, and is a model protein for various scientific studies.[149] Alpha-crystallin possesses chaperone-like properties and prevents the denaturation of other mammalian lens proteins – it provides lens transparency. The disruption of this protein's functionality can result in a serious disease – cataracts.[150] Both of the studied proteins have approximately the same backbone length; however, possess different hydrophobicity. Lysozyme in water solution exists as a well-packed globule, whereas αB-crystallin forms large aggregates.

To prevent difficulties with low signal-to-noise ratio isotope enrichment was very important. For ^{15}N enrichment, ammonium chloride was used as the only ^{15}N-source. The proteins synthesizing protocols are described elsewhere.[149,150] Before the NMR experiments the protein samples were lyophilized from the phosphate buffer in a vacuum dessicator under pressure of 0.37 mbar, the water condenser temperature was -52°C. We assume that immediately after lyophilisation the water content was equal to zero. There is, in fact, still a few percent of internal water molecules which can only be removed by drying at elevated temperatures. However, that would result in protein denaturation. Lyophilised proteins were placed in NMR rotors, and then hydration was performed in a vacuum dissicator. For hydration, the protein in MAS rotors were kept under water vapour until the desired humidity level was achieved. The water content was defined by weighing the rotor before and after hydration. Hydration ($h = \frac{m_{water+sample} - m_{sample}}{m_{sample}}$) was varied between 0 and 0.65. Larger hydration levels are problematic for MAS NMR experiments. Beyond a certain water content the protein becomes pasty. Under fast magic angle spinning the sample forms a layer on the walls of the rotor, and the excess water accumulates in the middle. It is then hard to define a true humidity level of the protein.

All experiments were performed on Varian INOVA and Bruker Avance spectrometers with proton resonance frequencies of 400 MHz. The pulse sequence for T_1 measurements (fig. 8) was developed by Torchia.[97] The measurements of rotating frame relaxation times were conducted with a resonance offset for the spin-lock pulse frequency to avoid spin-spin contributions to the apparent relaxation rate (fig. 10).Varying the duration of the relaxation delay or spin-lock pulse duration, we sampled different points of the magnetization decay (12-15 time points). The maximum spin-lock pulse length reached 80 ms. To avoid overheating the protein, long recycling delays were used (5-6 s). The effective spin-lock frequencies and the angles between B_{1e} and B_0 were 108-112 kHz and 19.5-20.5º for aliphatic carbons, respectively. For ^{15}N, 63.5-66 kHz and 17-19º were used. It is very important to calibrate the spin-lock power and frequency off-set carefully to be sure that these parameters are the same for the measurements at different hydration levels.

The last experiments performed on hydration response was done by CODEX.[88,136] The pulse sequence is depicted in figure 7. We performed CODEX experiments on the nitrogen-15 isotope of T4 lysozyme. Experimental conditions were the following: MAS rate of 4 or 5 kHz for ^{13}C experiments and 6 kHz for ^{15}N experiments, cross-polarization times were adjusted for every experiment and found to be in the range 0.5-1.0 ms, the acquisition time of the FID was 10-20 ms, the proton decoupling frequency was 60-70 kHz, the frequency coding period before and after the mixing time was 1 ms. The temperature calibration was done with methanol.[151] During the experiments the temperatures was kept at 25°C (unless another value is stated) with accuracy close to 1°C. The recycle time was 1.5-2.5 s.

3.2. The results

3.2.1. *Hydration influence on protein spectra*

A direct polarization (DP) spectrum contains the most abundant information about a sample; however, the measurement of a DP spectrum is very time-consuming due to the low sensitivity of rare nuclei. The implementation of cross-polarization (CP) can save time; however, it is necessary to make sure that the dynamic information is not lost during the cross-polarization process. Thus, the first issue I would like to discuss in this section is the difference between the ^{13}C and ^{15}N CP and DP spectra of proteins at various hydration levels. As can be seen in fig. 14, there is a small difference of the relative peak intensities in the DP and CP spectra in our samples. This difference has two possible origins. First, cross-polarization efficiency can be different for different carbon/nitrogen groups. Second, T_1 relaxation times for some chemical groups can be long and reach up to several tens of seconds. To completely restore the equilibrium magnetization, it is necessary to use recycling delays much longer than T_1. Thus, it could be that the recycle delays (20-30 s) used during experiments were not long enough to accumulate the entire signal.

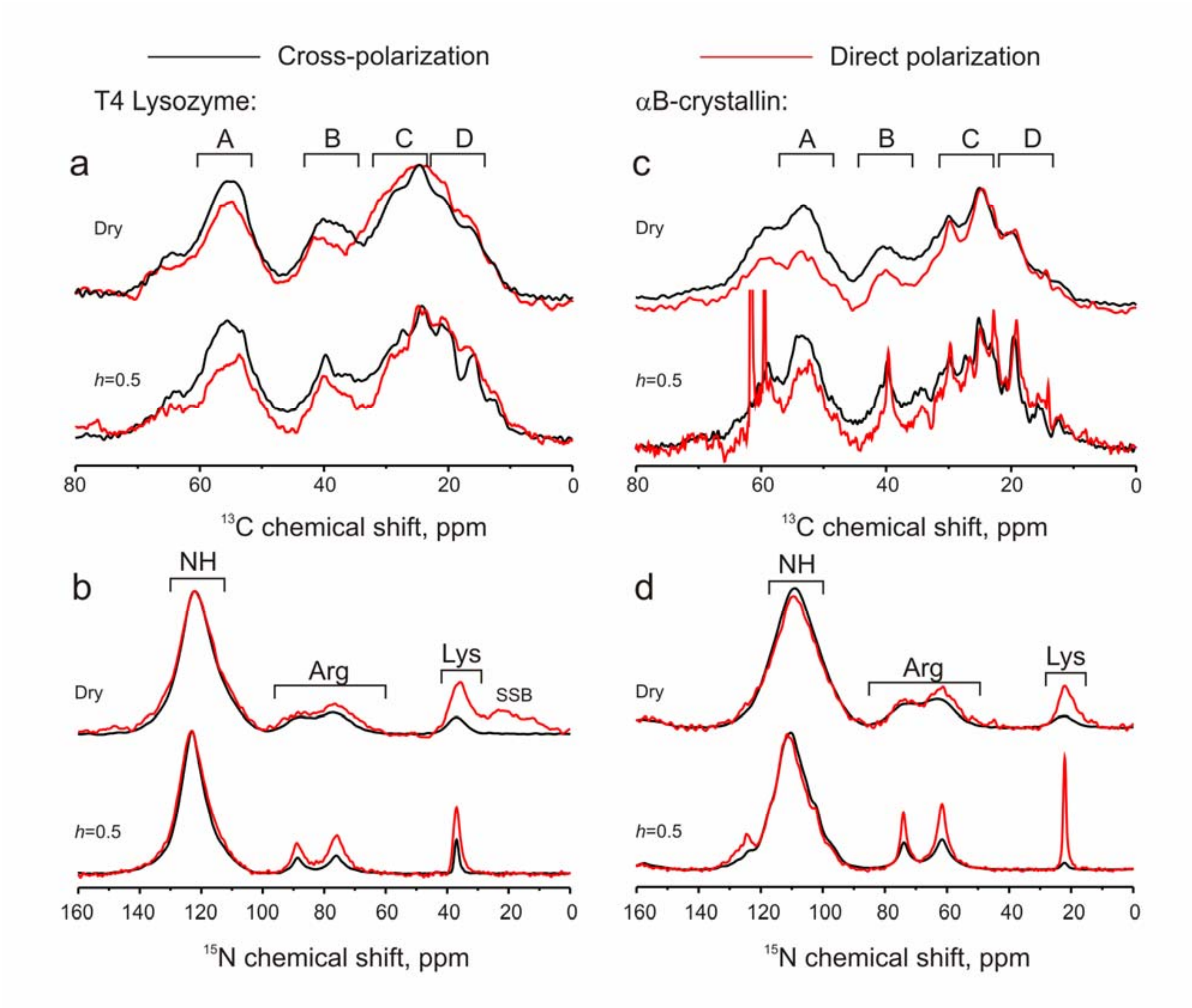

Fig. 14. ^{13}C (aliphatic) and ^{15}N spectra of T4 lysozyme (a, b plots) and αB-crystallin (c, d plots) with direct vs. cross-polarization at two different hydration levels (dry h=0 and h=0.5). (Replot of the data from Ref. [148]). SSB denotes spinning side bands due to the MAS.

The similarity of the CP and DP spectra for the both lyophilized proteins demonstrates an almost equal efficiency of cross-polarization for different atomic groups. This also means that the dipolar coupling strength stays stable under hydration. Kennedy and Bryant[152] and Gregory *et al*[153] concluded analogous results in their studies on hydration response by solid-state ^{13}C NMR. Thus, the difference in CP efficiency cannot be the reason for our discrepancies. This means that the incomplete recovery of magnetization causes these minor differences in our spectra.

It should be noted, that there is one prominent difference in the DP and CP spectra for hydrated αB-crystallin. Two sharp lines around 60 ppm (fig. 14c) are visible in the DP ^{13}C spectrum but are absent in the CP spectrum. This difference cannot be attributed to a problem in magnetization recovery, leaving cross-polarization as the main reason. The polarization transfer depends not only on the number of protons surrounding the probe nucleus, but also on mobility. The more motion that occurs, the less effective magnetization transfer is. These two sharp lines are assigned to the mobile fraction of C^{α} carbons, for which the efficiency of cross-polarization is poor. Thus, these signals are absent in the CP spectrum. This finding is not surprising and was already discovered by Perry et al.[154] αB-crystallin contains an unstructured C-terminus with increased mobility,[155] leading to the sharpening of DP signals and their disappearance from the CP spectrum. In order to exclude a possible origin of misinterpretation, I will not consider the spectral region beyond 57 ppm for all ^{13}C CP spectra of αB-crystallin. For the same reason, I will not consider the down-field range of ^{15}N spectra with chemical shifts >134 ppm.

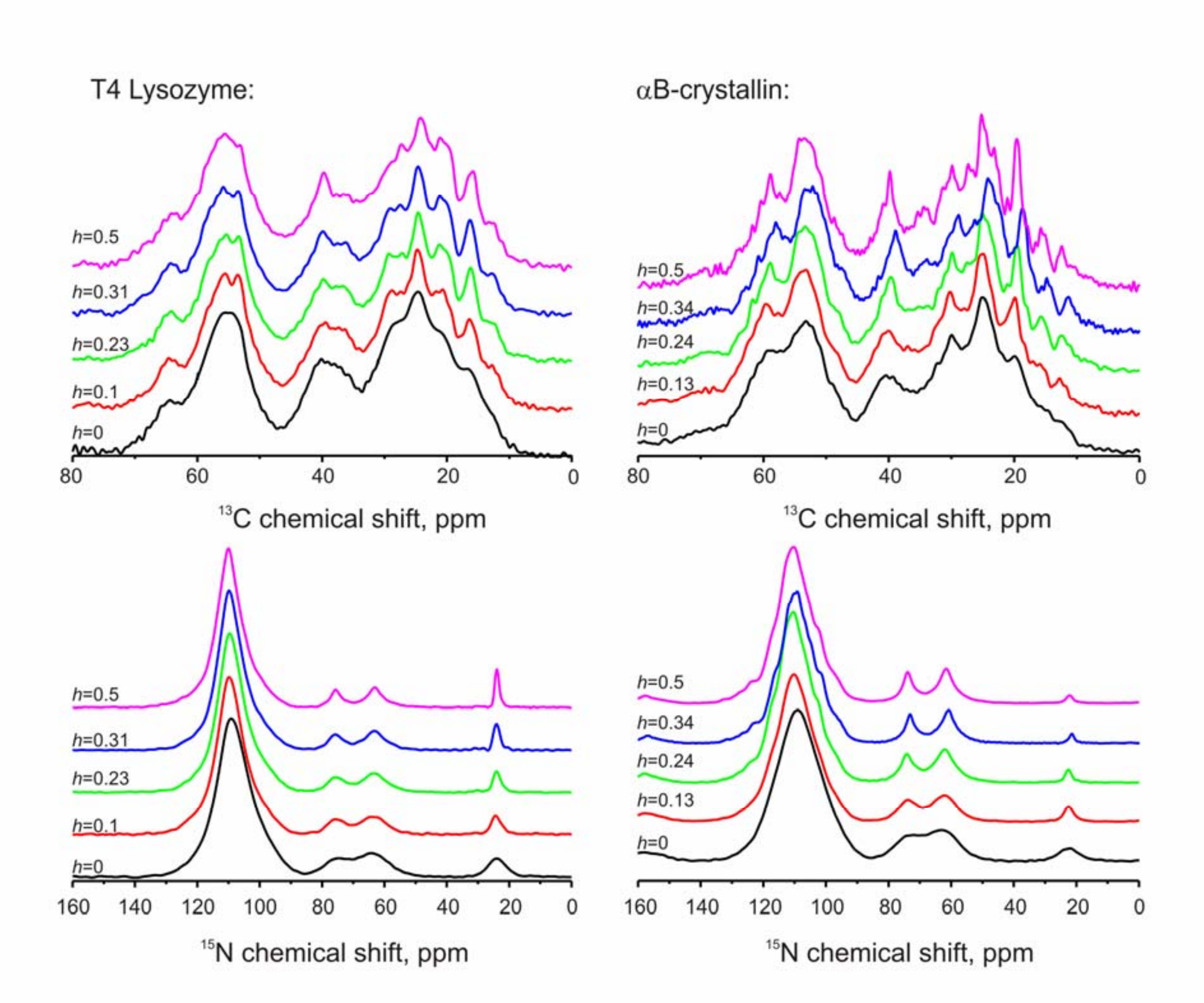

Fig. 15. ^{13}C and ^{15}N spectra of αB-crystallin and T4 lysozyme at different hydration levels. In carbon spectra only the aliphatic domain is represented. The ^{15}N spectra consist of the backbone peak and Arg and Lys peaks of the side-chains. (The data published in Ref. [148]).

In order to estimate the influence of hydration on the protein structure, the αB-crystallin and T4 lysozyme ^{13}C and ^{15}N spectra at different hydration levels were measured (Fig. 15). There is an improvement in apparent spectral resolution for both protein samples with increasing hydration levels. This effect was observed earlier, and is believed to be a result of the narrowing of the protein subconformation distribution.[39,152,153] During freeze-drying a protein becomes stabilized with greater electrostatic interactions, making the microenvironment of different protein molecules inequivalent. Each subconformation results in a sharp resonance line, the superposition of which leads to wide signals. Under progressive hydration, the system of hydrogen bonds breaks down. Ionized and polar groups of the protein gradually become hydrated and restricting contacts disappear reducing the number of subconformations. Thus, in hydrated samples we see sharper, better resolved signals of different protein groups.

The changes in resolution are not the same for backbone and side-chains residues. The side chain groups are more sensitive to the presence of water compared to the backbone. The more significant narrowing of side chain signals could originate from the fact that side chains are more involved in the formation of inter and intra molecular contacts. They are more accessible for water molecules which reduce the distribution of subconformations of the protein.[39]

Spectra at h=0, 0.06 (h=0.06 is not shown here) and 0.13 show almost equal resolution. The greatest changes in the linewidth occur at hydration levels between 0.2-0.3 g of water per g of protein. This hydration level corresponds to the saturation of polar groups of the protein.[42,46] Our results are in agreement with those obtained by Gregory et al.[153] In their work, they compared the solid-state ^{13}C NMR spectra measured at different hydration levels in hen egg white lysozyme. The onset of structural changes found by this group was around h=0.2; the changes mostly occurred before the saturation of the non-polar groups (h=0.38).

From the spectra, it is evident that site-specific resolution of signals is impossible. To get information on different structural units (backbone, different side chain groups) we divided the aliphatic region of ^{13}C spectra into four groups: group A corresponds to the methine C$^{\alpha}$ and mainly originates from the backbone, B contains methylene carbons, C and D reflect the methyl groups with some additional methylene signals in the C group. Groups B-D correspond to side chains of the proteins (Fig. 14). The analysis of the parameters characterizing the hydration response of groups instead of individual lines, helps us to avoid difficulties with different resolutions at different h levels.

There are fewer nitrogen atoms in the protein enabling us to differentiate between different side chain residues (peaks of arginine and lysine). The most intense signal in the ^{15}N spectra (115-120 ppm) corresponds to backbone nitrogens with a small portion of side-chain residues (Asn, Gln and Trp). The contribution from the side chain groups to the signal intensity is not very large and we can neglect it.

3.2.2. *Relaxation data analysis*

To measure the relaxation rates, the integral intensity of the lines from different groups as a function of the variable delay time were recorded. Some examples of relaxation decays are depicted in fig. 16. The intensity at the first time point was normalized to 100 for αB-crystallin and to 50 for T4 lysozyme for clarity.

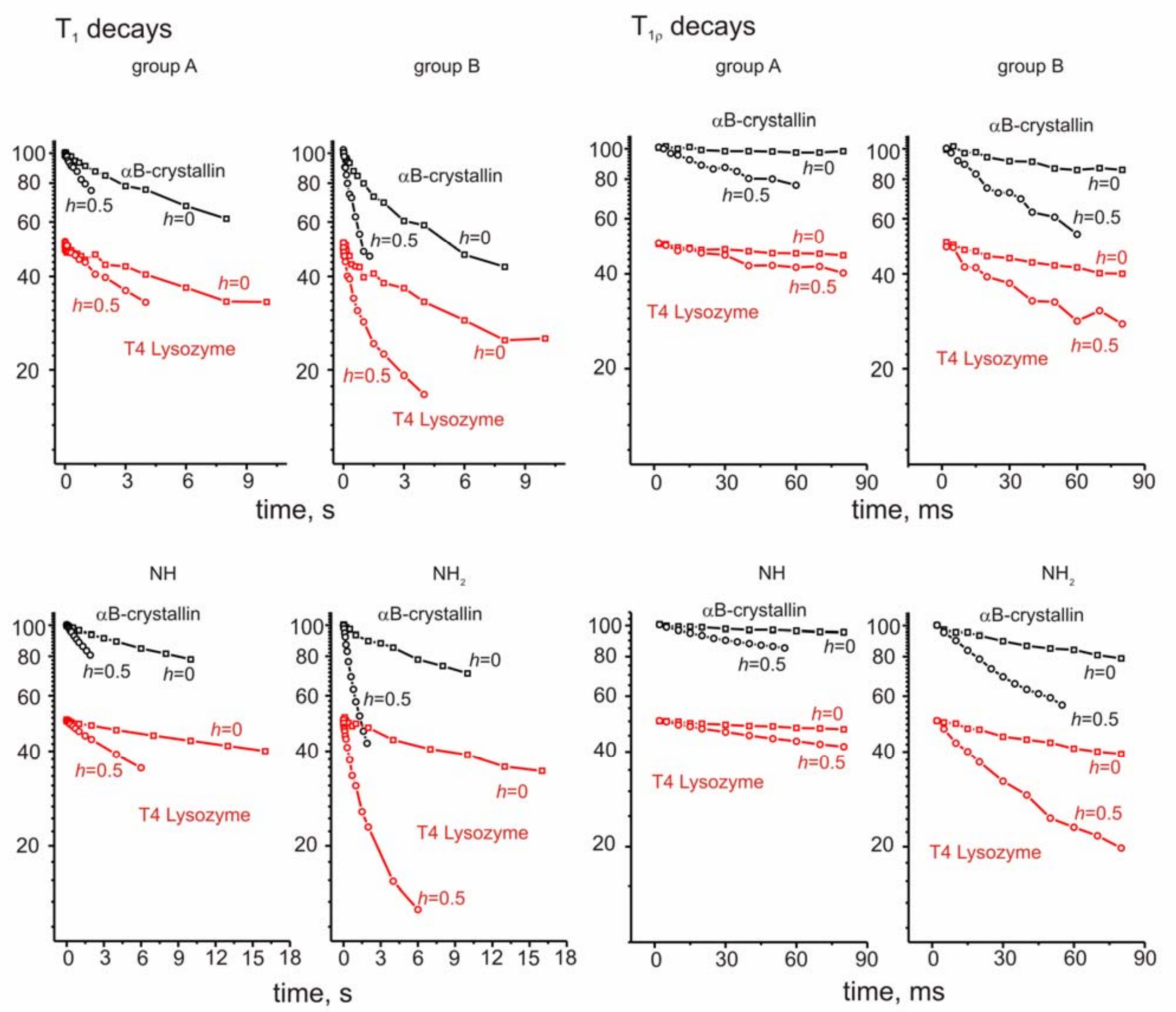

Fig. 16. Typical examples of the relaxation decays in αB-crystallin and T4 lysozyme. (Decays are from Ref. [148]).

It follows from fig. 16 that relaxation decays cannot be described by a single exponential function – they are multi-exponential in nature. This proves the suggestion that there is an inhomogeneous distribution of dynamic parameters in the protein. The environment governing the distribution of microdynamic parameters is dependent on hydration, as is indicated from the picture. The form of the decays changes with increasing sample humidity. To unify the analysis of all data we used a widely known approach. From the initial part of the decays we determined the mean relaxation rates and then compared these at different hydration levels.

In order to define the mean relaxation rate, all decays were fitted with a bi-exponential function:

$$I(t) = P_a \exp(-t/T_a) + P_b \exp(-t/T_b) \tag{3.1}$$

where T_a, T_b and P_a, P_b are the relaxation times and the weightings of each components, respectively. The mean relaxation rate is defined as:

$$R_{1,1\rho} = \frac{1}{P_a + P_b}\left(\frac{P_a}{T_a} + \frac{P_b}{T_b}\right) \tag{3.2}$$

The main advantage of the method is that the mean relaxation time can be defined with minimal inaccuracy in spite of the subjectivity of the decay decomposition. It should be noted that there is no necessary physical meaning for a bi-exponential decomposition; it is just a mathematical minimal-parameter treatment.

In general, relaxation times are defined by the spectral density functions (Eqs. (2.36) and (2.38)), which contains information about molecular motions. The aim of a researcher is to restore the correlation function which is a Fourier transformation of $J(\omega)$. However, a few relaxation times cannot define the whole form of the spectral density function. One has to measure detailed temperature and/or frequency dependencies of relaxation times to determine the number of motional processes and their parameters. This is a very time consuming process and hardly suitable for the characterization of hydration effects on microdynamic parameters. Nevertheless, such work for two different hydration levels (h=0 and h=0.39) of hen egg white lysozyme was done by Krushelnitsky *et al.*[122] The analysis of the ^{13}C relaxation times measured at different conditions showed that for adequate description of protein dynamics (at least) three motional regimes should be considered. These are fast methyl group rotations and low-amplitude molecular motions with correlation time around 10^{-5} s and 10^{-9} s. Both of the low-amplitude motions, which are different in nature, persist in the dry protein but with strongly restricted amplitudes. The slower motion is the conformational transition between different energy minima and does not lead to a change of secondary structure. The faster motion is the vibrations within one energy minimum. The authors found that the correlation time of the motions do not depend on the hydration level, but only motional amplitudes do. Similar result were obtained by Hackel *et al.* by directly measuring the

^{1}H-^{13}C order parameters for backbone and side chain atoms in cold shock protein.[156] Concerning CH3 groups dynamics, it was found that the motional parameters driving fast methyl rotation do not depend on the hydration level at all.

Our analysis is based on the assumption that the existence of a hydration dependence for carbon relaxation times is due to changes in amplitudes of nanosecond and microsecond motions. The relaxation rates in the case of the two independent motions (providing the condition $\tau_s >> \tau_f$) can be written according to the "model-free" approach:

$$R_{1,1\rho} = \frac{1}{T_{1,1\rho}} \sim \left(1 - S_f^2\right) \frac{\tau_f}{1 + \left(\omega \tau_f\right)^2} + S_f^2 \left(1 - S_s^2\right) \frac{\tau_s}{1 + \left(\omega \tau_s\right)^2} \tag{3.3}$$

here ω is a resonance frequency (in case of T_1 the Larmor frequency of the nuclei, in case of $T_{1\rho}$ the spin-lock pulse frequency); τ_f and τ_s are the correlation times of fast and slow motions, respectively, S_f^2 and S_s^2 are order parameters for two motional regimes. After taking into account that the fast motion is in the nanosecond timescale and the slow motion is in the range of 10-100 µs, the only significant terms in the Eq. (3.3) come from the amplitudes. Then, the relaxation rate in the laboratory frame depends on the amplitude of the fast motion. The relaxation rate in the rotating frame comprises contributions from both fast and slow motional regimes amplitudes:

$$\begin{aligned} R_1(h) &\sim \left(1 - S_f^2(h)\right) \\ R_{1\rho}(h) &\sim S_f^2(h)\left(1 - S_s^2(h)\right) \end{aligned} \tag{3.4}$$

In spite of the fact that the relaxation rate in the rotating frame feels both amplitudes of motion, it is possible to define the hydration dependence of slow motion amplitude by a mathematical manipulation of the above equations:

$$1 - S_s^2(h) \sim \frac{R_{1\rho}(h)}{1 - \frac{R_1(h)}{R_1(0)}\left(1 - S_f^2(0)\right)} = R_{1\rho}^*(h) \tag{3.5}$$

within the brackets the hydration level h is denoted. Thus, if we know the value of the amplitude of fast motion in the dry sample, then from the measured relaxation rates R_1 and $R_{1\rho}$, it is possible to determine the amplitudes of slow motions as a function of the humidity level. The exact "dry" values for amplitudes in case of T4 lysozyme and αB-crystallin have not yet been defined. However, these values are already published for the hen egg lysozyme:[122] for the CH group it was around 0.98 and for the CH_2 group – 0.95. It is believed that the magnitude of the motional amplitude probed by carbon nuclei in different lyophilized globular proteins is rather similar. Thus, in the current work, we take these values for our systems. It is worth noting that the motional amplitude of NH groups is dependent on the hydration level. [156] Thus, such an approach does not fit for the interpretation of ^{15}N relaxation data. A corresponding approach for the analysis will be presented below.

3.2.3. *Nanosecond dynamics probed by ^{13}C-T_1*

The dependencies of ^{13}C R_1's, thus, amplitudes of fast motion, on hydration for different spectral groups are presented on the figure 17.

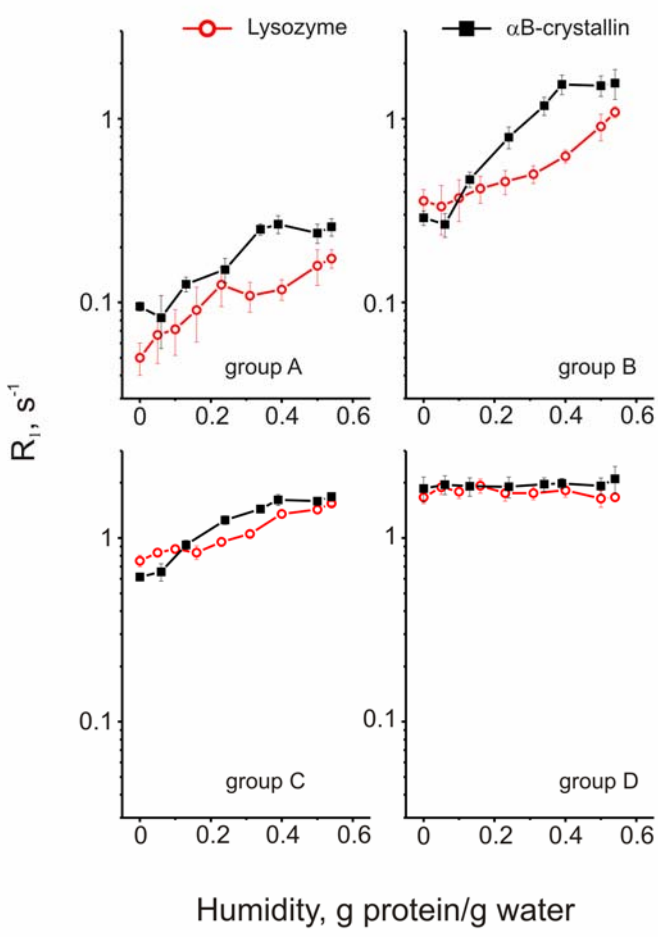

Fig. 17. Carbon relaxation rates R_1 as a function of the humidity level for different bands. The data are published in Ref. [148].

The first issue to discuss is the behaviour of the CH_3 groups (D group). The methyl protons undergo large amplitude fast rotation around the symmetric axis, thus their decays are fast and the relaxation rates R_1 are rather high. The prominent feature of such carbon motions is the lack of hydration dependence. This result is not new and is in the accordance with the previous findings.[41,122,154] The independence of the methyl rotation from the water content can be explained by the hydrophobic nature of CH_3 groups. They do not directly interact with water molecules and their mobility should not depend on the H_2O content in protein sample.

The amplitudes of fast motions for other groups are smaller than for methyl carbons and are dependent on the hydration level. The amplitude increases upon hydration rather monotonically. αB-crystallin amplitudes reach a plateau value at the h~0.35-0.4, while T4 lysozyme growth continues through all measured hydration levels. Such differences between proteins are probably due to differing hydrophobicity. T4 lysozyme has more hydrophilic groups on the surface of the globule compared to αB-crystallin; thus, it is likely that for the saturation of lysozyme more water is required. If this explanation is correct then the plateau for the T4 lysozyme is still not reached at the hydration point of 0.6. The conclusion could be made that the amplitude of the fast motion increases with increasing humidity until it becomes the same as in the solution.

3.2.4. *Microsecond dynamics probed by ^{13}C-$T_{1\rho}$*

To assess the water influence on the slow molecular dynamics of proteins we implement the above approach (Eq. (3.5)). Figure 18 demonstrates the hydration dependence of the experimentally measured relaxation rates in the rotating frame and $R^{*}_{1\rho}$. The data for the CH_3 group is not presented here because this group has a very slow $R_{1\rho}$ relaxation rate (on the order of 1 s^{-1}) endangering the probe from overheating during long spin-lock pulses.

As is depicted in the figure, the variation between values of 0.95-0.98 for the fast order parameter of the backbone does not change the general behaviour of the humidity dependence of $R_{1\rho}(h)$. A similar trend was found for side chains.

The growth of the relaxation rate $R_{1\rho}(h)$ under hydration in the rotating frame differs from R_1. The amplitude of slow motions increases abruptly at low water content, and after reaching h~0.15-0.25 there is a weak dependence. The difference in the form of the relaxation rate functions $R_1(h)$ and $R_{1\rho}(h)$ is in agreement with the nature of the fast and slow motions in proteins. Slow motions are correlated rearrangements of several structural units with a large amplitude. These motions are due to transitions between different energy minima. In dry proteins, barriers between minima are high and the addition of water reduces their height.[122,145]

Nanosecond motions correspond to non-correlated librations of protein atoms within the spatial restrictions. For such types of motions the presence of free volume around the moving unit is necessary. Hydration weakly influences the globule interior, but on the surface of the protein it causes large changes in the amplitude of motions upon hydration, until the saturation point is reached.

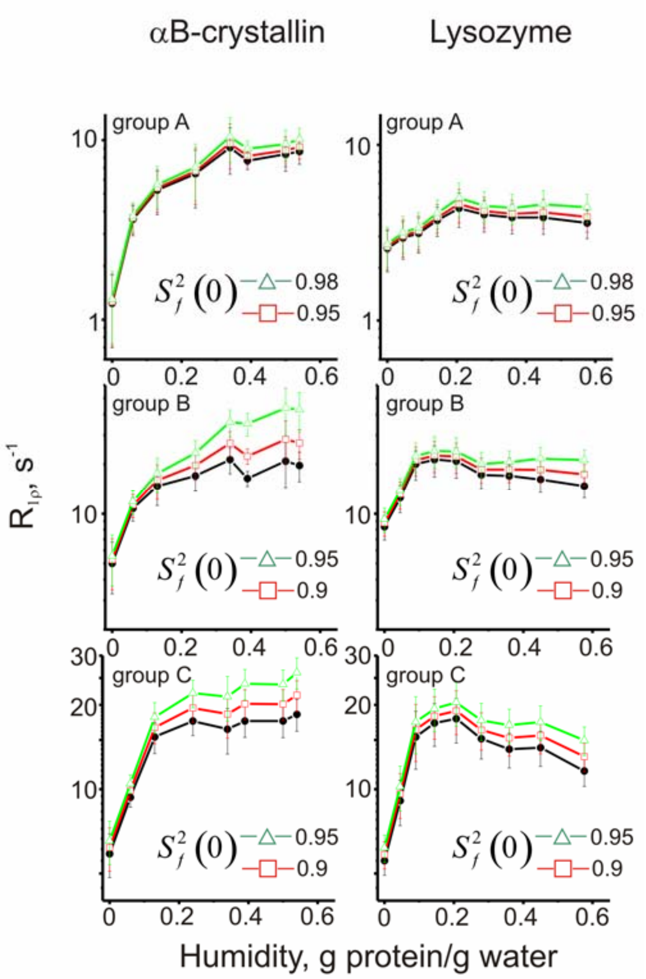

Fig. 18. Hydration dependencies of the $R_{1\rho}$ (black line with solid circles) and the $R^*_{1\rho}$ (green and red lines with open symbols) calculated for various order parameters at different carbon sites of protein. Figures are replotted from Ref. [148].

3.2.5. *Nanosecond to microsecond protein dynamics probed by* $^{15}N - T_{1,1\rho}$

In addition to carbon relaxation, nitrogen relaxation rates were also analyzed. There is a difference between the hydration response of motions for nitrogen and carbon groups in the protein backbone. The unique feature of N-H bond motions is the independence of the amplitude on water content. The explanation for this difference is an existence of intramolecular hydrogen bonds which stabilize the secondary structure of the protein and governs the motions of N-H and C=O groups.[156] Thus, the changes in relaxation rates of backbone nitrogens are a result of correlation time variations:

$$R_1 \sim \frac{\tau_f(h)}{1+\left(\omega\tau_f(h)\right)^2} \qquad (3.6)$$
$$R_{1\rho} \sim \frac{\tau_s(h)}{1+\left(\omega\tau_s(h)\right)^2}$$

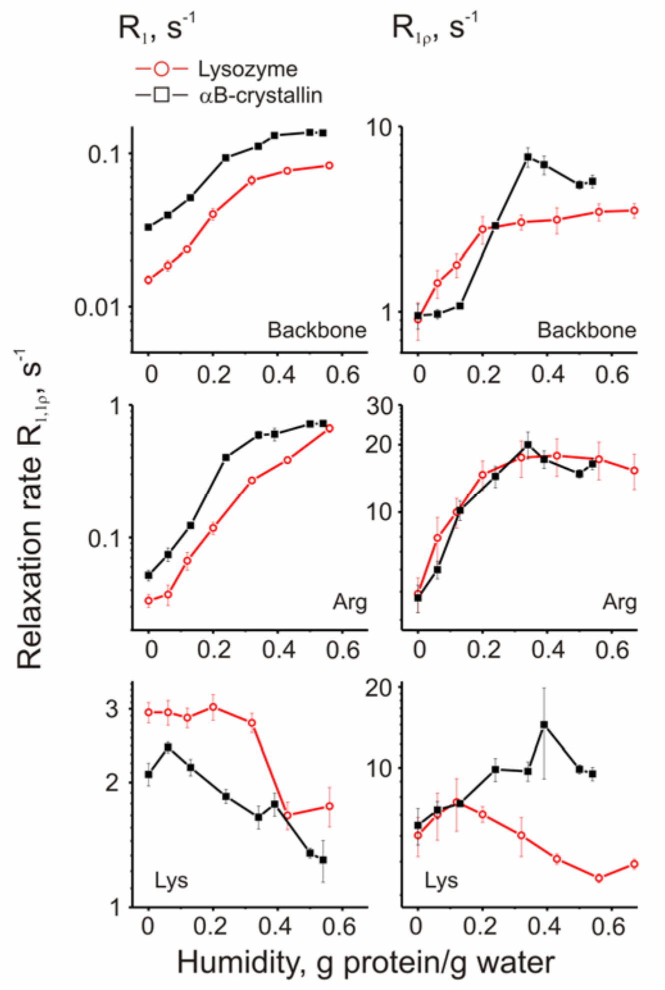

Fig. 19. ^{15}N R_1 and $R_{1\rho}$ as a function of the humidity for different protein sites. (Data are taken from Ref. [148])

Figure 19 demonstrates R_1 and $R_{1\rho}$ for different nitrogen groups as a function of hydration. The behaviour of NH_3 groups (Lys peak), in contrast to CH_3 groups, has a pronounced hydration dependence. It is a consequence of the hydrophilic nature of this group located mainly on the protein surface. Water molecules directly influence NH_3 groups by lowering the energy barriers of proton rotation. From fig. 19 we see that humidity leads to a decrease in relaxation rates for the Lys side chains. Since the amplitude of motion hardly decreases upon hydration, then the changes in the relaxation rates of these groups are most probably governed by the shortening of the correlation time. An analogous decrease of the slow correlation time is also typical for NH_3 as evident from $R_{1\rho}(h)$ behaviour. Relying upon the fact that acceleration of motion results in relaxation rate decrease, we can conclude that the correlation time of NH_3 rotation is faster than the inverse Larmor frequency (fig. 20). The correlation time decreases and shifts outwards from the maximum sensitivity of the relaxation experiment.

The ^{15}N relaxation rates in the laboratory and rotating frames for the backbone grow upon hydration. This increase means that the correlation time of motions changes towards the inverse Larmor (R_1 case) or spin-lock pulse frequency ($R_{1\rho}$). It is unlikely that during incremental hydration nitrogen site motions slow down. Thus, correlation times of the fast motions decrease with humidity levels coming towards the range of the maximum sensitivity for the ^{15}N-R_1

experiments (tens of nanoseconds). The same occurs for the $R_{1\rho}$-humidity profile of NH. The correlation times become shorter and closer to the range of tens of microseconds.

However, the R_1's of the backbone do not increase monotonically. The behaviour is sigmoidal: there is an initial slow increase up to *h*~0.15, then sharper growth to *h*~0.4, and again weak dependence at higher hydration levels. Analogous sigmoidal trends in the mobility on nanosecond scales was detected by Roh *et al.*[41]

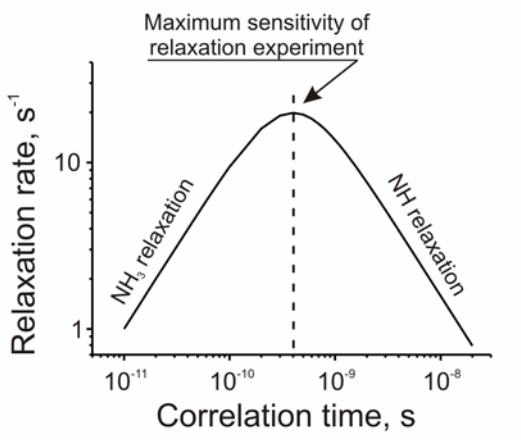

Fig. 20. The dependence of relaxation rate on the correlation time of motion.

The relaxation rates of the side chain atoms (Arg peak) can change as a result of the alteration of both the correlation time and amplitude. We are not able to distinguish between the contributions without additional measurements.

Analogous to the $R_{1\rho}$ of CH and CH_2 groups the relaxation rate in the rotating frame for NH and Arg peaks has a plateau value at around *h*=0.2, whereas R_1 continues to increase.

3.2.6. *Ultra-slow dynamics measured by ^{15}N CODEX*

To probe the hydration response of slower timescale dynamics, the water content dependence was measured by ^{15}N exchange experiments on T4 lysozyme. We can only analyze the NH signal since other peaks are low in intensity. During the mixing time spin-lattice relaxation occurs as well. In the original CODEX experiment the compensation of spin-lattice relaxation is built into the pulse sequence. In our work we used a modification of the initial pulse sequence. Here, the relaxation part was skipped. To compensate for this, we divided the intensity of the signals at different mixing times by the relaxation time decay measured by the Torchia pulse sequence. The other interfering effect reflected in the exchange measurement is proton-driven spin diffusion. It has the same effect on the exchange spectra as molecular reorientations, and one faces a problem with the separation of both effects when both rates are similar.

The ways to decrease the PDSD rate are implementing proton decoupling, which suppresses X-^1H dipolar coupling, or diluting of the spin system.[68] The first method is dangerous for the sample and the probe-head as it uses long high-power decoupling pulses. The latter is hardly practical in our case, since the signal-to-noise ratio would not allow us to obtain reliable information. Thus, we attempted to distinguish between two effects by measuring at different temperatures.[124] Molecular reorientations are thermally activated and their rates depend on temperature. If there are any variations in the correlation times of the molecular motions, they would be seen in the initial time dependence of the signal intensity. In the case when the frequency of the molecular process is comparable or less then the PDSD rate, then it is impossible to register them.

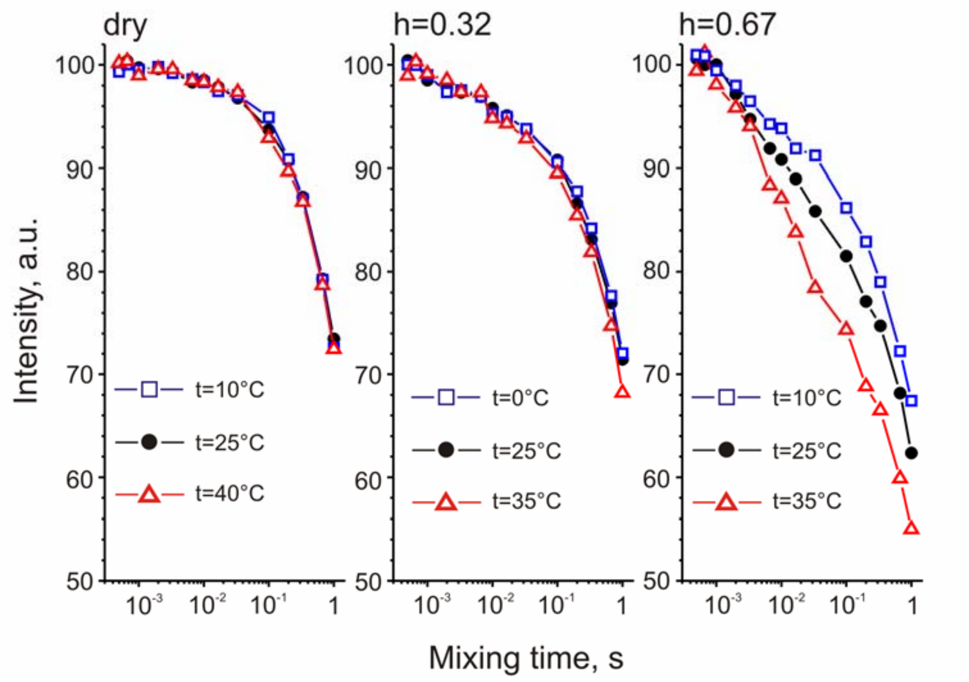

Fig. 21. ^{15}N CODEX decays for T4 lysozyme measured at different humidity levels and temperatures. Data are published in Ref. [148]

We can safely ignore the possible influence of direct ^{15}N-^{15}N spin diffusion (in contrast, direct ^{13}C-^{13}C spin-diffusion was found to significantly disturb exchange measurements[157]). The spin diffusion rate is inverse to the sixth power of the distance and is directly proportional to the fourth power of magnetogyric ratio. The distance between nitrogens in proteins backbone quite large, while their γ is small, making this phenomenon not very effective.

Figure 21 demonstrates the temperature dependence of the exchange decays at different humidity levels. Temperature induced variations of the decays exist only at the highest studied humidity levels, while decays in dry and partially hydrated samples for different temperatures are indistinguishable. Thus, slow millisecond to second molecular motions are absent in dried proteins, but are intrinsic to some proteins in the hydrated state. The same absence of slow motions in dehydrated protein powders and at moderate humidity was observed by Krushelnitsky *et al.*[124]

At h=0.67, exchange decay includes both contributions from PDSD and molecular reorientations. It is possible to exclude spin diffusion by measuring exchange experiments at elevated temperatures where the correlation time of molecular motion is too short for CODEX measurements. However, high temperatures are dangerous for proteins as they sometimes induce irreversible changes in the protein structure.

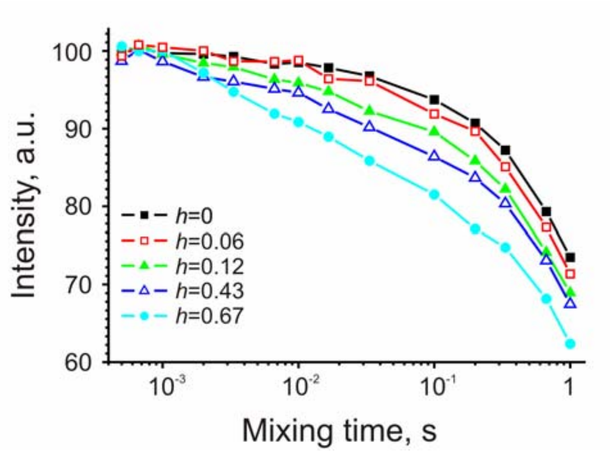

Fig. 22. The dependence of ^{15}N main peak of T4 lysozyme CODEX decays on the humidity level.[148]

The decay becomes faster as the sample is hydrated (fig. 22). This is due to structural rearrangements during hydration. It is known that the structure of proteins differs slightly in the dehydrated and native states.[158] Because of the inverse sixth power of distance for the PDSD rate, even minor changes in structure influence the exchange rate. Gradual structural changes are reflected in variations of the exchange decay shape.

In general, it is possible to not only capture the slow exchange processes by the CODEX experiment, but also to define the motional parameters characterizing the dynamics. The mixing time dependence gives direct access to the correlation function without any approximations. The dependence of the signal on the evolution time would allow estimations of the geometry of motion and the number of subconformations involved in the motional process.[96] Investigations of exchange decays governed by spin diffusion showed that this process in proteins cannot be described by a single exponent, since there is a distribution of distances between atoms in complex samples.[68,124] Moreover, the component containing the dynamic information in the powder samples can also possess a non-exponential form. To get exchange purely due to motions, one should exclude the effect of spin diffusion from the experimental data. In our case, the decomposition of the experimental decays will be ambiguous and uncertain. Thus, we do not try to make any quantitative analysis of the obtained data.

We also made an attempt to measure exchange on carbon nuclei. The signal-to-noise ratio for the natural-abundance ^{13}C spectra was so low that it was not feasible to obtain smooth decays.

Despite the fact that it was not possible to extract motional parameters from the ^{15}N exchange measurements carried on T4 lysozyme, we were able to compare qualitatively the slow motions in our protein with those of other proteins – barstar,[105,124] small proteins ubiquitine and colicin, and multidomain triblock protein ACA;[136,137] and the SH3 domain.[138]

As was stated in Ref. [136,137], there are no slow motions in small proteins, such as ubiquitin and colicin, or their amplitude is too small to be registered by exchange NMR methods. In contrast, in the triblock protein there is a significant amount of slow mobility which follows from the difference in the signal intensities at various mixing times. Since almost all residues in the A domains in the ACA protein show exchange with similar correlations times, the authors conclude this domain moves as a whole. In the SH3 domain slow millisecond motions were detected for approximately half of the residues in the backbone. Correlation times of this motion for different residues were in the range of 1-3 s. The allied correlation times suggest that a large number of amino acid residues participate in a collective slow motion. Not only unstructured residues take part in this type of motion, some of the structured residues also participate.[138]

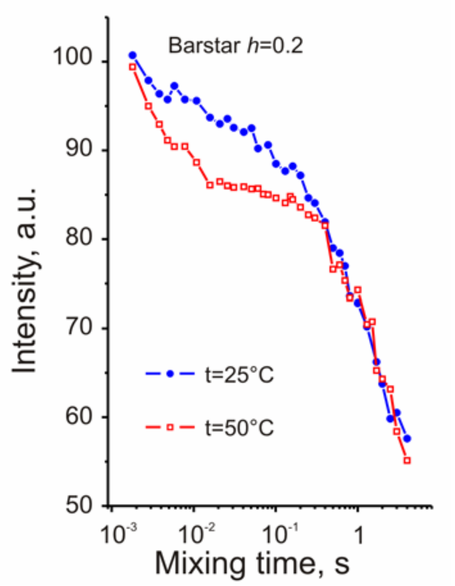

Fig. 23. ^{15}N exchange decay of barstar measured by time-reversed ODESSA.[124]

Another example of the existence of slow motions was found in barstar.[105,124] This protein has a highly negative charged surface assisting large-scale conformational motions. These motions were detected and characterized by exchange spectroscopy. Slow barstar backbone motions are activated at *h*=0.2. These are infrequent, high-amplitude transitions between different protein subconformations. Large activation energies confirm the nature of this motion. It is interesting to compare slow dynamics of this protein with the one found in T4 lysozyme.

The differences between exchange behaviour in barstar and T4 lysozyme are (i) the onset of the slow dynamics of barstar is already detected at *h*=0.2, whereas for T4 lysozyme no exchange is visible till the highest humidity levels; (ii) the form of the exchange decays are different for both proteins (see Fig. 23 and Fig. 21).

We suppose that these differences result from the different nature of the motion for these proteins. Barstar possesses internal mobility which is necessary for its function. It is unlikely that the rigid and well-packed T4 lysozyme has such a significant portion of large scale internal mobility. We believe that the detected motion seen in the exchange experiments is from librations of the whole globule in the glassy matrix of the hydrated protein sample. The humidity level of *h*=0.5 is considered to be high enough to cover the protein molecule with a water bilayer. At this point water acts as a lubricant enabling restricted reorientations of the protein globules relative to each other.

Powder samples of proteins have been studied before in order to capture slow motions. However, no indication of millisecond motional processes was obtained. The reason could be that some methods are designed for registering internal motions and are not sensitive to the motion of the molecule as a whole. Some researchers did not reach high hydration levels[159] – at low water contents millisecond to second processes do not occur.

Thus, we obtained the first indication for the existence of whole protein molecule librations within the glassy protein matrix at high humidity levels.

3.3. Conclusions

In this section, the hydration response of the internal protein dynamics was studied in a wide frequency range starting from picosecond up to millisecond motions. We found that motional modes with different correlation times react differently to the increase of water content. The fast molecular motions become increasingly prominent in the entire range of investigated hydration levels until the saturation point is reached. For the protein sites stabilized by hydrogen bonds, the enhancment of mobility is characterized by the acceleration of motions. For other sites, hydration leads to higher amplitude motions. The saturation point is not unique for all proteins, and is likely to depend on the hydrophobicity of the protein.

Submicrosecond and microsecond motions do not increase monotonically. The sharp growth in flexibility corresponds to low hydration levels. A h>0.2 the increase slows down and finally comes to a plateau.

This difference corresponds to the nature of the motions. The formation of free volume around the mobile unit during the rehydration facilitates motions within one energy minimum. The effect is visible until the fast motions coincide with those in the solution state.

For the enhancement of microsecond mobility, it is important to decrease the energy barriers between different minima corresponding to the explored subconformations. Even low hydration levels significantly reduce potential barriers. This phenomenon is reflected in the behaviour of the hydration dependence of jumps between energy minima.

There is one type of motion that does not depend on hydration at all – fast CH_3 group rotation. This independence is caused by the hydrophobic nature of the CH_3 group. Analogous NH_3 end groups are sensitive to the presence of water.

We studied two proteins with different properties, and showed that the qualitative hydration response of both proteins is similar. The similarity of the hydration response for cold shock protein was also detected by Hackel *et al.*[156] From this, one can suggest the generality of the behaviour for proteins.

It was found that in highly hydrated protein samples millisecond librations of the whole protein globule can occur within the matrix formed by hydrated protein molecules.

We revealed the co-incidence of protein internal mobility in the hydrated and solution states on the timescale range where $\tau_C \leq 10\ \mu s$. Consequently, it is possible to study protein dynamics by solid-state NMR and to use the obtained information about motions in order to explain functionality of proteins. The water content needed for the restoration of native-like dynamics should be more than around 50% of H_2O (by weight) depending on the protein. Thus, in the microcrystalline state, where the hydration reaches 60-80%, the parameters describing mobility should correspond to those in the liquid state.

4. Microsecond internal molecular motions in fully hydrated microcrystalline proteins studied by relaxation solid-state NMR

In the previous section we presented evidence that μs molecular dynamics in the fully-hydrated state and in solution are nearly identical. Thus, we can use results obtained from microcrystalline samples to describe the dynamics on proteins' in the native state. $T_{1\rho}$ relaxation measurements are most suitable for investigating μs motions. In this section, I would like to present ^{15}N $R_{1\rho}$ relaxation data measured for a microcrystalline protein - SH3 domain of chicken α-spectrin. Experiments performed at different spin-lock field strengths expand the sensitive frequency range of the method. The usage of perdeuterated microcrystalline proteins allows one to obtain information with site-specific resolution. The comparison between relaxation parameters characterizing protein motions on different timescales gives an opportunity to obtain more detailed information about internal motions occurring in the protein molecule. The results of these experiments and their discussions are published in our paper.[160] My contribution was processing and analysis all of the experimental data, and I took part in all of the discussions and drawing conclusions.

4.1. Samples and experimental conditions

^{15}N, ^{2}H-enriched SH3 domain of chicken alpha-spectrin was prepared according to the protocol described by Chevelkov *et al.*[129] Protein microcrystals were grown in a buffer containing 10% water and 90% D_2O. Thus, the exchangeable deuterons in labile sites were back-substituted by protons. Afterwards, protein samples were put into MAS NMR rotors (3.2 mm and 4 mm).

Because the dynamic measurements were performed in the perdeuterated microcrystalline state, we benefit by overcoming several challenges. First, it is possible to obtain liquid-like resolved spectra. Small efficiency of the interaction between rare nuclei and the proton reservoir in ^{1}H-diluted samples results in weak line broadening due to dipolar coupling. In microcrystals each protein molecule has the same surrounding as the others. Consequently, an inhomogeneous distribution of chemical shifts does not appear. Second, protons possessing high sensitivity are well-suited for the measurement of spectra with good signal-to-noise ratio in a short experimental time. The third advantage concerns dynamical measurements. In proteins with a natural abundance of ^{1}H nuclei, there is a high rate of polarization transfer caused by spin diffusion. This process equalizes apparent relaxation rates at different protein sites. Spin diffusion does not contain dynamic information, and its rate depends strongly on the interproton distance. Dilution significantly increases the ^{1}H-^{1}H distance, making the spin diffusion contribution to the relaxation rate negligible. The same proton dilution prevents the high-efficiency of the spin-spin contribution to the relaxation rates in the rotating frame. Summarizing all these features, perdeuterated microcrystalline proteins are perfectly suitable for site-specific dynamic measurements.[24,76,78–82,161]

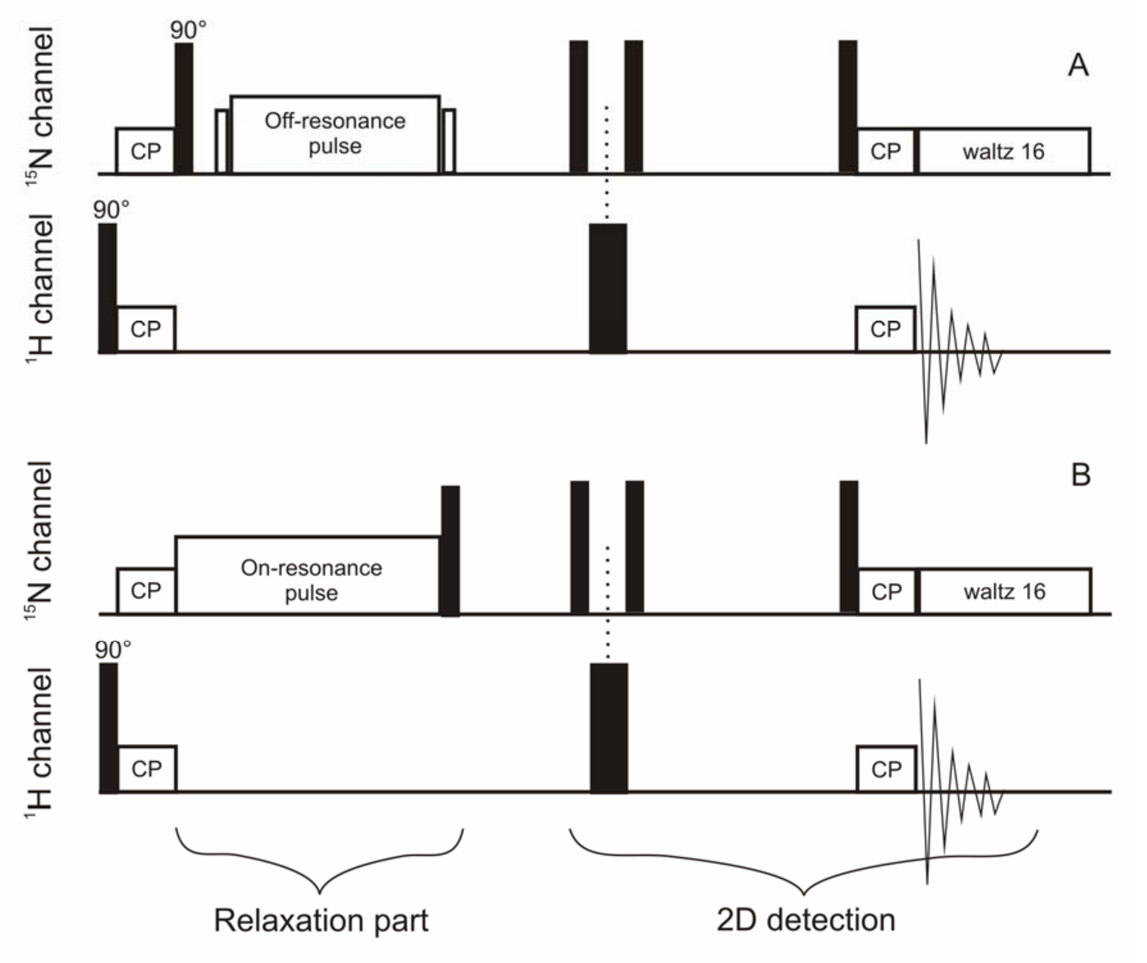
90°
Off-resonance pulse
CP
waltz 16
A
^{15}N channel
90°
CP
CP
^{1}H channel
On-resonance pulse
CP
waltz 16
B
^{15}N channel
90°
CP
CP
^{1}H channel
Relaxation part
2D detection

Fig. 24. Pulse sequences for $T_{1\rho}$ measurements with resonance off-set of spin-lock pulse frequency (A) and without off-set (B). Black rectangles denote 90° and 180° rf-pulses. CP means cross-polarization.[24]

All experiments were performed on Bruker Avance spectrometers with proton resonance frequencies of 400 and 600 MHz. Off-resonance $R_{1\rho}$ experiments were carried out with B_{1e}=34.9 kHz and 46.3 kHz and the MAS rate of 10 kHz at t=14°C and 24°C using the 4mm probe; the off-set angle θ yielded 24° (B_{1e}=34.9 kHz) and 14° (B_{1e}=46.3 kHz). The maximum spin-lock pulse length was set to 100 ms. Before performing experiments, the nutation calibration was carried out to make sure that the resonance off-set was the same for all the experiments. The on-resonance experimental conditions were: MAS rate of the 3.2 mm probe – 20 kHz; applied on-resonance spin-lock field 8.1 kHz and 13 kHz; temperatures were 10° and 27°C. Before all measurements, the temperature inside the probeheads was calibrated to account for the frictional heating effects at different frequencies of magic-angle spinning.

The pulse sequences for the on-resonance and off-resonance $R_{1\rho}$ experiments are presented in fig. 24. The pulse sequence consists of two parts: the relaxation time measurement and proton detection to enhance the sensitivity. After proton magnetization is placed in the *xy* plane, the cross-polarization process occurs to transfer polarization from abundant ^{1}H nuclei to rare ^{15}N. Then the ^{15}N magnetization relaxes during the spin-lock pulse with or without frequency off-set. Then, proton detection follows after the transfer of the X magnetization to protons using cross-polarization.

2D spectra for six different spin-lock pulse durations were recorded to obtain the relaxation decay of the individual signals.

4.2. The results

Figure 25 demonstrates 2D ^{15}N-^{1}H correlation spectra of SH3 domain of α-spectrin with residue assignment.

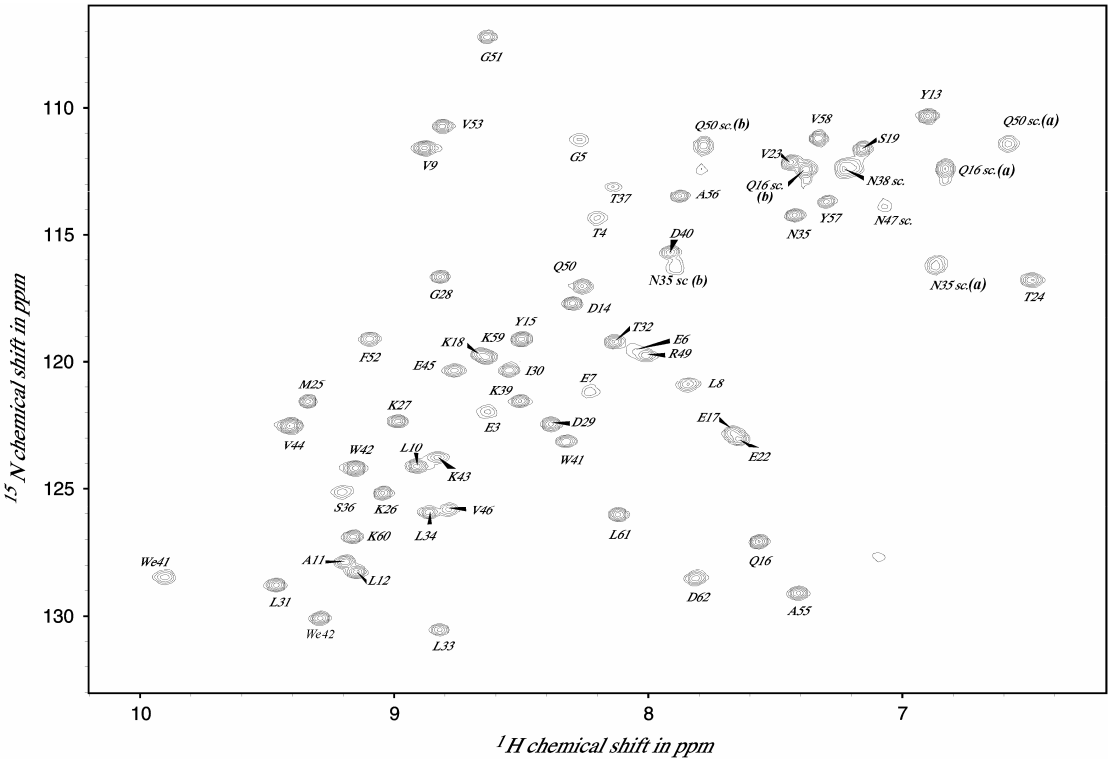

Fig. 25. 2D ^{15}N-^{1}H correlation spectra of the proton-diluted SH3 domain of α-spectrin with the residue assignment measured at 600 MHz.[24]

The linewidth of approximately 17-35 Hz obtained at moderate spinning rates provides good, resolved NMR spectra without the implementation of homonuclear decoupling.[24] In total, the SH3 domain contains 62 backbone amino acid residues; however, only 46 backbone peaks and 8 side chain peaks were observed. The obscured residues belong to the N-terminus of the protein backbone (residues Met1-Lys6) and residues that are located in the loops connecting β-sheets. One of the reasons for the absence of these peaks in the spectra is due to line broadening, which arises from an increased mobility in the corresponding site of the protein.

4.2.1. *Relaxation data analysis*

The intensity decays of the individual peaks acquired at different spin-lock pulse durations are depicted in figure 26. We took relaxation curves to be single-exponential since they were measured for residues in identical surroundings. The relaxation rate values were found after fitting the measured data to a single-exponential decay according to the equation:

$$I(t) = I(0)\exp\left(-\frac{t}{T_{1\rho}}\right) \tag{4.1}$$

here I is intensity and $T_{1\rho}$ is the relaxation time constant.

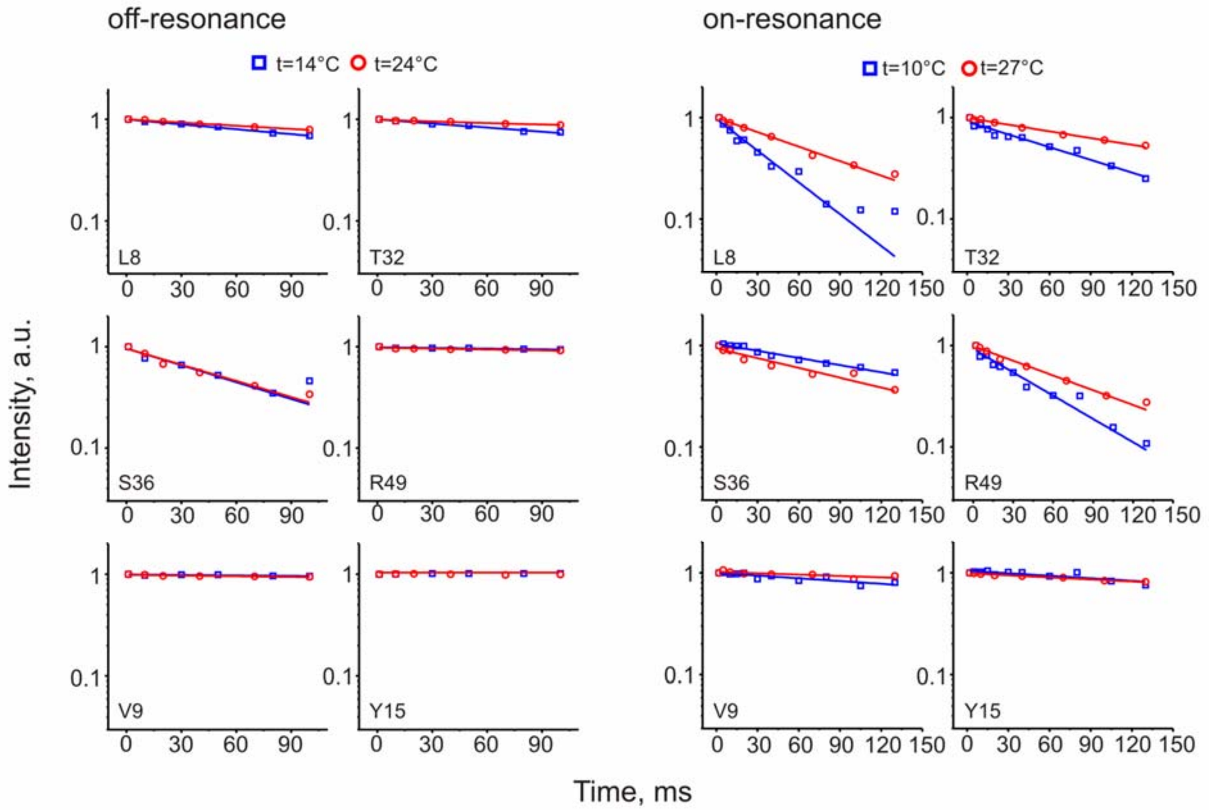

Fig. 26. Examples of the $T_{1\rho}$ decays measured with on-resonance frequency of spin-lock pulses (right), and with an off-set (left). The solid lines correspond to single-exponential fitting curves. Relaxation data are published in Ref. [160]

The fitting quality was different for individual residues because of differing signal-to-noise ratios, and because the cross-polarization efficiency is not uniform for each peak throughout the protein molecule. Moreover, if the spin-lock pulse is too short to provide significant intensity decay due to relaxation, then $T_{1\rho}$ values cannot be defined accurately; but a lower limit can be estimated. The maximum spin-lock field times used during the experiments were between 100-130 ms, and were not long enough for the accurate determination of the relaxation rates for some residues. Using longer pulses could cause harm to the sample. Relaxation rates in the on-resonance experiments were generally faster, and we were able to define them quite reliably.

4.2.2. *Relaxation rate constants and dynamics*

Site-specific fitting results for the $T_{1\rho}$ experiments at different parameters are presented in figure 27. The main feature from this figure is the notable alteration (up to 45-fold) of rotating frame relaxation rates as a function of the amino acid location within the protein structure. The various relaxation rates demonstrate the lack of influence from spin diffusion on the experimentally measured dynamic parameters in deuterated microcryastalline samples. This conclusion is also supported by the fact that the relaxation rates are temperature dependent ($R_{1\rho}$‘s measured at 10°C are usually larger than $R_{1\rho}$‘s measured at 27°C). As spin-diffusion rates are independent of temperature and a function of inter-proton distance, the observed variations of relaxation rates with temperature suggests that the origin of relaxation is due to molecular motions. Thus, by measuring $R_{1\rho}$, we detect heterogeneity in protein dynamics, particularly on the submicrosecond to microsecond timescale.

In general, relaxation rates are elevated at the N and C-termini of the backbone, as well as in side chains. Increased mobility is also observed at the ends of β-sheets and in the loops between. Nevertheless, it is interesting to emphasize that even within a few β-sheets relaxation rates fluctuate significantly. This was also detected by other authors in their microcrystalline protein studies based on experimental measurements of relaxation rates in laboratory and rotating frames.[53,125,127,131–134]

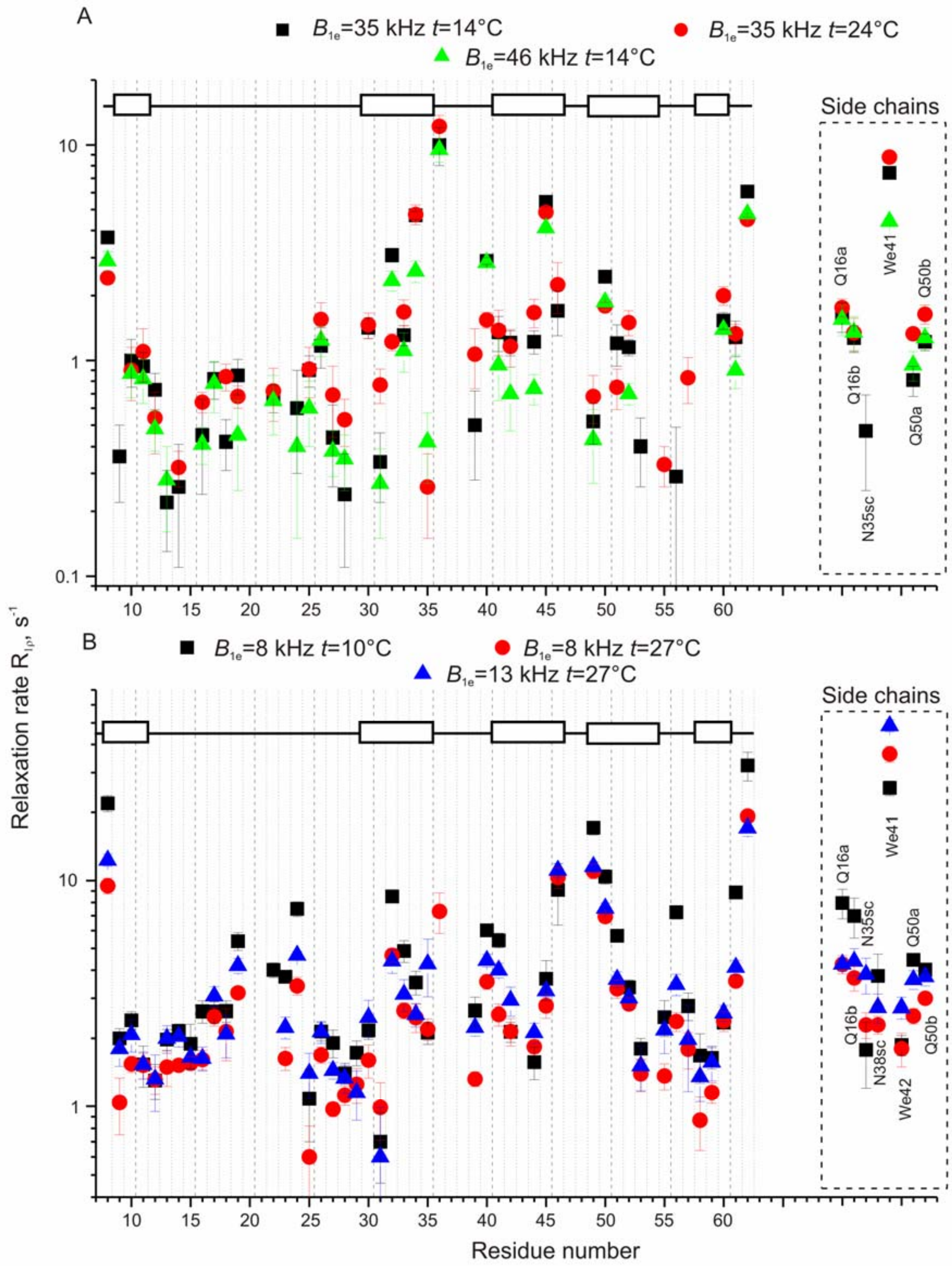

Fig. 27. $R_{1\rho}$ relaxation rates as a function of residue number for SH3 domain measured in off-resonance (A) and on-resonance modes (B).(Present data are from the Ref. [160]) Straight solid lines and rectangles in the upper part of each picture denote the secondary structural elements: loops ("unstructured" regions) and β-sheets, respectively.

4.2.3. *Correlations*

In some of works,[53,131] correlation between dynamic parameters describing molecular mobility on different timescales was observed. At the moment, relaxation rates in the laboratory frame (~ns timescale),[127] motionally averaged dipolar couplings (up to ~several μs)[126] and exchange measurements (ms-s range)[138] are available in the literature for SH3 domain of α-spectrin. Fig. 28 shows a comparison for the general behaviour of the NMR parameters describing SH3 domain. The first notable feature is that R_1 and $R_{1\rho}$ profiles are similar. Though these two relaxation rates characterise mobility on different timescales (nanosecond in the case of R_1 and microsecond for $R_{1\rho}$), there still exists a correlation between them. Those residues which possess increased $R_{1\rho}$ values also have increased R_1 relaxation rates. There are two possible explanations for this effect. The first explanation found in the literature, is that there exists a correlation between nanosecond and microsecond motions. The hypothesis is that fast motions somehow facilitate the onset of slow dynamics.[4,53]

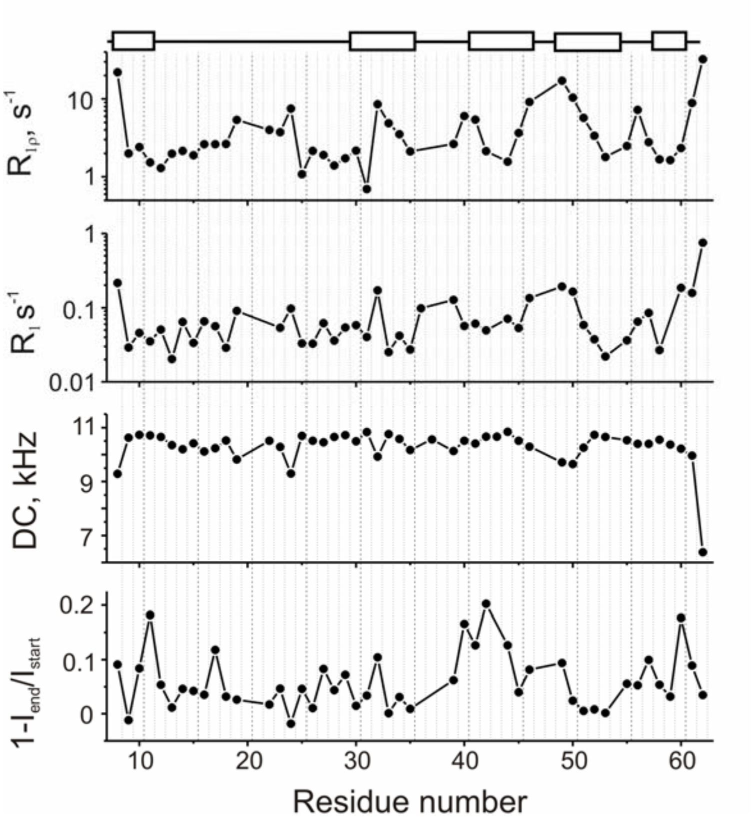

Fig. 28. Dynamic parameters measured in SH3 domain by means of ^{15}N ssNMR spectroscopy. R_1 is the relaxation rate (600 MHz);[127] DC are ^{15}N-^{1}H dipolar couplings reported by Chevelkov *et al*;[126] 1-I_{end}/I_{start} are relative amplitudes of the dipolar CODEX decays.[138] $R_{1\rho}$ relaxation rates (spin-lock frequency 8 kHz, spin-frequency 20 kHz, temperature 10°C, by 400 MHz spectrometer) are taken from Ref. [160]. In the upper part of the figure the secondary protein structure is shown.

Similar features for R_1 and $R_{1\rho}$ dependencies also appear if the protein backbone undergoes motion with a correlation time around $10^{-8} - 10^{-7}$ s. This corresponds to a region that is located between the maximum sensitivity of the R_1 and $R_{1\rho}$ relaxation experiments. To check what the actual cause is, one should quantify the correlation times and order parameters by some model or by using the "model-free" approach. Comprehensive relaxation data analysis will be presented in the last part of the thesis.

Not only do the trends of the relaxation rates appear similar to each other, the motionally averaged dipolar couplings also have related dependencies. Residues possessing increased relaxation rates, namely L8, S19, T24, T32,V46, R49, Q50, L61 and D62, also have lower dipolar couplings, which means a greater extent of averaging by motion.

This observed correspondence is not surprising. Generally, the ends of the backbone (L8, L61 and D62) and some loop regions (V46-Q50) undergo less restricted motions, while the centres of the structured protein elements are stabilized by hydrogen bonds.

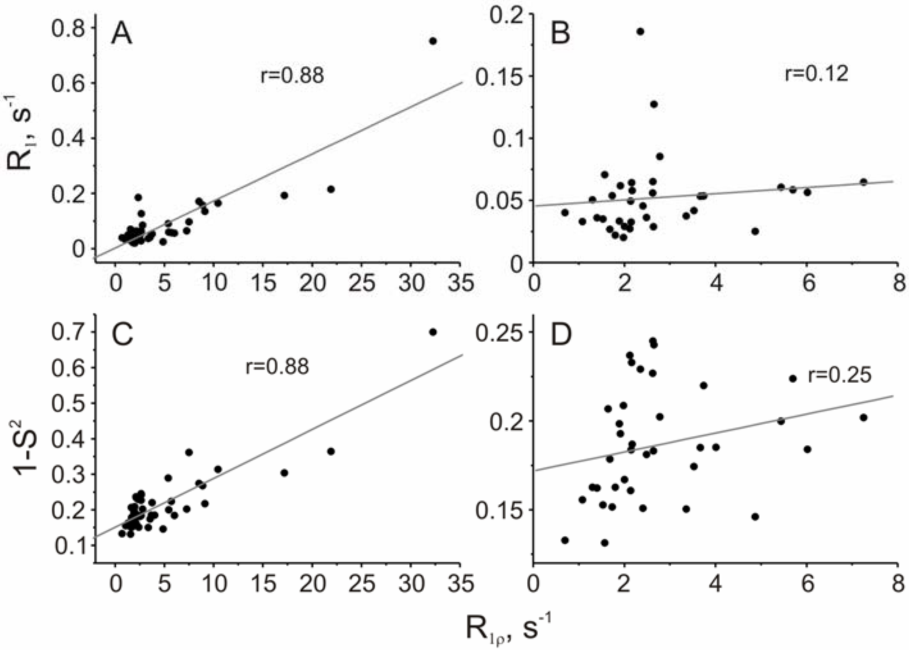

Fig. 29. A, B: R_1-$R_{1\rho}$ correlation maps. In A relaxation rates for all residues are plotted. B is plotted without L8, S19, T24, T32,V 46, R49, Q50, L61 and D62 residues.
C, D: 1-S^2-$R_{1\rho}$ correlation plots. Here 1-S^2 is amplitude of motion derived from motionally averaged dipolar couplings measurements according to the equation $1-S^2 = 1-\left(D_{exp} / D_{rigid}\right)^2$. In the left plot (C) all measured residues are present, in the right one (D) there is no amide atoms possessing increased relaxation rates. The picture is taken from Ref. [160].

To make more precise conclusions concerning correlations of these NMR parameters, the correlation plots are presented in fig. 29. Here, we compare the R_1 data (measured by a 600 MHz NMR spectrometer at 12°C) and $R_{1\rho}$ data (at spin-lock frequency 8 kHz, spin-frequency 20 kHz, temperature 10°C, by 400 MHz spectrometer).

From this figure we see that there is only a correlation between NMR parameters characterising solid-state protein dynamics if the mobile sites are involved. However, if we exclude nine residues possessing high relaxation rates, then only a weak relation between the data persists. To find a real reason for the correlation a more rigorous analysis is required.

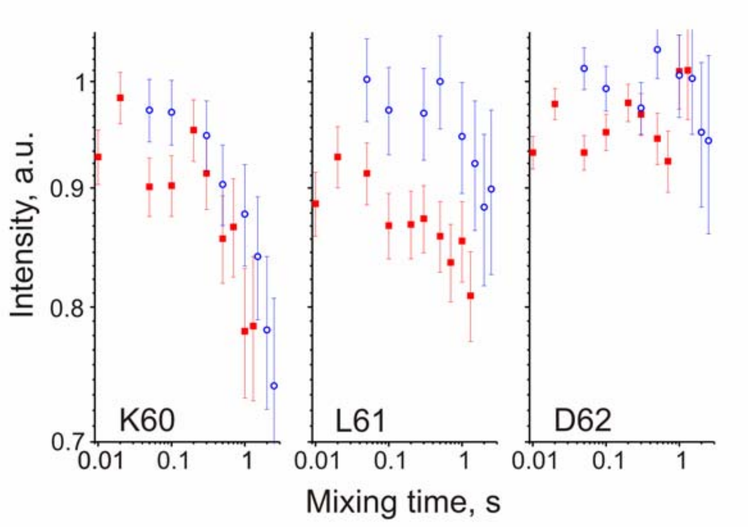

Fig. 30. The exchange decays measured by dipolar CODEX in SH3 domain. Data are published in Ref. [138]

The $1\text{-}I_{end}/I_{start}$ dependence[138] has a different characteristic profile (Fig. 28). This term can serve as a measure of the ultra-slow (millisecond to second) motions. As is clear from the figure, there is millisecond mobility in the SH3 domain, but it does not correlate with microsecond and nanosecond dynamics. Nevertheless, we can use the exchange experiment results to complement the comprehensive picture of the protein dynamics. If we refer to the C-terminus of the backbone and consider $R_{1\rho}$ and dipolar CODEX data (fig. 30), then we will see that the increased mobility in the millisecond-second timescale is intrinsic for the K60 and L61 residues, whereas D62 reveals no motions in this time window. However, in the relaxation experiments characterizing microsecond mobility, D62 demonstrates an elevated relaxation rate. Combining this information we conclude that three terminal residues undergo slow motion. The rate of this motion gradually increases towards the end of the SH3 backbone; thus, D62 residue dynamics occur outside of the sensitivity of the CODEX experiment, at shorter correlation times.

4.3. Conclusions

In the course of this work it was shown that perdeuterated microcrystalline proteins are perfectly suited for investigations of protein dynamics through ssNMR. In such protein samples, it is possible to measure dynamic information with site-specific resolution free from the influence of spin-diffusion. Proton detection helps to achieve good signal-to-noise ratio without time-consuming experiments.

The distribution of relaxation rates evidences different mobility for different parts of protein globules. The ends of the SH3 backbone and some of the unstructured region possess significant dynamics on both nanosecond and microsecond time scales. For other residues located in β-sheets and loops there is no obvious correlation between different types of motions. For ascertaining the inter-relation between protein mobility and functionality, it is necessary to characterize different motions quantitatively. By simultaneously analyzing the data characterising motion on different time scales, we gain better insight into functional protein dynamics.

In summary, we conclude that with a more abundant experimental data set, more detailed information concerning molecular motions is possible. Information for different types of motion from different NMR experiments complements each other and increases our understanding of protein mobility and enlightens mechanisms of enzyme functionality.

5. General R_1/$R_{1\rho}$ equations in the “model-free” analysis of NMR relaxation data in solids

Relaxation rates measurements are a good tool for providing site-resolved dynamic information in proteins. However, relaxation times contain only indirect information about amplitudes (angles) and correlation times of motions. To extract these parameters one must apply some approach to obtain the correlation function for the motion. A single relaxation time cannot provide sufficient information to restore the whole correlation function, requiring multiple relaxation measurements. The temperature or frequency dependence of the relaxation rates proves to be very informative. For example, the number of minima by T_1 temperature dependence indicates the number of dynamic processes which the probe nucleus undergoes. The application of special mathematical formalisms for the temperature dependent relaxation data provides frequencies and angles of motions.[96] There are different models used for the quantification of the NMR relaxation data. For example, widely used in protein dynamic studies is the “diffusion-in-a-cone” model[128,131,132] or the Gaussian axial fluctuation model.[162] An alternative method to treat relaxation data is by a “model-free” approach introduced by Lipari and Szabo,[103,104,135] which, we note, also represents a specific model for data analysis.

No matter which approach one decides to apply for the quantification of the experimental data, it is always necessary to know how relaxation rate depends on the correlation function of motion (or spectral density function). The equations derived before for the relaxation rates rarely take into account the possible resonance frequency off-set, which is very important in suppressing spin-spin contributions, and arbitrary values of the spin-lock pulse frequency and MAS frequency.[93,163] Recently new equations for the relaxation caused by dipolar coupling and CSA accounting for these complications were derived in our group and published in Ref. [92]. In this section, the limits of the applicability of these equations will be validated by means of the SPINEVOLUTION program,[31] which can simulate a simple motional “two-site jumps” model with different frequencies. All simulations along with some conclusions were performed by myself. Some of the results are published in Ref. [92].

5.1. SPINEVOLUTION simulations

SPINEVOLUTION[31] is a general program for the simulation of NMR experiments specifically tailored for solid samples. It works more efficiently than other simulation programs. More important for my purposes, is its ability to imitate the influence of motion on NMR measured parameters. To check the validity of the equations, I performed numerical simulations. The main

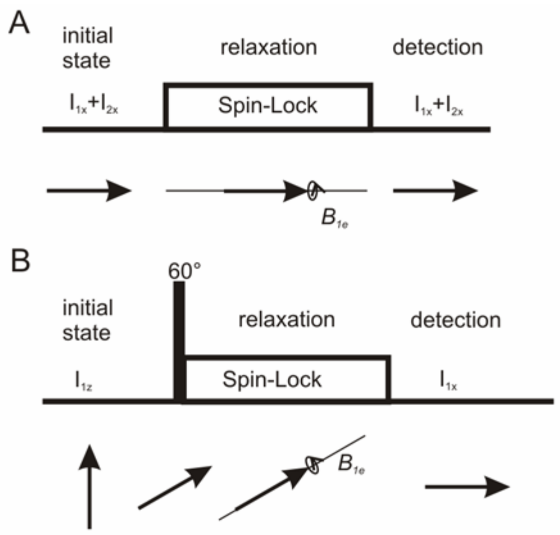

Fig. 31. Representation of $T_{1\rho}$ experiments in on- and off-resonance modes (A and B, respectively). The figure demonstrates the simplified pulse sequence and the initial state of the spins and observables. In plot A two spins participate in the simulation, in plot B just one spin evolves under the CSA interaction during the off-resonance spin-lock field. The arrows depict the magnetization directions.

advantage of the numerical simulations is the possibility to distinguish between both significant relaxation mechanisms (CSA and heteronuclear dipolar coupling) for our samples. This would be impossible in real NMR experiments.

The first important step is to specify the pulse sequence, the spin system of interest and the powder averaging scheme. To direct the program to carry out the correct action, an input file has to be written. The input file consists of four main parts: *System*, *Pulse Sequence*, *Variables* and *Options*. In *Options*, one declares the initial density matrix elements significant for the experiment, observed spins, powder averaging scheme, line broadening (if necessary), and the Fourier-transformation options.

An important issue that I would like to mention is a limitation of the SPINEVOLUTION program in simulating T_1 relaxation process. The program takes into account only secular approximation for the Hamiltonians. It works well in most cases, but for the T_1 relaxation the secular approximation is not enough, while this process is also caused by non-secular terms of the Hamiltonian. Thus, to be on the safe side, one should make sure that the T_1 relaxation contribution is negligible in the simulation procedure. In the case of $T_{1\rho}$ simulations it is strongly important to choose the correlation time of motion in the intermediate limit (approximately 10^{-8} s), where T_1 makes almost no contribution to the relaxation rate (see Appendix 14).

All simulations were performed for the case of the NMR spectrometer operating at the proton frequency 400 MHz with the probe nucleus was ^{15}N. The parameters describing the CSA tensor and its orientations were: δ=100 ppm, $\eta = 0$, and the angle between different orientations (θ) was chosen to be 60° (if not otherwise specified). The dipolar coupling was calculated from the ^{1}H-^{15}N bond length of 1.015 Å.[164] In the case of the dipolar coupling mechanism, the motions were simulated as jumps between two different equally-populated states of the ^{1}H-^{15}N bond orientations (all simulation details are summarized in the Appendix 6).

First, I performed simulations for two cases of β_ρ angles corresponding to an on-resonance spin-lock frequency (β_ρ=90°) and an off-set angle of 60° for two mechanisms of relaxation. The simplified simulated pulse sequences are schematically depicted in fig. 31.

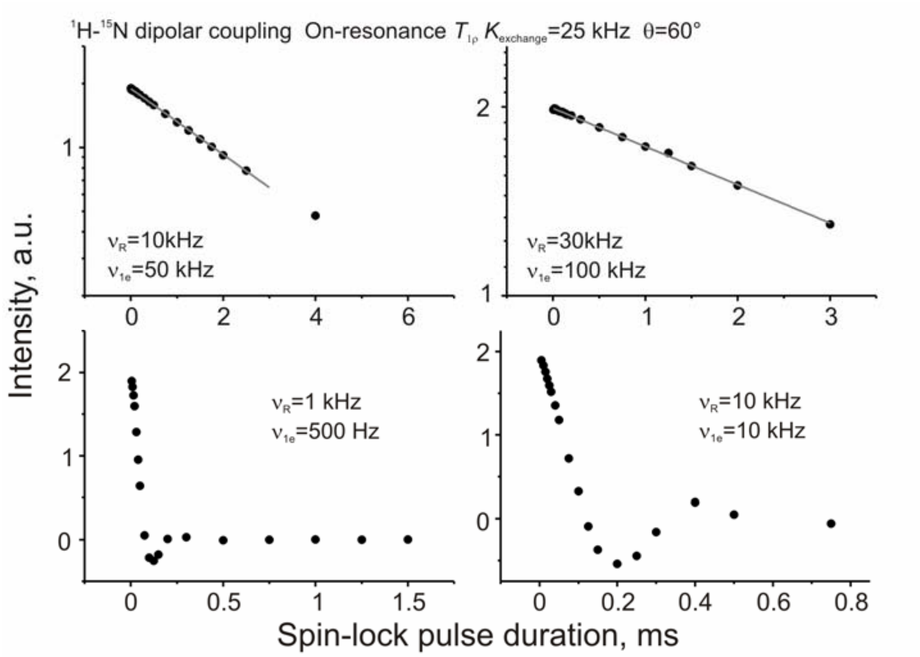

Fig. 32. Examples of the relaxation decays simulated by SPINEVOLUTION program. $K_{exchange}$ is the "two-site jump" rate and θ is the angle between sites. ν_{rot} is the MAS frequency and ν_{1e} is the spin-lock pulse frequency.[92]

The magnetization decays due to CSA and dipolar coupling relaxation were simulated as a function of the spin-lock pulse duration. Its duration varied between 5 μs to the value corresponding to a decay of 90-95% of the initial intensity. In the case of very long spin-lock pulses the simulations can be very time-consuming. Then, I limited myself with 50% decay of the initial intensity. The simulated points were fitted by a single-exponential decay to determine the relaxation rates:

$$I(t) = I(0) \cdot \exp\left(-t \cdot R_{1\rho}\right) \tag{5.1}$$

Examples of decays are depicted in fig. 32. As is shown, the simulated points in the upper figures can be described quite well by a single exponential decay. Strictly speaking, decays will not necessarily appear as a single exponential curve. In a static solid sample there is a distribution of orientations of dipolar coupling vectors with respect to $\vec{B}_0$. As a result there is also a distribution of relaxation time constants corresponding to different dipolar couplings. Thus, the form of the relaxation decay is multi-exponential. To quantify relaxation data, it was suggested to define the mean relaxation rate from the initial slope of the relaxation curve.[94] During magic angle spinning the orientation dependence of the relaxation times reduces, through this the relaxation decay becomes nearly exponential. The mean relaxation rate defined in static and rotating powder samples stays the same. This approach allows comparison of motional studies carried on static and rotating samples.

The deviations from the exponential function were also observed during simulations, at large values of spin-lock pulse timing. These deviations have just a small influence on the value of relaxation rate constants, and explain minor differences in relaxation constants obtained in simulations and defined analytically. The behaviour of the decays in the bottom of the fig. 32 will be discussed later.

For analytical calculations, the form of the spectral density function was assumed to be according to the Lipari-Szabo[103,104] approximation:

$$J(\omega)=\frac{2}{5}\left(1-S^2\right)\frac{\tau_C}{1+\left(\omega\tau_C\right)^2} \tag{5.2}$$

the factor of 2/5 comes from the powder averaging in spectral densities. In the frame of work published by our group[92] the sameness of correlation functions $C_0(t), C_1(t), C_2(t)$ was proven by the computer simulations take into account the powder averaging in isotropic samples. This means that $J_0(\omega), J_1(\omega), J_2(\omega)$ are also the same, similar to the liquid-state case. Thus, one can analyze the isotropic solid sample relaxation data by using a “liquid-state” “model-free” approach. Thus, we can skip the indexes of the spectral density functions in equations (2.39) and (2.40).

$$\begin{aligned}
R_{1\rho}^{IS} &= R_1^{IS}+\sin^2\beta_\rho\left(R_{1\Delta}^{IS}-\frac{1}{2}R_1^{IS}\right)\\
R_1^{IS} &= {\mu_S}^2\left(J\left(\omega_I-\omega_S\right)+3J\left(\omega_I\right)+6J\left(\omega_I+\omega_S\right)\right)\\
R_{1\Delta}^{IS} &= {\mu_S}^2\left(3J\left(\omega_S\right)+\frac{2}{3}\sum_{\substack{n=-2\\ n\neq 0}}^{2}\frac{1}{|n|}J\left(\omega_e+n\omega_R\right)\right)
\end{aligned} \tag{5.3}$$

$$\begin{aligned}
R_{1\rho}^{CSA} &= R_1^{CSA}+\sin^2\beta_\rho\left(R_{1\Delta}^{CSA}-\frac{1}{2}R_1^{CSA}\right)\\
R_1^{CSA} &= \frac{3}{4}\left(\delta\omega_I\right)^2 J\left(\eta,\omega_I\right)\\
R_{1\Delta}^{CSA} &= \frac{1}{6}\left(\delta\omega_I\right)^2\sum_{n=-2,n\neq 0}^{n=2}\frac{1}{|n|}J\left(\eta,\omega_e+n\omega_R\right)
\end{aligned} \tag{5.4}$$

5.1.1. *Equation validity*

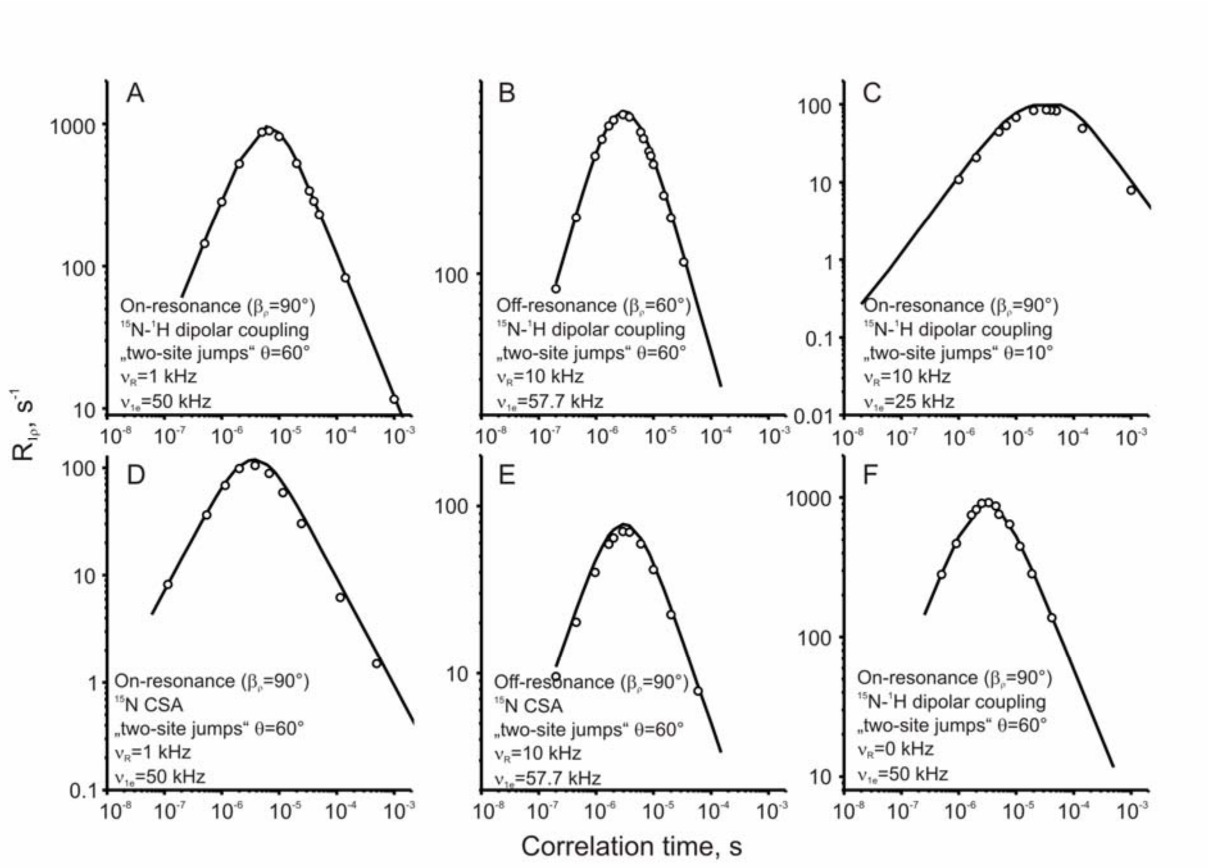

Fig. 33. Relaxation rates as a function of the correlation time of the motion calculated by analytical expressions (open circles) and simulated (solid lines) by the SPINEVOLUTION program.[92]

Results of simulations and analytical calculations with equations (5.3) and (5.4) are presented in Fig. 33. These figures demonstrate good correspondence between analytical and simulated relaxation rates at different conditions.

Since the highest relaxation rates are inherent to the dipolar coupling mechanism (for the B_0=9.36 T) and large angles between two states, I saved time by only simulating the ^{1}H-^{15}N dipolar mechanism of relaxation with a "jump" angle of 60°. The usage of the dipolar coupling mechanism is quite well justified since at low and moderate external fields $\vec{B}_0$ this mechanism is more efficient for relaxation.

5.1.2. *Limits of applicability*

Further simulations were performed to check the limits of applicability for equations (5.3) and (5.4). The relaxation rate dependence on the effective field strength was simulated and compared with the analytical expression. The first problem which appears during simulations is that at the rotary resonance condition (when the nutation frequency matches the sample spinning frequency $\omega_1 \approx n \cdot \omega_R$, n=0, 1), the magnetization decay can not be described by a single-exponential function. The example of this relaxation behavior is presented at the bottom of fig. 32.

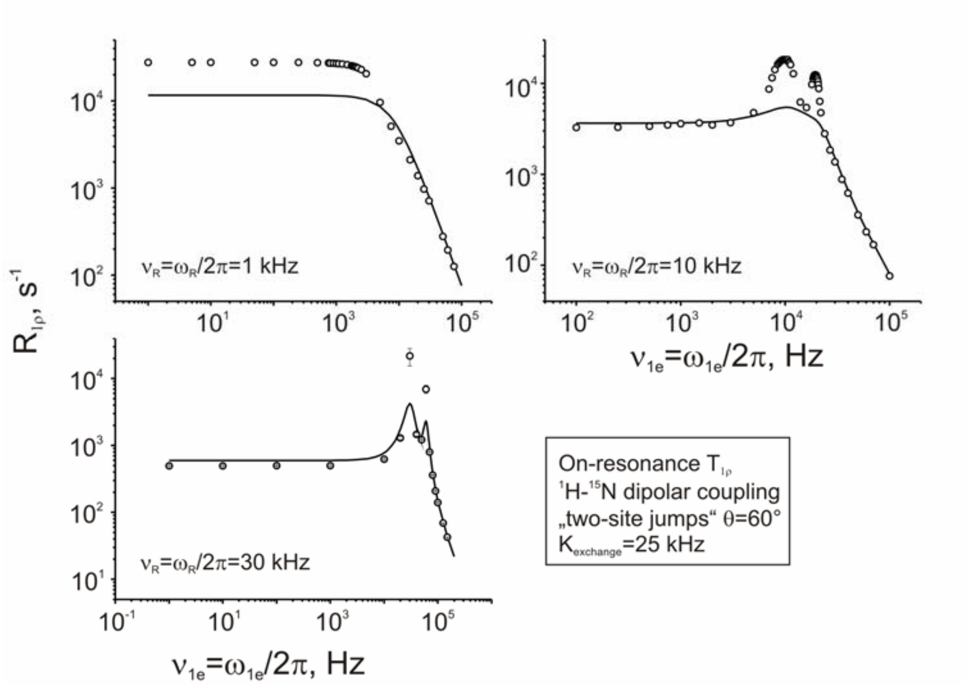

Fig. 34. Spin-lock field frequency dependencies of the relaxation rates at different MAS frequencies. Solid lines are for the analytical $R_{1\rho}$ calculations and opened circles denote the simulation.[92]

As is evident from pictures (fig. 32 and fig. 34), rotary resonance has a large influence on the value of the relaxation rate. However, it does not contain dynamic information. Thus, one should avoid the matching rotary resonance condition in experiments; otherwise the elevated relaxation rates lead to the misinterpretation of the underlying motional behavior. A consequence of this phenomenon is the restriction to measuring motional parameters for very slow dynamics.

5.2. Conclusions

This work confirms the validity of the derived expressions for the relaxation rates in the case of the CSA and dipolar coupling mechanism of relaxation. Moreover, the limiting conditions for these equations were defined. Rotary resonance seems to be the only reason for the incompatibility of the analytical expressions to the simulations. If the nutation frequency differs from the MAS rotation frequency, then these equations determine accurately the relaxation rates. The equations take into account both the magic angle spinning and the off-resonance spin-lock frequency. The latter is highly important in order to increase the effective field strength without damaging power of the transmitter.

The derived expressions can be used to interpret the relaxation rates obtained from the experiments to gain amplitudes and correlation times of motions.

6. Multifrequency quantitative analysis of ^{15}N solid-state relaxation data characterising protein internal dynamics

This part is devoted to the comprehensive analysis of the ^{15}N relaxation data measured on deuterated microcrystalline SH3 domain of chicken α-spectrin. This analysis provides information about internal protein motions occurring on different time scales. The measurement of T_1's and $T_{1\rho}$'s at different conditions (magnetic fields, temperatures, spin-lock fields for on- and off-resonance spin-lock frequency) yields information about motions with correlation times up to microseconds. ^{1}H-^{15}N dipolar couplings averaged by motions are a direct measure of motional amplitudes for all motions faster then several microseconds. Thus, joint analysis for the complete set of all available experimental data covers a dynamic range of 6-7 orders of magnitude in correlation time.

Analysis performed in the current work is based on the "model-free" approach,[103,104] supposing the presence from one up to three independent components of motional process inherent to each residue of the SH3 domain. Starting with the simplest regime-one motional process, I increased the complexity by introducing other motional modes to find a good fit of experimental data with a minimum number of fitting parameters. Assuming a complex nature of motions, which could lead to a distribution of correlation times, I also evaluated a model where motion has a smooth distribution of correlation times. The results of this work will help to better understand the dynamic processes occurring in the model protein on different time scales. I performed all fitting procedures and contributed to most of the conclusions. The results presented in this chapter were obtained by our group and published in Ref. [165].

6.1. Experimental data

In this section, I analyse the solid state NMR data measured in previous experimental studies of SH3 domain. The $T_{1\rho}$ data was measured and discussed already previously in frame of this thesis. Some of the experimental results were published elsewhere; some of them were measured but not published explicitly. Below is the list of the experimental NMR parameters used in the analysis:

- ^{15}N-^{1}H motionally averaged dipolar couplings (order parameters) measured at 400 MHz (^{1}H resonance frequency), MAS rate 20 kHz, t=11 °C[126];
- ^{15}N T_1 at 400 MHz, MAS rate 13 kHz, t=12 °C[127];
- ^{15}N T_1 at 600 MHz, MAS rate 13 kHz, t=12 °C [127];
- ^{15}N T_1 at 900 MHz, MAS rate 13 kHz, t=12 °C[127];

- ^{15}N T_1 at 600 MHz, MAS rate 10 kHz, t=14 °C[138];
- ^{15}N T_1 at 600 MHz, MAS rate 10 kHz, t=24 °C[138];
- ^{15}N $T_{1\rho}$ at 400 MHz, MAS rate 20 kHz, on-resonance spin-lock 8 kHz (^{15}N resonance frequency in the rotating frame), t=10 °C[160];
- ^{15}N $T_{1\rho}$ at 400 MHz, MAS rate 20 kHz, on-resonance spin-lock 13 kHz, t=27 °C[160];
- ^{15}N $T_{1\rho}$ at 400 MHz, MAS rate 20 kHz, on-resonance spin-lock 8 kHz, t=27 °C[160];
- ^{15}N $T_{1\rho}$ at 600 MHz, MAS rate 10 kHz, off-resonance spin-lock 35 kHz (effective ^{15}N resonance frequency in the tilted rotating frame), the off-resonance angle between B_0 and B_{1e} fields 24°, t=14 °C[160];
- ^{15}N $T_{1\rho}$ at 600 MHz, MAS rate 10 kHz, off-resonance spin-lock 35 kHz, off-resonance angle 24°, t=24 °C[160];
- ^{15}N $T_{1\rho}$ at 600 MHz, MAS rate 10 kHz, off-resonance spin-lock 46.3 kHz, off-resonance angle 24°, t=14 °C[160].

In total, I consider up to 11 relaxation rates measured at different conditions in combination with motionally averaged dipolar couplings. It should be noted that for some residues not all listed data was available. The T_1 relaxation decays measured in Ref. [138] were used for the normalization of the dipolar CODEX decays. In the frame of that work, there was no need to measure relaxation delays exceeding the mixing times used in the exchange experiments (longer then 3-4 s). Thus, the relaxation delays were not long enough for the accurate determination of T_1's ~ 20-30 s, and were excluded from the analysis. A similar problem with the off-resonance $T_{1\rho}$ relaxation rate determination was discussed in a previous section (section 4.2.1). The details of the experiments performed by other authors are presented in the corresponding references. All the experimental data used in the fitting for each residue is summarized in the table in Appendix 7.

In the 2D ^{15}N-^{1}H correlation spectrum (see fig. 25) it was possible to register 54 signals from the backbone amides and 8 peaks corresponding to the side chain ^{15}N atoms. Some of the residues are obscured from the spectra due to their increased mobility. Two pairs of residues (K18 and K59, E17 and E22) cannot be resolved from each other at some temperatures because of line overlap. Thus, for these two pairs we are able to define only averaged dynamic parameters. Moreover, SH3 domain backbone includes residues Pro20 and Pro54. These do not bear N-H group and do not appear in ^{15}N-^{1}H correlation spectra.

6.2 Data analysis

The main goal during the processing of relaxation data is to obtain the correlation function of motion for each of the residues in our protein. This can be done in frame of some model. The "model-free" approach allows for a dramatic reduction of the potential parameters, as it neglects specific geometries and subsumes any geometric information in the order parameter.[103,104] Nevertheless, the choice of the number of components of the correlation function is still represents a model. Here, I will discuss the theory underlying our treatment.

In the previous chapter we derived and checked the applicability of the equations (5.3) and (5.4) characterizing relaxation rates in the laboratory and rotating frames caused by CSA and dipolar interactions. As was stated, these formulae account for MAS rotation and the resonance off-set of the spin-lock frequency from the resonance condition. Hence, these equations can be successfully used in our data analysis.

Some assumptions were made in our work:

- The CSA tensor is assumed to be axially symmetric ($\eta = 0$). As a result we have the same expression for all spectral density functions used in equation (5.4).
- The length of the ^{15}N-^{1}H bond is supposed to be 1.015 Å as it was reported in Ref. [164].
- The ^{15}N anisotropy value we take to be 160 ppm.[166–169]
- Moreover, we accepted that the main axis of the ^{15}N CSA tensor is along the ^{1}H-^{15}N bond. Strictly speaking this is not the case. There are some experimental results indicating that the backbone main axis is tilted at 20° with respect to the ^{1}H-^{15}N bond,[166] and for the side chains this angle can even be larger 30°.[170] However, this assumption is justified, because only in some special cases of motions will this significantly affect the analysis.

The relaxation rate measured in the experiments can be expressed as:

$$R_{1,1\rho} = R_{1,1\rho}^{IS} + R_{1,1\rho}^{CSA} \tag{6.1}$$

We perform our analysis within the „model-free" approach where the correlation function of the motion is divided into non-averaged and time-dependent parts (Fig. 35). S^2 is assumed to serve as a dimensionless measure of the motional amplitude.

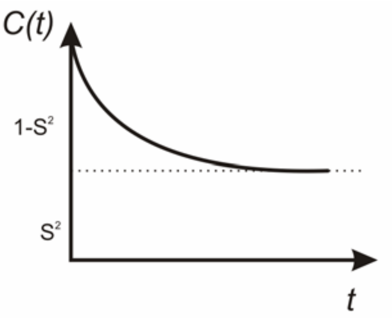

Fig. 35. The description of the time dependence of the motional correlation function in a “model-free” approach.[104]

If the discussed amino acid residue is involved in several motional processes, the correlation function can be expressed as in Eq.(2.49). In the single exponential assumption for the correlation function (and for the spectrometer frequencies larger than zero), the spectral density function is given by Eq. (2.48).

Relaxation rates were measured at different temperatures. Considering the temperature dependence helps determine the trend of $T_{1,1\rho}$ as a function of τ. Thus, the correlation times can be defined more precisely. Despite that the temperature range was narrow, found trend for the activation energies is correct. This means there is a consistent temperature dependence. By taking it into account, we improve the preciseness of the analysis. We suppose the Arrhenius law for the correlation times:

$$\tau(T) = \tau_{293K} \exp\left(E_a / R\left(\frac{1}{T} - \frac{1}{293K} \right) \right) \tag{6.2}$$

here E_a is the activation energy, R is the universal gas constant, and τ_{293K} is the correlation time at 293 K.

In the frame of this analysis, we do not consider the temperature dependence of the order parameters. In fact, there should be a thermal effect on motional amplitudes. However, the analyzed temperature range is not large (12°C – 27°C). The solution state ^{1}H-^{15}N dipolar coupling measurements within this interval showed that the changes in S^2 are just slightly above experimental error.[171,172] Moreover, the solid-state measurements of the motionally averaged ^{1}H-^{15}N dipolar couplings in the lyophilized protein powders show no evident alterations of the order parameters.[156] Of course, it is possible to introduce the temperature dependence, but it will cause the appearance of new fitting parameters and increased uncertainty in the fitting result.

Here, I will summarize the spectral density functions for all the models of motions used in this work. As we start from the a single motion $J(\omega)$ is written as:

$$J(\omega) = \left(1 - S^2\right) \frac{\tau}{1 + (\omega\tau)^2} \tag{6.3}$$

Coming to the more complex form of motion – two components of autocorrelation function – we apply the “extended model-free” approach:[135]

$$J(\omega)=\left(1-S_2^2\right)\frac{\tau_2}{1+\left(\omega\tau_2\right)^2}+S_2^2\left(1-S_1^2\right)\frac{\tau_1}{1+\left(\omega\tau_1\right)^2} \quad (6.4)$$

where subscript "1" denotes slow motion and "2" is used for the fast one.

The most complicated form of the spectral density function implemented in our analysis consists of three components and is written as:

$$J(\omega)=S_3^2\left[\left(1-S_2^2\right)\frac{\tau_2}{1+\left(\omega\tau_2\right)^2}+S_2^2\left(1-S_1^2\right)\frac{\tau_1}{1+\left(\omega\tau_1\right)^2}\right]+\left(1-S_3^2\right)\frac{\tau_3}{1+\left(\omega\tau_3\right)^2} \quad (6.5)$$

providing that $\tau_3 \ll \tau_2 \ll \tau_1$.

If we assume that the $\tau_3 \ll \omega^{-1}$, then the changes in its value do not have a strong influence on the experimentally measured relaxation rate. We take the form of the spectral function to be:

$$J(\omega)=S_3^2\left[\left(1-S_2^2\right)\frac{\tau_2}{1+\left(\omega\tau_2\right)^2}+S_2^2\left(1-S_1^2\right)\frac{\tau_1}{1+\left(\omega\tau_1\right)^2}\right] \quad (6.6)$$

In the case where all components of motions independent from each other, the generalized order parameter is equal to:

$$S_{exp}^2=S_1^2\cdot S_2^2\cdot S_3^2 \quad (6.7)$$

It is important to note that the S_{exp}^2, determined from the experimentally measured dipolar coupling ($S_{exp}^2=\left(D^{exp}/D^{rigid}\right)^2$ where D^{rigid} in the case of ^{1}H-^{15}N dipolar interaction is 11.64 kHz), is a product of all order parameters whose correlation time is shorter than several microseconds.[126] The slower motions do not contribute to the motional averaging of the apparent dipolar couplings.

All above mentioned equations (Eqs. (6.3), (6.4) and (6.6)) consider the loss of the correlation to be exponential. Proteins are very complex systems, and dynamic inhomogenity is very likely for them. Even some relatively simple models of protein dynamics cannot be described by a single-exponential function. Thus, a distribution of correlation times for the spectral density function should be used and checked to see how it influences the results of data analysis. The last model checked corresponds to two motions: one is rather fast and is characterized by only an order parameter, and the second, slower one has a smooth distribution of correlation times according to the Fuoss-Kirkwood function:[106]

$$J(\omega)=S_f^2\left[\left(1-S_s^2\right)\frac{\beta}{\omega}\frac{\left(\omega\tau_s\right)^{\beta}}{1+\left(\omega\tau_s\right)^{2\beta}}\right] \tag{6.8}$$

Here β is a distribution width parameter; its value can be in the range between 0 (infinitely broad distribution) and 1 (no distribution of correlation times). The effect of other values of β on the distribution of correlation times is depicted on fig. 13.

6.3. The fitting strategy

The strategy for the determination of dynamic parameters is in the selection of order parameters, correlation times, activation energies and, sometimes, distribution widths. The proper selection of these parameters will result in the best correspondence of the experimentally measured data to the analytical values calculated with the spectral density functions by Eqs. (5.3) and (5.4). Dynamic parameters were defined from the simultaneous fitting of the experimental data. The fitting procedure included the minimization of the following expression:

$$\chi=\sqrt{\frac{1}{N+1}\left(\sum_{i=1}^{N}\left(\frac{T_{\mathrm{exp}}^{i}-T_{sim}^{i}}{\delta T_{\mathrm{exp}}^{i}}\right)^2+\left(\frac{S_{\mathrm{exp}}^2-S_1^2\cdot S_2^2\cdot S_3^2}{\delta S_{\mathrm{exp}}^2}\right)^2\right)} \tag{6.9}$$

Here T_{exp}^{i} and T_{sim}^{i} are experimental and analytically calculated relaxation times, respectively; δT_{exp}^{i} and δS_{exp}^{2} are the experimental errors in the determination of relaxation rates and dipolar order parameters. A Monte-Carlo algorithm was used to minimize Eq.(6.9). During the procedure 10^6 steps were performed, and mean values of fitting parameters and mean χ values were determined from these trajectories.

One more detail about the fitting procedure should be mentioned. The temperatures at which the relaxation times were measured are in a very narrow range. This fact does not allow a reliable determination of the activation energies of the motions. Sometimes the values were unreasonably high and sometimes too low. Nevertheless, the changes in activation energy do not crucially influence other fitting parameters, only the fitting error. To minimize the possible misinterpretation of the activation energies, the following procedure was carried out. First, all the experimental data was fitted to the analytical curves without restrictions on activation energies. Then unphysical values of E_a (out of the range 10-100 kJ/mol) were excluded, and the mean value of the activation energy and RMSD were found for other values of E_a. The table of the activation energy limits during the Monte-Carlo simulations for each fitting model is shown in the Table 2.

Then, the fitting was repeated considering values of E_a within a range limited by RMSD from the mean value. Another imposed restriction was that the activation energy of the slower motions cannot be less than that of the faster motions. These limitations have a minor impact on the values of correlation times and order parameters.

Table 2. Activation energies for every motional regime used during the Monte-Carlo simulations.[165]

Fitting model	Activation energy limitations, kJ/mol	
One motion	24±12	
Two motions with distribution	32±19	
Two motions	Fast	24±15
	Slow	31±21
Three motions	Intermediate	39±23
	Slow	42±22

6.4. The Akaike Information Criterion (AIC)

The aim of this work is to find the set of motional parameters which describes the experimental data with the best quality. It is evident, that the more complicated the model is, the better the fitting of the analytical curves. On the other hand, the usage of an unreasonably complicated model can lead to overinterpretation of the experimental results. Thus, it is important to find a compromise between the number of fitting parameters and the fitting quality. There are some criteria one can be guided by. In this work, I used Akaike information criterion.[173] This criterion is a measure of the relative goodness of models for a given number of experimental parameters (N). It accounts not only for the fitting error, but also the number of experimental and fitted points:

$$AIC = \ln(\chi^2) + 2K / N \qquad (6.10)$$

Here K is a number of fitting parameters. The model providing the minimum AIC value is assumed to be the best one.

6.5. Results and discussions

6.5.1. *Results of combined data analysis*

The first step is to define the number of the minimal motional processes which is sufficient for good fitting of the experimental results. It is well-known that proteins possess a complex hierarchy of motions in an extremely wide frequency range. Thus, it is clear, that the existence of only one motional process is unlikely. From another point of view, assuming too complicated a motional model can misrepresent dynamic parameters. Accordingly, the primary aim of the investigation was to find a compromise between the fitting quality and model complexity. We started from the simplest model and then sequentially increased the number of motional regimes. The errors and order parameters which were obtained as a result of the fitting procedure, along with experimentally measured dipolar couplings, are depicted in Fig. 36. Initially, all experimental data for all of the residues as fitted to a "one motion" model characterized by a single correlation time, activation energy and an order parameter. In this case the spectral density function has a from of Eq. (6.3). From Fig. 36 it is evident that fitting according to this model gives the highest value of χ among all other models (except for seven residues). Moreover, the inconsistency between experimentally measured order parameters and simulated ones is apparent. This is an evidence of the fact that this model is oversimplified and does not possess physical meaning. The experimental order parameter can be achieved in the frame of the "one motion" model for just one particular residue –Q50. Thus, this is the sole residue which can be described by one motional mode.

The results of fitting with the "one motion" model are presented in Fig. 37. Correlation time of the motions was generally found to be on the timescale of 10-20 ns. In contrast, in another protein investigated by Schanda *et al,*[132] the correlation times according to the "one motion" model were registered to be on the faster, picosecond timescale. The discrepancy can be explained by the $T_{1\rho}$ data inclusion into our analysis. This is also confirmed by Emsley and his group. In their works,[131,133] they considered both T_1 and $T_{1\rho}$ relaxation rates. The correlation times of motions were found to be around 5-20 ns. $T_{1\rho}$ is sensitive to slower motions. By including them, the correlation times shift to slower values. This significantly expands the robustness and the frequency range of the analysis. All this clearly indicates that analysing a limited set of experimental data using a simplified model may provide good fitting quality but physically meaningless results. Because of the poor fitting quality for the "one motion" model, it will be used here as a starting point.

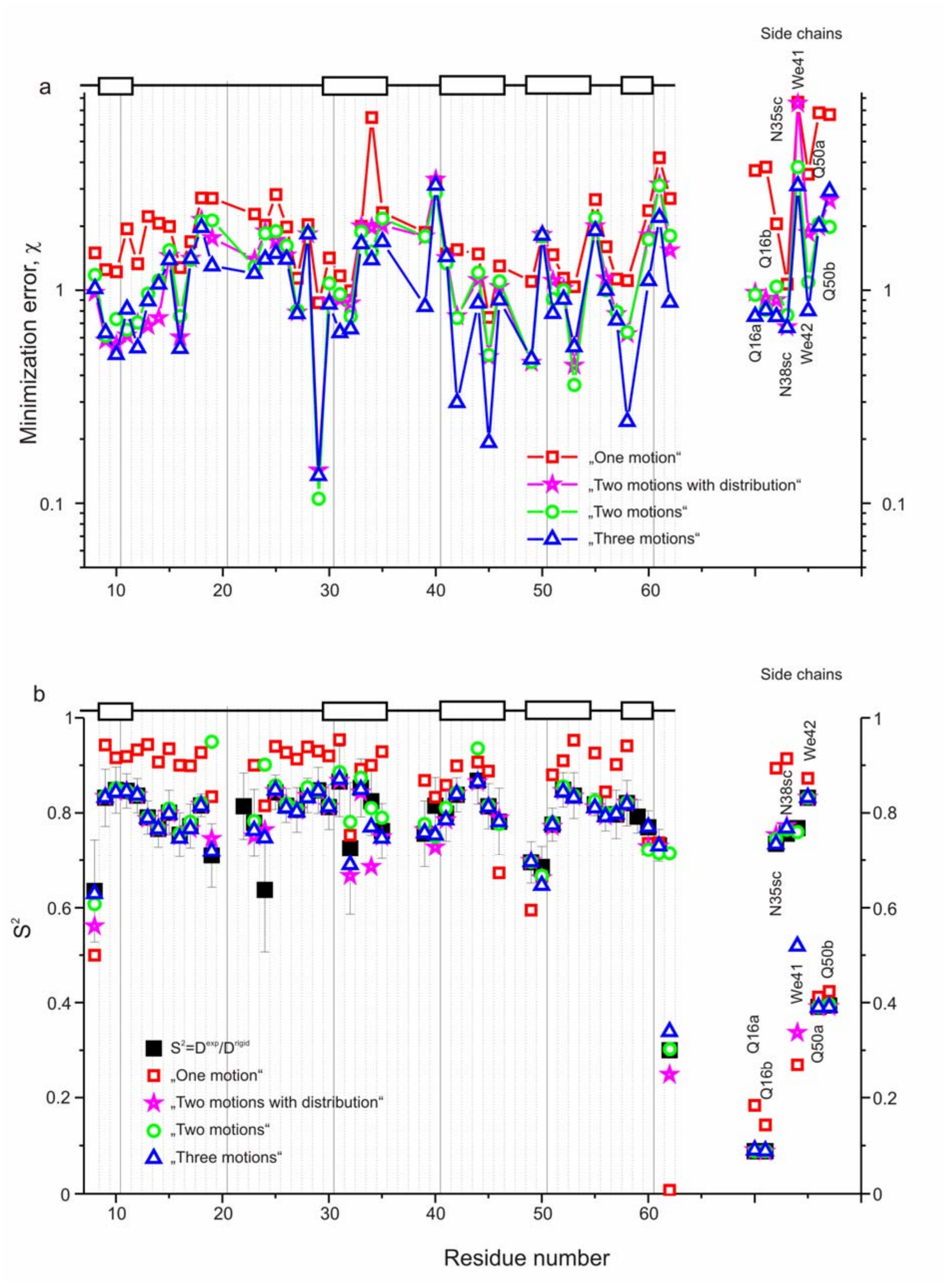

Fig. 36. (a) The deviations of simulated parameters from experimental ones χ (Eq. (6.9)) and (b) dipolar experimental and calculated order parameters as a function of residue number for different fitting models. The side chain residues are depicted on the right side of the figure. In the upper part of figures, the secondary structure of the SH3 domain is represented.[165]

The next used model is “two motions”. It is described by two motional components with distinct correlation times, activation energies and order parameters. In total, there are 6 fitting parameters in the model. The spectral density function is as the form of Eq. (6.4). The first feature to note is a significant improvement of the fitting quality reflected in the decrease of χ upon an introduction of a second component for the correlation function of motion. An analogous conclusion was made by Schanda *et al.*[132]

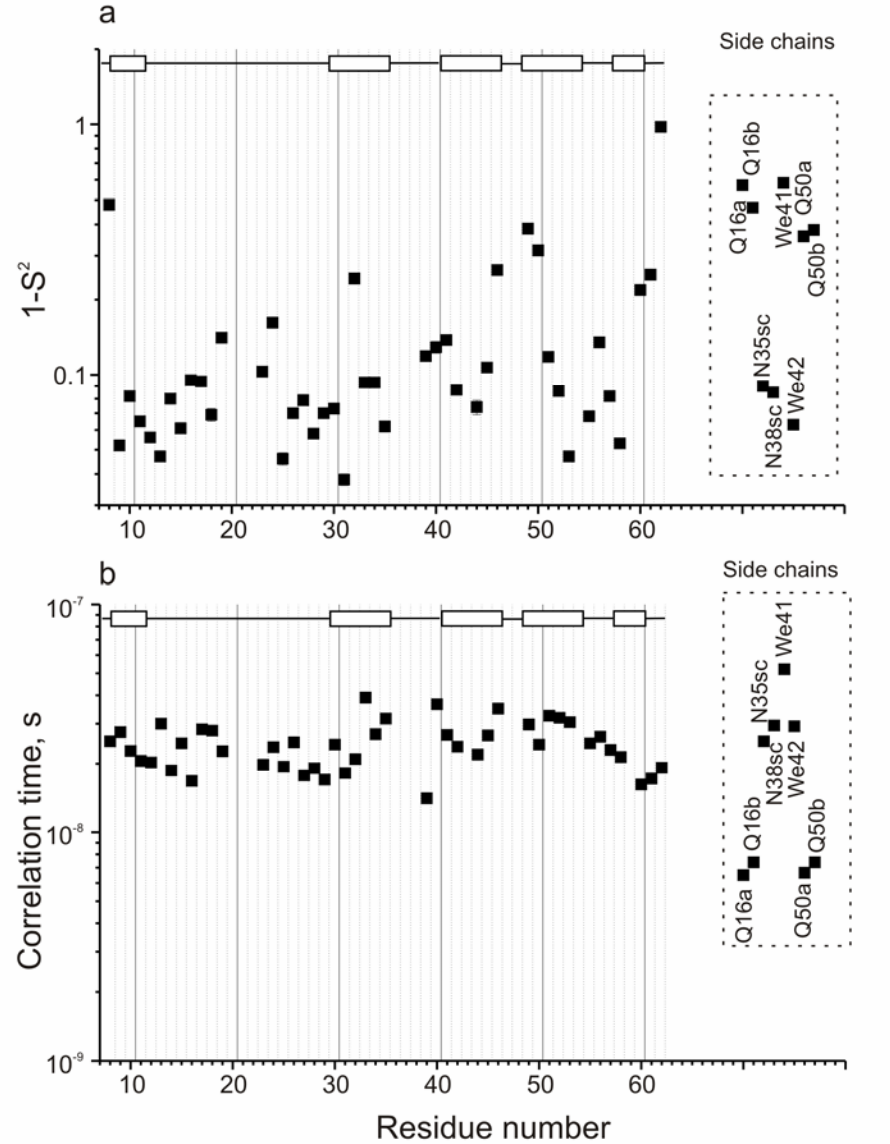

Fig. 37. The amplitude (a) and the correlation time (b) as a function of residue number for the "one motion" model. In the upper part of figures, the secondary structure of the SH3 domain is represented.[165]

Two additionally more complicated models described by the spectral density functions of the form of Eqs. (6.6) and (6.8) were checked during the work. The former represents a “three motions” model, and is described by seven fitting parameters: order parameters, correlation times and activation energies of the slow and intermediate motions and the order parameter for the fast motion. Generally, three motions should be parameterized by nine arguments: three order parameters, three correlation times and three activation energies. However, if the fast motion is assumed to have a correlation time $\tau_f \ll 10^{-11}$ s, then the fitting procedure cannot provide exact values of correlation times and activation energies. Thus, the number of fitting parameters was reduced to seven. Introducing the third motional mode improves the fitting quality for some residues (see Fig. 36 and Fig. 38).

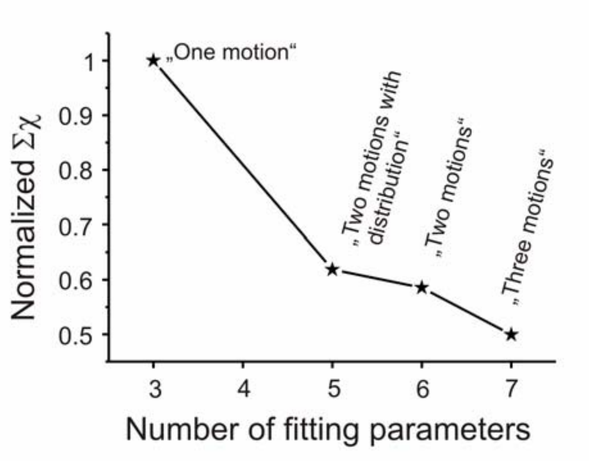

Fig. 38. Summed χ over all residues for the different fitting models.[165]

The latter model ("two motions with distribution") contains 5 fitting parameters: the fast motion order parameter, and the order parameter, correlation time, activation energy and the distribution width of correlation times for the slower motional mode. The introduction of a distribution of the correlation times of slow motion is well-justified for such complex systems as proteins. Slow dynamics are controlled by many cooperative motions. Only through these cooperative motions can the large energy barriers be overcome. The correlation function for such type of dynamics can be very complicated. The spectral density function in this case is as in Eq.(6.8). The fitting quality for "two motions" and "two motions with distribution" is similar (Figs. 36, 38).

The values of AIC which were used to select the most appropriate model of motion inherent for particular residue are presented in table 3. It is worth noting that one should not overestimate the meaning of the model selection based on AIC. This selection is quite ambiguous due to the experimental noise. That is, the minimal values of AIC for some residues point to the "one motion" model as optimal. It does not mean that these residues in fact undergo only one motional mode. It can also mean that the data noise for these residues does not unambiguously define a more complicated form of the motional correlation function. According to AIC, for some residues, three components of the correlation function are needed. Thus, the expansion of the experimental dataset can assist in describing a larger number of motional modes.[129,131–133]

Table 3. χ's and *AIC* values for four fitting models. “1” is “one motion”, “2a” corresponds to “two motions with distribution”, “2” and “3” define, “two motions” and “three motions” models, respectively. RL is the amino acid residue label, NP is the number of experimental data (relaxation times and dipolar order parameter). Lavender and light-pink colours define the minimal *AIC* values among all four models and among three discrete models, respectively.[165]

RL	NP	χ1	*AIC*1	χ2a	*AIC*2a	χ2	*AIC*2	χ3	*AIC*3
L8	11	1.5	1.35638	0.975	0.85846	1.18	1.42194	1.02	1.31233
V9	9	1.25	1.11295	0.583	0.03197	0.612	0.35129	0.631	0.63466
L10	8	1.22	1.1477	0.557	0.07962	0.733	0.87878	0.5	0.36371
A11	7	1.94	2.18252	0.615	0.45631	0.653	0.86193	0.816	1.59332
L12	7	1.33	1.4275	0.701	0.71808	0.706	1.01801	0.538	0.76021
Y13	11	2.22	2.14047	0.682	0.14364	0.963	1.01551	0.893	1.04639
D14	9	2.06	2.11208	0.743	0.51699	1.11	1.54205	1.07	1.69087
Y15	9	1.99	2.04294	1.45	1.85424	1.54	2.1969	1.39	2.21416
Q16	11	1.28	1.03917	0.604	-0.09927	0.758	0.53677	0.534	0.01801
E17	9	1.69	1.71612	1.41	1.79829	1.39	1.99194	1.41	2.24273
K18	10	2.72	2.60126	2.14	2.52161	2.11	2.69338	1.97	2.75607
S19	12	2.71	2.4939	1.76	1.96396	2.13	2.51224	1.3	1.6914
V23	8	2.28	2.39835	1.4	1.92294	1.29	2.00928	1.2	2.11464
T24	11	2.02	1.95165	1.89	2.18224	1.85	2.32128	1.4	1.94567
M25	9	2.82	2.74014	1.71	2.1841	1.89	2.60649	1.49	2.35311
K26	9	1.98	2.03286	1.46	1.86798	1.62	2.29819	1.4	2.2285
K27	9	1.14	0.92872	0.789	0.63713	0.804	0.89702	0.776	1.04835
G28	11	2.03	1.96153	1.83	2.11772	1.86	2.33206	1.84	2.49226
D29	9	0.874	0.39732	0.143	-2.77871	0.105	-3.17426	0.135	-2.44941
I30	8	1.42	1.45131	0.889	1.01468	1.08	1.65392	0.862	1.453
L31	8	1.17	1.06401	0.908	1.05698	0.958	1.41418	0.633	0.83543
T32	9	0.994	0.65463	0.869	0.83029	0.756	0.77391	0.659	0.72149
L33	11	2	1.93175	2	2.29539	1.88	2.35345	1.65	2.27428
L34	8	6.48	4.48744	1.97	2.60607	1.52	2.33742	1.39	2.40861
N35	11	2.32	2.22859	2.015	2.31033	2.17	2.64036	1.69	2.32218
K39	8	1.87	2.00188	1.79	2.41443	1.79	2.66443	0.841	1.40367
D40	9	3.24	3.01781	3.32	3.51104	2.86	3.43498	3.12	3.83122
W41	9	1.48	1.45075	1.42	1.81242	1.34	1.91867	1.44	2.28484
W42	7	1.55	1.73365	0.758	0.87443	0.743	1.12017	0.298	-0.42132
V44	7	1.48	1.64123	1.12	1.65523	1.21	2.09553	0.871	1.72377
E45	8	0.747	0.16662	0.487	-0.18898	0.497	0.10167	0.193	-1.54013
V46	9	1.3	1.1914	1.04	1.18955	1.1	1.52395	0.9	1.34483
R49	7	1.1	1.04776	0.459	-0.12884	0.462	0.1699	0.477	0.51952
Q50	12	1.79	1.66443	1.82	2.03101	1.79	2.16443	1.81	2.35332
G51	11	1.47	1.31598	1.11	1.11781	0.91	0.90229	0.78	0.7758
F52	10	1.14	0.86206	1.02	1.03961	1	1.2	0.908	1.20698
V53	8	1.04	0.82844	0.445	-0.36936	0.36	-0.5433	0.544	0.53239
A55	10	2.67	2.56416	2	2.38629	2.19	2.7678	1.9	2.68371
A56	7	1.6	1.79715	1.14	1.69063	1	1.71429	1	2
Y57	7	1.13	1.10158	0.774	0.9162	0.793	1.25042	0.726	1.35959
V58	8	1.11	0.95872	0.625	0.30999	0.637	0.59803	0.243	-1.07939
K60	8	2.37	2.47578	1.81	2.43665	1.73	2.59624	1.11	1.95872

L61	12	4.2	3.37017	3.15	3.12814	3.11	3.26925	2.2	2.74358
D62	12	2.7	2.4865	1.54	1.6969	1.8	2.17557	0.88	0.911
Side chains									
Q16a	9	3.66	3.26159	0.975	1.06048	0.954	1.23915	0.755	0.99348
Q16b	9	3.8	3.33667	0.915	0.93345	0.812	0.91682	0.808	1.12917
N35	9	2.05	2.10235	0.9	0.90039	1.04	1.41177	0.752	0.98552
N38	8	1.07	0.88532	0.673	0.45798	0.765	0.96424	0.669	0.94606
W41	12	7.66	4.57202	7.55	4.87643	3.8	3.67	3.1	3.42947
W42	6	3.51	3.51123	1.86	2.90782	1.09	2.17236	0.801	1.88954
Q50a	11	6.82	4.38517	1.98	2.27528	2.05	2.52659	2	2.65902
Q50b	12	6.7	4.30422	2.65	2.78245	1.98	2.36619	2.92	3.30983

Though, as it is seen from the table, “two motions with distribution” is beneficial for some residues, to make the representation of data unified and clear, I will discuss only discrete models. In this case, the comparison of dynamic parameters obtained for different residues will be simple and direct. All dynamic parameters for each model are presented in the Appendix. The best fitting results within the AIC are shown in Fig. 39.

6.5.2. *Motional amplitudes vs. correlation times and low- amplitude motions*

The main feature of Fig. 39 is that all motions occurring in the protein can be divided into three groups: fast with correlation times $\tau_f < 10^{-10}$ s, intermediate $1 \cdot 10^{-9} < \tau_i < 2 \cdot 10^{-7}$ s, and slow $\tau_s > 2 \cdot 10^{-7}$ s. These timescale divisions reflect the differing nature of the motions. Secondly, it was found that the slower the motion, the less amplitude it has. However, the decrease in the motional amplitude for different time ranges is not monotonic. To make this conclusion more evident, a histogram of the sum of motional amplitudes vs. correlation times of mobility is presented in Fig. 40. Two peaks corresponding to the increased mobility on fast and intermediate timescales have approximately equal intensities and are separated by a gap of one order of magnitude. Such a gap has not been noticed before, however, can be explained by the difference in the nature of the motion. The fast motions are local oscillations of the N—H vector within steric hindrances. Slower motions requiring correlated rearrangements involve several conformational degrees of freedom. The second and less pronounced gap occurs around 10^{-7} s, and the sharp increase of the motional amplitudes follows.

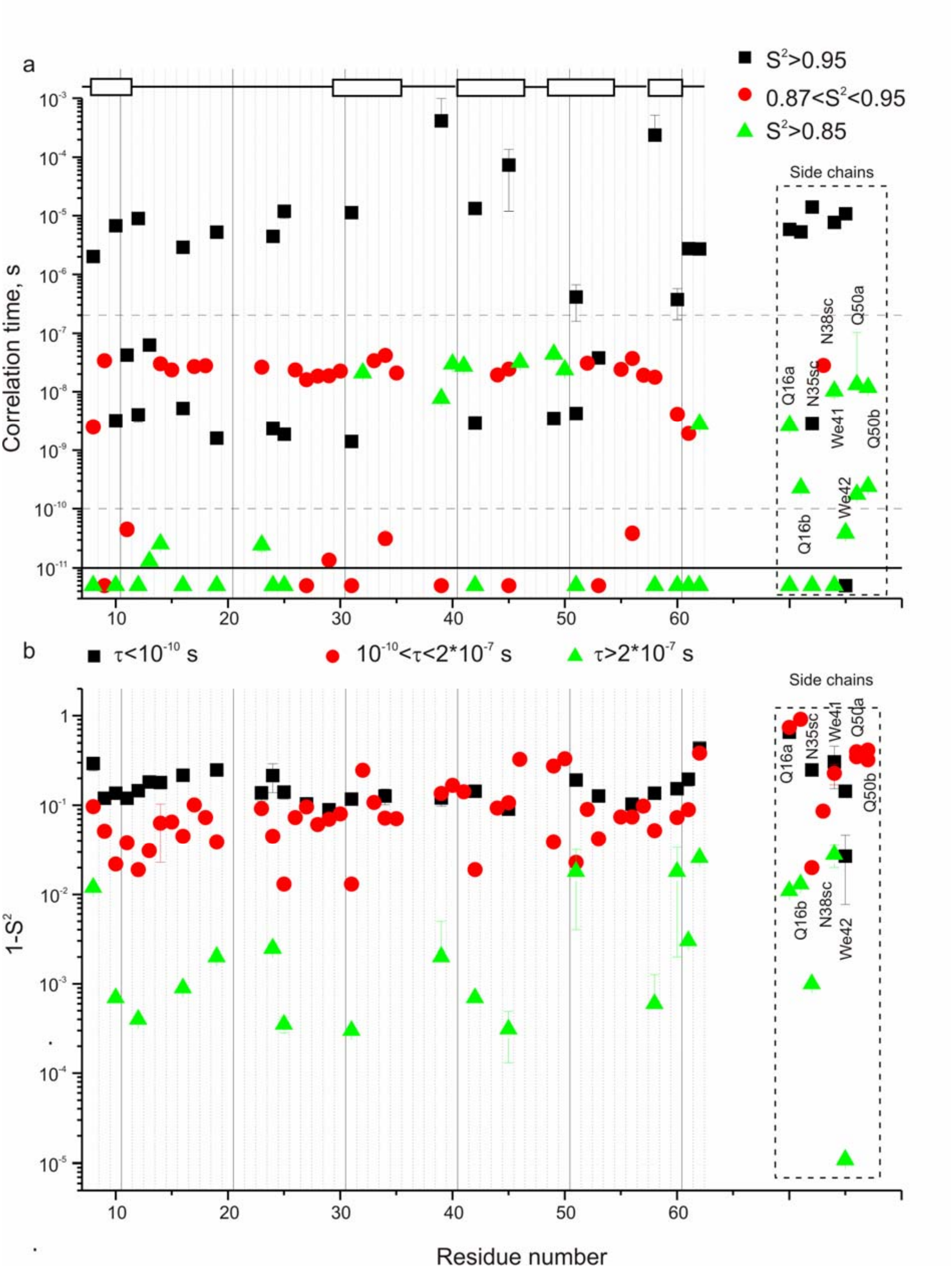

Fig. 39. (a) Correlation times (with order parameter encoded by colours) and (b) motional amplitudes (with correlation time encoded by colours) as a function of residue number. The selection of the model was performned according to the Akaike criterion. The solid line in (a) depicts the limit of correlation times below which the correlation times cannot be defined reliably. Dashed lines separates the fast, intermediate and slow motions.[165]

Such a distribution of motional amplitudes was found to be model independent. The same histograms plotted for three other models possess the same features – a gap between fast and intermediate motions and a sharp decrease of the motional amplitudes around 10^{-6}—10^{-7} s (see Appendix 11-13).

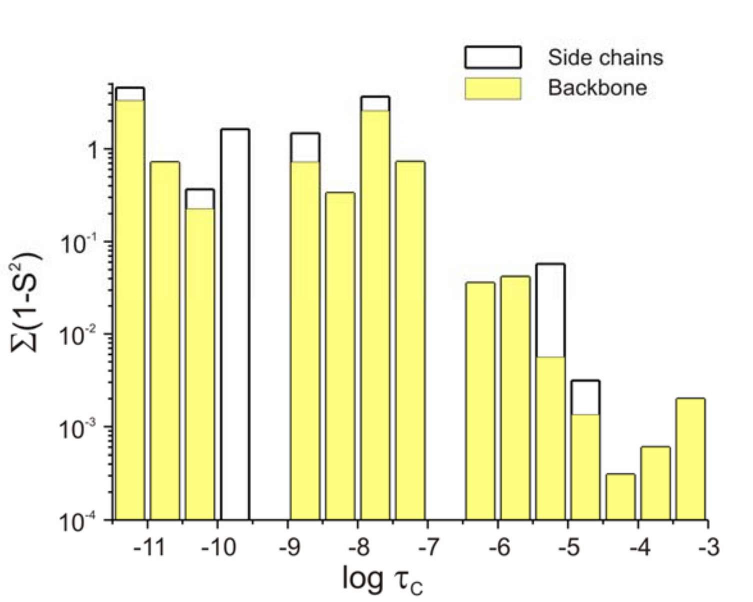

Fig. 40. Histogram of motional amplitudes (1-S^2) summarized for all the residues as a function of the time scale of motion. The fitting models were selected on the base of the *AIC* values.[165]

The detection of slow motions in the microsecond timescale is another important result of the current study. Low amplitudes of slow motions (in sub-percent range) might seem suspicious. However, it is a real result. The inclusion of the $R_{1\rho}$ data in our analysis allows us to determine slow amplitudes. To prove this, I present fig. 41. In this figure the comparison of the fitting quality of the experimental data for two cases is shown. The left figure presents calculated curves with the order parameter of microsecond motion equal to 0.9991, and the right curves calculated with $S_s^2 = 1$, exactly. The figure demonstrates that, only faster motion fails to describe the $T_{1\rho}$ data. Only inclusion of the slower motional mode can provide good fitting quality. Indeed, if the frequency (Eq.(6.3)) is smaller than the inverted correlation time (i.e., $\omega\tau \ll 1$, fast motion limit), then $J(\omega) \approx (1-S^2)\tau$. This means that even when the amplitude $1-S^2$ is low, the product $(1-S^2)\tau$ may still be significant if only τ is long enough. This condition is easily fulfilled for low-frequency spin locks and motions in the μs range.Thus, this picture can serve as evidence for the benefit in considering $T_{1\rho}$ data in the combined analysis.

As it was already stated in the first chapter of this thesis, the S^2 values of motions close to 1 do not necessarily indicate low amplitudes of motions. Conversely, slow motions by their nature should occur with high amplitudes.[5] However, the populations of distinct sites (so called ground and excited states) can be very different – the observed $1-S^2$ varies within the (sub)percent range (Fig. 12). In spite of the great influence of experimental noise, it is possible to unambiguously conclude on the existence of motions on the microsecond timescale. Such slow conformational motions between ground and excited states can be also detected by the liquid-state chemical-exchange method, which can also provide information concerning chemical shifts of the excited state.[111] However, the liquid-state exchange-methods, based on the $R_{1\rho}$ and R_2 relaxation time dispersion measurements, are limited by the population of the excited state – it should be at least 1 percent. Thus, the method implemented in this work is more sensitive to the slow infrequent protein motions.

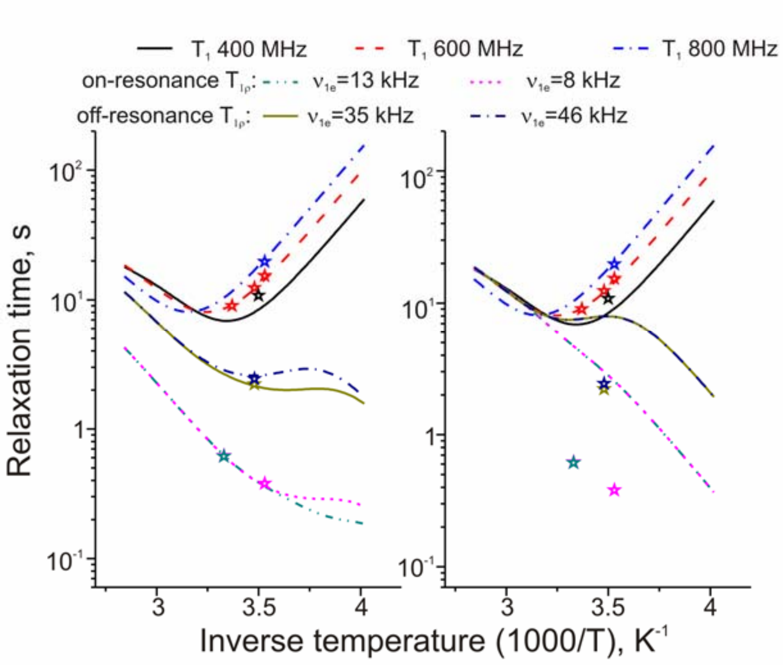

Fig. 41. Experimental (stars) and simulated (lines) $R_{1,1\rho}$ for the Q16 residue. The curves were simulated with parameters: S_f^2=0.78; $\tau_f<10^{-11}$ s; S_i^2=0.956; $\tau_i=5.1\cdot10^{-9}$ s; $\tau_s=2.9\cdot10^{-6}$ s. S_s^2=0.9991 (left) and S_s^2=1.0 (right).[165]

6.5.3. *Alternative minimization protocol*

Here, I would like to make a brief digression on a problem related to the minimization process and calculation of Akaike information criterion. The first question is how to take into account the experimental error in our analysis. All experimental parameters were measured with different accuracy. The accuracy is the best for the experimental order parameters. The first version of fitting relied on the linear scale of relaxation time and accounting for their error. In this case, order parameters possessing small experimental order have the greatest impact on the minimization procedure, while relaxation times have lower priority. The usage of the logarithmic scale has its own advantages. Using a logarithmic scale, the program almost equally fits all the relaxation data, and the weight of the relaxation rates with 10% of error and 20% of experimental error do not differ twice. So, this version should be also considered.

In the case of accounting for the logarithmic scale the minimization equation takes the form of:

$$\chi = \sqrt{\frac{1}{N+1}\left(\left(\sum_{i=1}^{N}\left(\lg T_{exp}^{i} - \lg T_{sim}^{i}\right)^{2} \cdot \left(1 - \frac{\Delta T_{exp}^{i}}{T_{exp}^{i}}\right)^{2}\right) + \left(S_{exp}^{2} - S_{1}^{2} \cdot S_{2}^{2} \cdot S_{3}^{2}\right)^{2} \cdot \left(1 - \Delta S_{exp}^{2}\right)\right)} \quad (6.11)$$

Strictly speaking we cannot use χ as an error parameter for the calculations of AIC. In the original expression it uses the root mean square deviation (RMSD), which is defined as:

$$RMSD = \sqrt{\frac{1}{2N}\left(\sum_{i=1}^{N}\left(T_{exp}^{i} - T_{sim}^{i}\right)^{2} + \left(S_{exp}^{2} - S_{1}^{2} \cdot S_{2}^{2} \cdot S_{3}^{2}\right)^{2}\right)} \quad (6.12)$$

Then Akaike information criterion is expressed by:

$$AIC = \ln(RMSD^{2}) + 2K / N \quad (6.13)$$

where K is the number of the fitting parameters and N is the number of experimental parameters (relaxation times and dipolar order parameters in the current case) for each residue.

To check how these details influence the results of analysis, the fitting procedure was repeated again from the very beginning. First, all residues were fitted to analytical curves corresponding to four different models in order to determine the new activation energy limits (see appendix 15). Then, all residues were fitted again with activation energies within these limits. All parameters were defined from the trajectories in the same way as was described in the section 6.3. In addition to the χ value, the RMSD value was defined for each model and each residue. Figure 42a represents values defined from the minimization equation as a function of the amino acid residue number. As it is clear from the picture, the “one motion” model still provides the worst quality in describing experimental parameters. However, to find the proper model for data interpretation, it is necessary to define AIC’s values. This was done with two expressions (Eq. (6.10) and Eq. (6.13)). It turned out that both versions point to the same model for each residue to be the best. Thus, there is no difference in which expression to apply in this case (AIC’s for RMSD along with RMSD found for the minimization equation (6.11) are presented in Appendix 16).

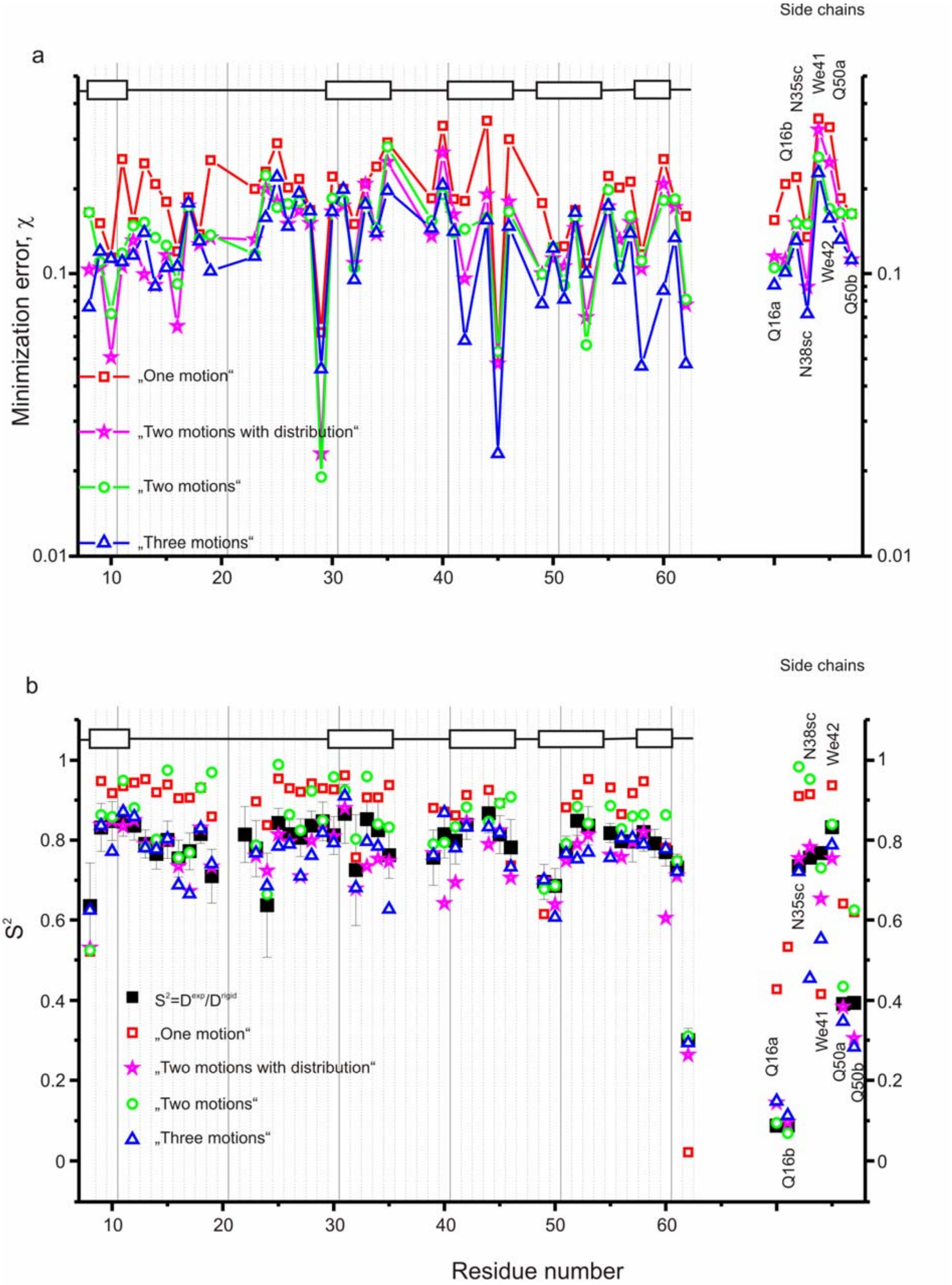

Fig. 42. χ (Eq. (6.11)) and order parameters as a function of the proteins secondary structure for different fitting models.[165]

From the AIC table it is clear that despite the fact that for some particular residues another motional model is beneficial, the overall picture did not change much. Again, “one motion” is not enough to describe properly the dynamic picture of the residue. There are still residues undergoing motional process which is best described by three components of the correlation function.

However, if we refer to the order parameters (Fig. 42b) defined from the new fitting procedure, than we see significant discrepancy between experimentally measured and calculated values, while in the previous version only the “one motion” model failed to describe motionally averaged dipolar couplings. That is not very surprising. Now, we treat all experimental parameters in almost the same way, and order parameters do not have any priority over relaxation rates as it was in the previous calculations. From the mathematical point of view this is reasonable, but by nature experimentally measured order parameters provide direct information on amplitude of all motions intrinsic to the residue. Relaxation rate is only an indirect indication of dynamics. So, from the physical viewpoint the first analysis is more rational.

Nonetheless, all dependencies and pictures were plotted for this version of the fitting procedure and the results are summarized in the Appendix (17-25). All these figures indicate that there is no major differences between the main results of both fitting procedures. In fact, we were able to capture very slow motions despite their low amplitudes. Peaks of the backbone mobility are occurred in the very fast regime and near the 10^{-8} s range of correlation times. Thus, I will only further discuss the first as it seems to be more justified.

6.5.4. *Dynamics on different timescales*

As was found in chapter 4, there is a correlation between the NMR parameters describing the mobility in different timescales (fig. 29). A similar observation was also made by other authors.[53,131] One possibility to explain this correlation is that motions on the nanosecond and microsecond timescales are correlated, and that the nanosecond facilitates the microsecond mobility.[5,174] The data obtained as a result of the simultaneous fitting of experimental data can check whether or not this is a case. Correlation between various dynamic parameters characterizing molecular mobility in different time ranges was not revealed. There was no correlation between any pair of order parameters or correlation times. Thus, the hypothesis was not supported by the results of the current work.

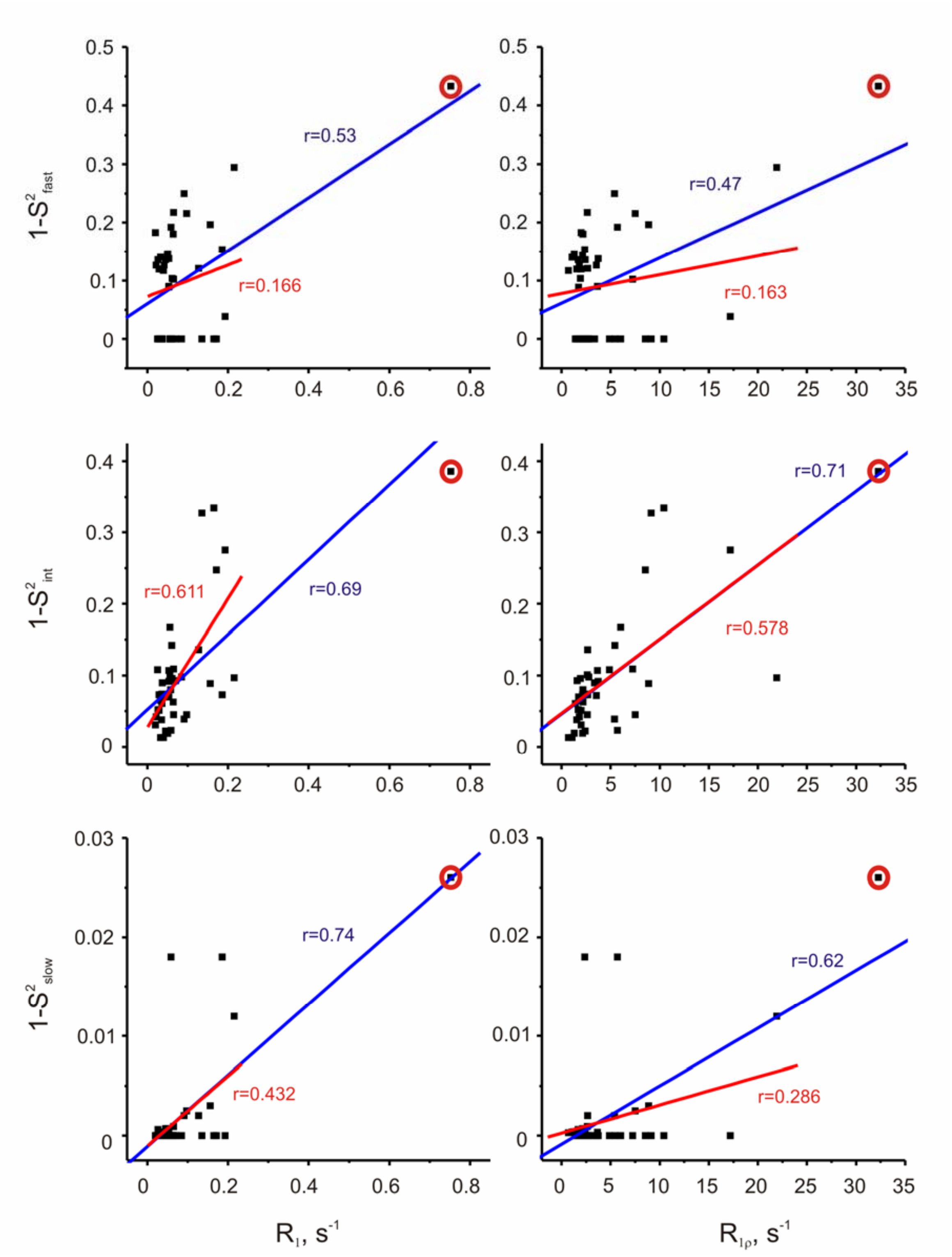

Fig. 43. Correlation between $R_{1\rho}$ /R_1 and motional amplitudes (1-S^2) for the fast (top), intermediate (middle) and slow (bottom) motions (AIC based selection of the model). The correlation coefficients were calculated with (blue) and without (red) D62 data. By exclusion of D62, the only remaining correlation coefficient is for intermediate motion. R_1's were measured at 600 MHz and T=12 °C; $R_{1\rho}$'s were measured at 400 MHz, on-resonance spin-lock frequency 8 kHz, MAS 20 kHz and T=10 °C.[165]

There should be another reason for the correlation between parameters characterizing mobility on different timescales. The reason could be the existence of intense intermediate motions which influences both measured relaxation rates R_1 and $R_{1\rho}$. Indeed, the correlation plots (fig. 43) show the connection of the amplitude of the intermediate motions with both relaxation rates. Thus, the high amplitude motions with correlation time on the order 10^{-8} s contribute to both R_1 and $R_{1\rho}$.

The results of this work contradict the conclusions of Yang *et al.*[53] They presumed a correlation between motions in different time windows through the comparison of several NMR parameters. R_1's, liquid-state order parameters, motionally averaged solid-state dipolar couplings, measured in thioredoxin. However, the intermediate motions occurring with high amplitudes affect all measured NMR parameters in the work. In that case, these parameters can seem correlated, even though fast and slow motions are not correlated at all.

Another kind of correlation was assumed between the raw NMR parameters characterizing dynamics of proteins and their secondary structure. It is believed, that mobility tracks secondary structure with greater intensity in the termini and loops.[53,126,127,131] Based on the derived dynamical parameters, we can reveal their correlation with the secondary structure. Table 4 demonstrates mean values of $1\text{-}S^2$ for different structural elements on different timescales along with raw data – motionally averaged dipolar couplings and R_1 and $R_{1\rho}$.

Table 4. Mean and RMSD values of the simulated motional parameters and experimental data.[165]

Time scale of the motion	β-sheets	unstructured	side chains
Motional amplitudes, model selection based on *AIC* values			
Fast	0.08±0.084	0.144±0.112	0.172±0.231
Intermediate	0.109±0.1	0.088±0.076	0.399±0.357
Slow	0.0017±0.0055	0.0023±0.0057	0.0067±0.01
Motional amplitudes, "two motions" model			
Fast	0.072±0.056	0.092±0.057	0.043±0.079
Intermediate	0.111±0.101	0.095±0.056	0.388±0.299
Slow	$4.3\cdot10^{-5}\pm1.6\cdot10^{-4}$	0.01±0.031	0.006±0.008
Motional amplitudes, "three motions" model			
Fast	0.147±0.061	0.18±0.07	0.308±0.207
Intermediate	0.066±0.072	0.059±0.081	0.325±0.324
Slow	0.0086±0.018	0.0114±0.027	0.0082±0.0094

Experimental NMR parameters			
$1-S^2$	0.203±0.062	0.233±0.112	0.4935±0.308
R_1 (*600 MHz, t=14 °C*)	0.173±0.129	0.282±0.425	0.496±0.476
On-resonance $R_{1\rho}$ (ν_{1e}*=8kHz, t=10 °C*)	5.04±5.32	4.63±6.4	7.06±7.83

The only feature that was revealed for the backbone is that the mean amplitude of the fast motion in β-sheets is less than in unstructured parts of the protein. If one also considers the RMSD of the parameters, the correlation is not significant. Concerning other motional regimes no correlation was found.

Side chains are found to be more mobile in comparison with backbone on all scales of internal motions.

6.5.4. *Detection of slow motion based on the comparison of solution and solid-state derived order parameters*

A new approach for the detection of slow (nanosecond to microsecond) motions in proteins was suggested by Chevelkov *et al.*[54] The idea of the method is the following. From the solution-state relaxation data, the generalized order parameter S^2_{gen} is defined by the “model-free” approach. S^2_{gen} contains information about the motional amplitudes of the dynamics occurring up to several nanoseconds ($\tau_{overall\ tumbling}$). Their solid state analogs S^2_{DC} are obtained from the motionally averaged dipolar couplings ($S^2_{DC} = \left(D^{exp} / D^{rigid}\right)^2$). S^2_{DC} samples all the motions with $\tau_C < 10^{-6}$ s, approximately. Then both of the order parameters are compared for each residue. If some motions occur within the correlation time range $\tau_{overall\ tumbling} < \tau_C < 10^{-6}$ s, then the S^2_{DC} will be less than S^2_{gen}. The authors[54] did not detect any slow motions for most of the residues in the SH3 domain since $S^2_{DC} \approx S^2_{gen}$. However, there were two residues L8 and T24 for which the difference is rather significant. For these particular residues the existence of high-amplitude nanosecond to microsecond motions was inferred. With the results of the simultaneous analysis of experimental data characterizing mobility in a wide frequency range, it is possible to compare these results with those obtained by Chevelkov. Figure 44 demonstrates the product $S^2_{\text{int}} \cdot S^2_s$ as a function of the amino acid residue number. From this figure it is evident that almost all of the residues undergo slow motions with $5 \cdot 10^{-9} < \tau_C < 1 \cdot 10^{-6}$ s, however no peculiarities for L8 and T24 (marked by red open stars) follow from Fig. 44.

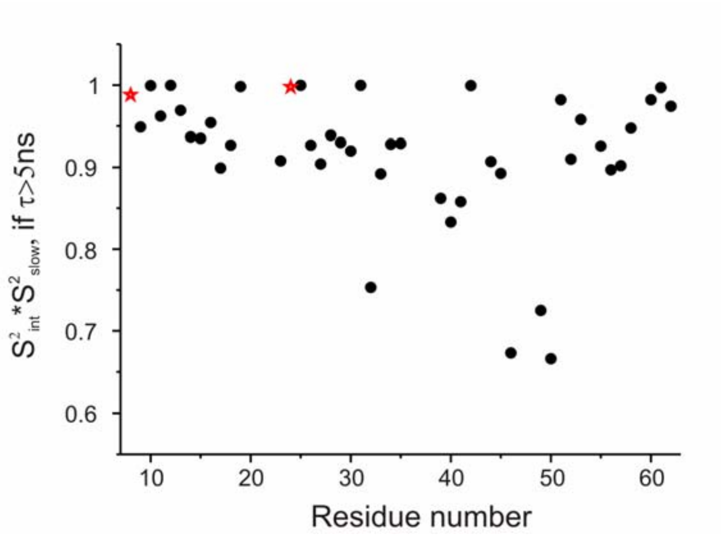

Fig. 44. Product of the order parameters of slow motions (τ_C is longer than the overall tumbling of the SH3 molecule tumbling). L8 and T24 residues are star-marked.[165]

The discrepancy in the conclusions of two works needs to be discussed. The fact that we, in contrast to the results of them, do detect slow motions in the nano to microsecond timescale, can be explained by the low amplitudes of these motions. The accurate determination of the motions through the comparison of the order parameters is rather low. Sometimes, $S^2_{DC} > S^2_{gen}$ is found, and cannot be due to physical reasons, but only because of experimental inaccuracy. Thus, the amplitude of such slow motions simply varies within the experimental error. The second reason can be the oversimplification of the form of the correlation function taken in frame of the “model-free” approach. The authors assumed the correlation function to be single exponential, and, at the moment, there is evidence of a more complex nature for the proteins dynamics.[4,5,11,116,122,132,147,175]

Chevelkov and co-workers were not the only ones who compared S^2_{DC} and S^2_{gen}. The same was made by Yang *et al*[53] with thioredoxin. In their work they concluded that, generally, both order parameters are the same and their difference is within the experimental error.

To gain a better insight into the capability of the approach in revealing slow mobility, I present the comparison of S^2_{DC} and S^2_{gen}[171] (S^2_{DC}’s were kindly provided by Paul Schanda) for ubiquitin in Fig. 45. In addition to these parameters, Fig. 45 represents S^2_{RDC} obtained from the residual dipolar couplings (RDC) measured in aligning media. This work was performed by Salmon *et al.*[176] RDC values provide information on amplitudes of motion which are slower than the inverse frequency of the residual coupling (up to milliseconds).[22] According to the sensitivity to different motions occurring in different timescales, the inequality $S^2_{den} \geq S^2_{DC} \geq S^2_{RDC}$ can be written. It follows from the figure that S^2_{DC} and S^2_{gen} sets of the order parameters do not reveal any significant difference. Concerning S^2_{RDC} there is a disparity. Sometimes, the S^2_{RDC} values for the particular residues are larger than all other order parameters. From the physical point of view this is impossible, and the only explanation to the results is a large experimental error in these measurements.

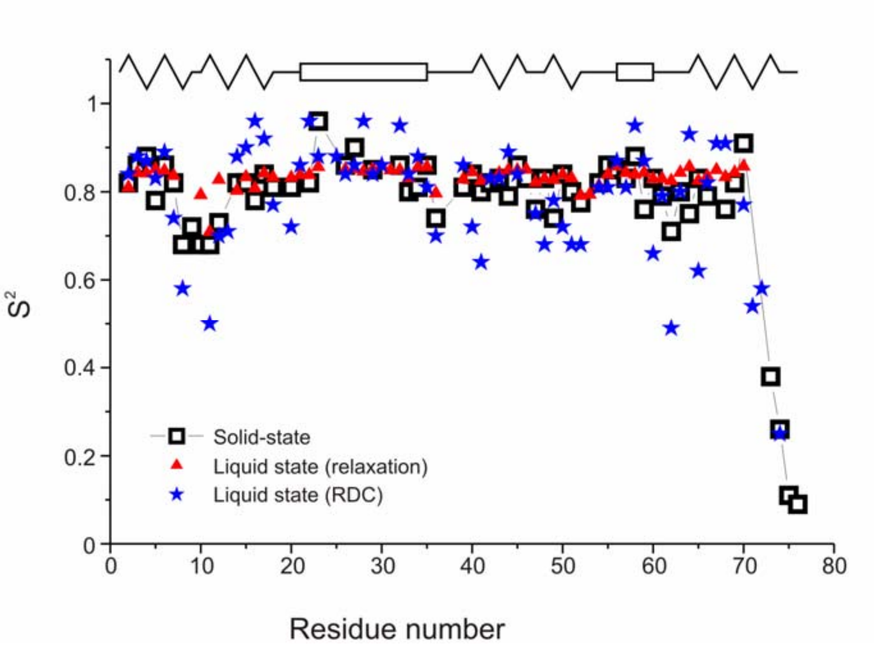

Fig. 45. Comparison of the order parameters derived from the ^{15}N relaxation experiments,[171] residual dipolar coupling (RDC) measurements in aligning media[176] and motionally averaged ^{15}N-^{1}H dipolar couplings[132] in ubiquitin. In the upper part of the figure the secondary structure is depicted. Rectangles symbolize β-sheets and a-helices are zigzagging lines.[165]

Thus, the approach of the slow motion detection implementing the comparison of solution and solid-state derived order parameters does not serve as a rigorous method.

6.6. Conclusions

The performed work shed light on the nature of internal protein mobility. Expansion of the motional frequency range by inclusion of $T_{1\rho}$ experiments enabled us to detect slow microsecond mobility for a large number of the amino acid residues. Now, it is evident that two-components of the correlation functions are often not enough for the adequate description of the complex hierarchy of backbone mobility. Besides the large experimental errors in the determination of relaxation parameters, the simultaneous analysis of all of them provides a great sensitivity in the detection of different motions even with order parameters and very different populations of exchanging sites. It is possible to further increase the accuracy of the dynamic parameter determination by measuring detailed temperature dependencies. However, this requires impractically long experimental times.

Based on the results of the work, some inconsistencies of previously accepted ideas were revealed. For example, that slow motions are facilitated by the increased fast mobility. Any confirmation for a correlation between motions in different timescales was not found.

During this work conclusions about the correlation of mobility with secondary protein structure made by other authors were confirmed. Fast motions with correlation times less than 10^{-9} s are restricted in the centers of the secondary structural elements. However, with slower motions this tendency was not proven.

The nature of internal protein dynamics is reflected in their dynamic parameters. We found the main feature in the distribution of motional amplitudes according to the correlation times. The shorter the correlation time the less restricted the motions are, as reflected in the derived order parameters. The gap in 10^{-10} – 10^{-9} s demonstrates the separation of different protein motions. The faster are believed to be due to collective librations, while the slower are large-amplitude jumps between non-equally populated subconformations.

This investigation confirms the existence of sizable dynamics in protein molecules that spans many orders of correlation times. Even the analysis of the most abundant set of experimental parameters cannot reliably describe all of them. The nature of protein dynamics is too complex. For simple motional models and their assumptions are often not enough for a comprehensive picture.

7. Summary

NMR is a powerful tool for the investigation of protein dynamics in a wide-frequency range. It allows better insight into the characteristic features of different types of motions. Besides the fact that for a long time solid-state NMR experiments lagged behind solution state dynamics investigations, it can provide more abundant information on the mobility in a globule. The absence of overall molecule tumbling expands the correlation time window of the dynamic investigations. The anisotropic parts of the interactions which are not averaged out in powder and crystalline proteins serve successfully as dynamic probes.

During this work several important questions were adressed. Here, I will summarize all the results.

Hydration response of protein dynamics

The main question arising in solid-state NMR investigations of proteins is the influence of the inter- and intra-molecular contacts on the dynamic behaviour. In the third part of the thesis, I showed that the dynamics of proteins in the hydrated stated significantly resembles or is even the same as in the native state for motions faster than 10^{-6}-10^{-5} s. Besides the fact that different motions have different hydration responses, the dynamics with $\tau_C < 10^{-5}$ s resembles native dynamics already at the humidity level of 0.4-0.5. In the microcrystalline state, the water content can reach 0.8, which is proved to be enough for providing native mobility. This validates studies of slow microsecond motions in proteins crystalline states, which are believed to be very important for protein function.

Microsecond dynamics studied by $T_{1\rho}$

The measurements of site-specific relaxation rates $R_{1\rho}$ in the microcrystalline protein showed a large distribution for the values of relaxation time constants. $R_{1\rho}$'s are sensitive to the microsecond dynamics. To cause such an alteration in the profile, motional correlation times should fit to the method sensitivity window. Thus, the confirmation of the existence of mobility that is slower than nanoseconds was obtained. Now, there is evidence that except picosecond and nanosecond dynamics, which were obtained by other authors, sizable microsecond mobility is likely.

General $R_1/R_{1\rho}$ equations

In the fifth part, I perform simulations to check validity and limits of applicability of the general equations for spin-lattice relaxation rates. These recently derived equations take into account both magic angle spinning and frequency off-set of the spin-lock field pulse. As a result of simulations it was found that analytically calculated relaxation rates are the same as simulated for the vast majority of the “experimental” conditions. The discrepancy was found only in the case of rotatary resonance, making the acquisition of dynamic information impossible. Thus, these equations can be used to derive the correlation function of motion from the measured relaxation rates, and will help to describe quantitatively protein motions with site-specific resolution.

Quantitative analysis of protein dynamics

The last part was devoted to the quantitative analysis of protein mobility in the frame of the “model-free” approach. It was found that proteins possess a complex nature of internal motions, and just two components of the correlation function are often not enough for adequate description. It is possible to divide protein mobility in three groups. The fastest motions occur due to collective librations and have the correlation time of $\tau_C < 10^{-10}$ s. Nanosecond motions involve all protein residues and are caused by large-amplitude jumps between subconformations. Additionally, the existence of slow microsecond motions for some of the residues was detected. This motion occurs between states with very different populations, and solid-state NMR in this case, turned out to be more sensitive than liquid-state chemical exchange methods.

As a result of this investigation it was revealed that there was no correlation between mobility on different timescales, although it was earlier believed that the fast motions are a precursor of slower dynamics.

Despite the fact that to-date the most abundant set of the experimental parameters was included for simultaneous analysis, the data noise does not allow unambiguous definition of the number of motional processes. More detailed measurements on the temperature dependencies would solve this problem; however, this work would be too time-consuming to be practical.

The information about internal protein motions derived as a result of the work can now be used in further studies aimed at explaining the functional dynamics of various other proteins.

Appendix

1. *The calculation of z-magnetization of the spin system exposed to the uniform static magnetic field* $\vec{B}_0 = \left(0, 0, B_0\right)$

Zeeman Hamiltonian acting on a spin system in case of applied magnetic field $\vec{B}_0$ is:

$$\hat{H} = -\gamma\hbar B_0 \hat{I}_z \qquad 1$$

Where γ is the magnetogyric ratio, $\hbar$ is the reduced Plank's constant. The eigenfunctions of the hamiltonain are the wave functions describing possible eigenstates:

$$\hat{H}\left|I,m\right\rangle = E\left|I,m\right\rangle \qquad 2$$

The eigenfunctions of the $\hat{I}_z$ operator are the same as for the hamiltonian Eq. 1:

$$\hat{I}_z\left|I,m\right\rangle = m\left|I,m\right\rangle \qquad 3$$

Combining all above equations:

$$\hat{H}\left|I,m\right\rangle = -\gamma\hbar B_0 \hat{I}_z\left|I,m\right\rangle = -\gamma\hbar B_0 m \qquad 4$$

And the energies of the states are:

$$E_{I,m} = -\gamma\hbar B_0 m \qquad 5$$

If the spin system consists of isolated ½ spin, then there are two possible states, $\left|\frac{1}{2},\frac{1}{2}\right\rangle$ and $\left|\frac{1}{2},-\frac{1}{2}\right\rangle$. The corresponding energies are $-\frac{1}{2}\gamma\hbar B_0$ and $+\frac{1}{2}\gamma\hbar B_0$

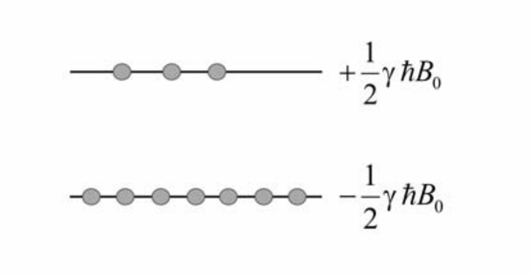

Fig. S1. Energy levels for the spin ½.

The population of different levels in the thermal equilibrium is described by Boltzmann distribution:

$$p_\psi = \frac{\exp\left(-E_\psi / kT\right)}{\sum\limits_\psi \exp\left(-E_\psi / kT\right)} \qquad 6$$

Considering that $\hat{\mu}_z = \gamma\hbar \cdot \hat{I}_z$, then it is possible to calculate the *z*-magnetization:

$$\begin{aligned}\left\langle \mu_z \right\rangle &= \gamma\hbar \sum_\psi p_\psi \left\langle \psi \right| \hat{I}_z \left| \psi \right\rangle = \gamma\hbar \left(p_{\frac{1}{2}} \left\langle \frac{1}{2},\frac{1}{2} \right| \hat{I}_z \left| \frac{1}{2},\frac{1}{2} \right\rangle + p_{-\frac{1}{2}} \left\langle \frac{1}{2},-\frac{1}{2} \right| \hat{I}_z \left| \frac{1}{2},-\frac{1}{2} \right\rangle \right) = \\ &= \gamma\hbar \left(\frac{1}{2} p_{\frac{1}{2}} - \frac{1}{2} p_{-\frac{1}{2}} \right) = \frac{1}{2}\gamma\hbar\Delta p \end{aligned} \qquad 7$$

Thus, *z*-magnetization of the ½ spin system is defined by the difference in population of energy levels.

2. *The calculation of y-magnetization for the spin system exposed to the uniform static magnetic field* $\vec{B}_0 = \left(0, 0, B_0\right)$ *and oscillating transverse field*

The interacting Hamiltonian can be written as:

$$\hat{H} = -\left(\gamma\hbar B_0 \hat{I}_z + \gamma\hbar B_1 \hat{I}_x\right) \qquad 8$$

In order to find the wavefunctions, it is necessary to solve Schrödinger equation:

$$i\frac{\partial \Psi\left(t\right)}{\partial t} = \hat{H}\left(t\right)\Psi\left(t\right) \qquad 9$$

Dealing with the time dependence of the hamiltonian can cause inconveniences. It is convinient to transform to the rotating frame (rotates around $\vec{B}_0$ with the frequency equal to ω_{rf}). In this frame the Hamiltonian has the form of:

$$H = \left(\hbar\left(\gamma B_0 - \omega_{rf}\right)\hat{I}_z + \hbar\gamma B_1 \hat{I}_x\right) \qquad 10$$

And the wavefunction transforms to:

$$\tilde{\Psi} = \exp\left(i\omega_{rf} t\hat{I}_z\right)\Psi \qquad 11$$

Then the Schrödinger equation is:

$$i\frac{\partial\tilde{\Psi}(t)}{\partial t} = \hat{H}\tilde{\Psi}(t) = \left(\hbar\left(\gamma B_0 - \omega_{rf}\right)\hat{I}_z + \hbar\gamma B_1 \hat{I}_x\right)\tilde{\Psi}(t) \qquad 12$$

Considering the isolated ½-spin nucleus, the basis set of the eigenfunctions is the set of eigenfunctions of $\hat{I}_z$. For convenience I will use reduced notion for them; $\left|\frac{1}{2}\right\rangle$ and $\left|-\frac{1}{2}\right\rangle$. Then, any state of the spin ½ at any moment in time can be described by the linear combination of these functions:

$$\Psi = c_{\frac{1}{2}}(t)\left|\frac{1}{2}\right\rangle + c_{-\frac{1}{2}}(t)\left|-\frac{1}{2}\right\rangle \qquad 13$$

Substitution of this form of the wavefunction to the Schrödinger equation results in:

$$i\left(\left|\frac{1}{2}\right\rangle\frac{\partial c_{\frac{1}{2}}(t)}{\partial t} + \left|-\frac{1}{2}\right\rangle\frac{\partial c_{-\frac{1}{2}}(t)}{\partial t}\right) = \hbar\gamma B_1 \hat{I}_x\left(c_{\frac{1}{2}}(t)\left|\frac{1}{2}\right\rangle + c_{-\frac{1}{2}}(t)\left|-\frac{1}{2}\right\rangle\right) \qquad 14$$

The multiplication of both sides of this equation on $\left\langle\frac{1}{2}\right|$ from the right side provides:

$$i\frac{\partial c_{\frac{1}{2}}(t)}{\partial t} = \frac{1}{2}\hbar\gamma B_1 c_{-\frac{1}{2}}(t) \qquad 15$$

Analogously after the multiplication of $\left\langle-\frac{1}{2}\right|$

$$i\frac{\partial c_{-\frac{1}{2}}(t)}{\partial t} = \frac{1}{2}\hbar\gamma B_1 c_{\frac{1}{2}}(t) \qquad 16$$

In this way, I derive the system of differential equations:

$$\begin{gathered} i\frac{\partial c_{\frac{1}{2}}(t)}{\partial t} = \frac{1}{2}\hbar\gamma B_1 c_{-\frac{1}{2}}(t) \\ i\frac{\partial c_{-\frac{1}{2}}(t)}{\partial t} = \frac{1}{2}\hbar\gamma B_1 c_{+\frac{1}{2}}(t) \end{gathered} \qquad 17$$

Solving the system of linear differential equations:

$$\frac{2}{\hbar\gamma B_1}\frac{\partial^2 c_{-\frac{1}{2}}(t)}{\partial t^2} + \frac{\hbar\gamma B_1}{2}c_{-\frac{1}{2}}(t) = 0 \qquad 18$$

The solution of this equation can be written in form of:

$$c_{-\frac{1}{2}}\left(t\right)=C_1\exp\left(i\frac{\hbar\gamma B_1}{2}t\right)+C_2\exp\left(-i\frac{\hbar\gamma B_1}{2}t\right) \tag{19}$$

From Eq. 16:

$$c_{\frac{1}{2}}\left(t\right)=\frac{2i}{\hbar\gamma B_1}\frac{\partial c_{-\frac{1}{2}}\left(t\right)}{\partial t}=-C_1\exp\left(i\frac{\hbar\gamma B_1}{2}t\right)+C_2\exp\left(-i\frac{\hbar\gamma B_1}{2}t\right) \tag{20}$$

Supposing the initial conditions $c_{\pm\frac{1}{2}}\left(0\right)$ it is possible to derive the linear coefficients of Eqs. 19 and 20.

$$\begin{aligned}
c_{-\frac{1}{2}}\left(t\right)&=c_{-\frac{1}{2}}\left(0\right)\cos\left(\frac{\hbar\gamma B_1}{2}t\right)-ic_{\frac{1}{2}}\left(0\right)\sin\left(\frac{\hbar\gamma B_1}{2}t\right)=\\
&=c_{-\frac{1}{2}}\left(0\right)\cos\left(\frac{\hbar\omega_1}{2}t\right)+ic_{\frac{1}{2}}\left(0\right)\sin\left(\frac{\hbar\omega_1}{2}t\right)\\
c_{\frac{1}{2}}\left(t\right)&=c_{\frac{1}{2}}\left(0\right)\cos\left(\frac{\hbar\gamma B_1}{2}t\right)-ic_{-\frac{1}{2}}\left(0\right)\sin\left(\frac{\hbar\gamma B_1}{2}t\right)=\\
&=c_{\frac{1}{2}}\left(0\right)\cos\left(\frac{\hbar\omega_1}{2}t\right)+ic_{-\frac{1}{2}}\left(0\right)\sin\left(\frac{\hbar\omega_1}{2}t\right)
\end{aligned} \tag{21}$$

Here, $\omega_1=-\gamma B_1$.

In the absence of the oscillating field the spin system can be described in terms of the populations:

$$\Psi\left(0\right)=\sqrt{p_{\frac{1}{2}}}\left|\frac{1}{2}\right\rangle+\sqrt{p_{-\frac{1}{2}}}\left|-\frac{1}{2}\right\rangle \tag{22}$$

where $p_{\pm\frac{1}{2}}$ are the populations of the Zeeman energy levels. Then the spin state coefficients are expressed by:

$$\begin{aligned}
c_{-\frac{1}{2}}\left(t\right)&=\sqrt{p_{-\frac{1}{2}}\left(0\right)}\cos\left(\frac{\hbar\omega_1}{2}t\right)+i\sqrt{p_{\frac{1}{2}}\left(0\right)}\sin\left(\frac{\hbar\omega_1}{2}t\right)\\
c_{\frac{1}{2}}\left(t\right)&=\sqrt{p_{\frac{1}{2}}\left(0\right)}\cos\left(\frac{\hbar\omega_1}{2}t\right)+i\sqrt{p_{-\frac{1}{2}}\left(0\right)}\sin\left(\frac{\hbar\omega_1}{2}t\right)
\end{aligned} \tag{23}$$

If a 90° pulse is applied to the system ($\hbar\omega_1 t=\pi/2$)

$$\begin{aligned}
c_{-\frac{1}{2}}\left(t\right)&=\sqrt{p_{-\frac{1}{2}}\left(0\right)}\cos\left(\frac{\pi}{4}\right)+i\sqrt{p_{\frac{1}{2}}\left(0\right)}\sin\left(\frac{\pi}{4}\right)\\
c_{\frac{1}{2}}\left(t\right)&=\sqrt{p_{\frac{1}{2}}\left(0\right)}\cos\left(\frac{\pi}{4}\right)+i\sqrt{p_{-\frac{1}{2}}\left(0\right)}\sin\left(\frac{\pi}{4}\right)
\end{aligned} \tag{24}$$

To find the populations of the states $p_{\pm\frac{1}{2}}=c_{\pm\frac{1}{2}}\left(t\right)^{*}c_{\pm\frac{1}{2}}\left(t\right)$:

$$\begin{aligned}
p_{\frac{1}{2}}\left(t_{90^\circ}\right)&=\frac{1}{2}\left(p_{\frac{1}{2}}\left(0\right)+p_{-\frac{1}{2}}\left(0\right)\right)\\
p_{-\frac{1}{2}}\left(t_{90^\circ}\right)&=\frac{1}{2}\left(p_{-\frac{1}{2}}\left(0\right)+p_{\frac{1}{2}}\left(0\right)\right)
\end{aligned} \tag{25}$$

Analogously it possible to calculate populations after the 180° pulse:

$$p_{\frac{1}{2}}\left(t_{180^\circ}\right)=p_{-\frac{1}{2}}(0)$$
$$p_{-\frac{1}{2}}\left(t_{180^\circ}\right)=p_{\frac{1}{2}}(0) \qquad 26$$

Thus, the 90° pulse equalizes the populations of the spin states and 180° pulse inverts these populations.

The expectation value of the y-magnetization combining Eqs. 13 and 21 can be calculated as:

$$\left\langle \mu_y \right\rangle = \hbar\gamma \left\langle \Psi^* \middle| \hat{I}_y \middle| \Psi \right\rangle = \frac{1}{2}\left(\left(c_{-\frac{1}{2}}(0)\right)^2 - \left(c_{\frac{1}{2}}(0)\right)^2\right)\sin\left(\omega_1 t\right) \qquad 27$$

3. *Perturbation theory*

Perturbation theory is a set of simplifications designed to describe real, complicated quantum systems. The idea of the method is the following. The dominating interaction in the spin system characterized by the Hamiltonian $\hat{H}_0$ has known eigenstates and energy levels defined as:

$$\hat{H}_0\left|\psi\right\rangle = E\left|\psi\right\rangle \qquad 28$$

If this interaction is strong compared to all other weak interactions $\hat{H}_1$, then the latter can be represented as perturbing the energy levels. The only part of the perturbing Hamiltonians $\hat{H}_1$'s which have the same eigenfunctions as Hamiltonian $\hat{H}_0$ (secular part) are considered. Thus, secular $\hat{H}_1$'s commute with $\hat{H}_0$. This does not necessarily mean that the other terms of $\hat{H}_1$'s, which do not commute with the dominating Hamiltonian, have no influence on energy levels, but this effect is supposed to be minor.

The condition of the applicability of the theory is that the perturbing interaction is small compared to energy difference of non-perturbed system.[177]

4. *Irreducible tensor operators*

Nuclear spin Hamiltonian includes different interactions (λ) between spin pairs (i,j)

$$\hat{H}_{ij}^{\lambda} = C_{ij}^{\lambda}\sum_{k}\sum_{q=-k}^{k}(-1)^q R_{k,-q}^{ij} T_{kq}^{ij} \qquad 29$$

Here C_{ij}^{λ} contains all physical constants corresponding to the interaction. This equation is written alternatively to Cartesian spin Hamiltonian, where $R_{k,-q}^{ij}$ and T_{kq}^{ij} are irreducible tensor operators representing spatial and spin parts of Hamiltonian, respectively. Here, *k* is the rank of the operator and *q* is the order of each irreducible tensor operator. Then, the spatial part is represented by spherical tensor functions. Such a representation of the Hamiltonian is convenient, when rotation in three-dimension space is used. The rank of the tensor operators does not depend on the rotation. The transformation of the irreducible tensor operators from one axis frame to another can be expressed as:

$$\hat{T}_{kq}^{new} = \hat{R}^{-1}(\alpha,\beta,\gamma)\hat{T}_{kq}^{old}\hat{R}(\alpha,\beta,\gamma) = \sum_{q'}\hat{T}_{kq'}^{old}D_{q'q}^{k}(\alpha,\beta,\gamma) \qquad 30$$

Here $\hat{R}(\alpha,\beta,\gamma)$ is an operator of the rotation and α,β,γ are the Euler angles describing the rotation of the old frame into the new one. The transformation includes rotation about the *z*-direction by γ angle, then, β around *y*, and α around *z*. $D_{q'q}^{k}(\alpha,\beta,\gamma)$ are the elements of the Wigner rotation matrix:

$$D^{k}_{q'q}\left(\alpha,\beta,\gamma\right)=\exp\left(-i\alpha q'\right)\exp\left(-i\gamma q\right)d^{k}_{q'q}\left(\beta\right) \tag{31}$$

Irreducible tensor operators of singular spin for different ranks and orders are:

$$\begin{gathered}\hat{T}_{00}=\frac{1}{\sqrt{2}}\\ \hat{T}_{10}=\sqrt{2}\hat{I}_z \quad \hat{T}_{1\pm1}=\mp\sqrt{\frac{1}{2}}\left(\hat{I}_x\pm i\hat{I}_y\right)\\ \hat{T}_{20}=\sqrt{\frac{1}{6}}\left(3\hat{I}_z^2-\hat{\mathrm{I}}\cdot\hat{\mathrm{I}}\right) \quad \hat{T}_{2\pm1}=\mp\left(\hat{I}_\pm\hat{I}_z+\hat{I}_z\hat{I}_\pm\right) \quad \hat{T}_{2\pm2}=\frac{1}{2}\hat{I}_\pm^2\end{gathered} \tag{32}$$

In the case of two spins *I* and *S*:

$$\begin{gathered}\hat{T}_{00}=-\frac{2}{\sqrt{3}}\left(\hat{I}_z\hat{S}_z+\frac{1}{2}\left(\hat{I}_+\hat{S}_-+\hat{I}_-\hat{S}_+\right)\right)\\ \hat{T}_{10}=\frac{1}{\sqrt{2}}\left(\hat{I}_-\hat{S}_+-\hat{I}_+\hat{S}_-\right) \quad \hat{T}_{1\pm1}=\left(-\hat{I}_\pm\hat{S}_z+\hat{I}_z\hat{S}_\pm\right)\\ \hat{T}_{20}=\sqrt{\frac{1}{6}}\left(3\hat{I}_z\hat{S}_z-\hat{\mathrm{I}}\cdot\hat{\mathrm{S}}\right) \quad \hat{T}_{2\pm1}=\mp\frac{1}{2}\left(\hat{I}_\pm\hat{S}_z+\hat{I}_z\hat{S}_\pm\right) \quad \hat{T}_{2\pm2}=\frac{1}{2}\hat{I}_\pm\hat{S}_\pm\end{gathered} \tag{33}$$

The hamiltonian for the dipolar interaction in terms of the irreducible tensor operators can be then written as:

$$\hat{H}_{dd}=\sqrt{6}\frac{\hbar\gamma_I\gamma_S}{r^3}\sum_{q=-2}^{2}\left(-1\right)^q D^{(2)}_{0,-q}\left(\alpha,\beta,\gamma\right)\hat{T}_{2q}\left(\hat{\mathrm{I}},\hat{\mathrm{S}}\right) \tag{34}$$

The spin part of the hamiltonian is associated with the spherical tensor operator $\hat{T}_{2q}\left(\hat{\mathrm{I}},\hat{\mathrm{S}}\right)$ and Wigner matrices define spatial contribution.

5. *The comparison of the correlation functions for the "wobbling-in-a-cone" model and the correlation function using the Fuoss-Kirkwood distribution function*

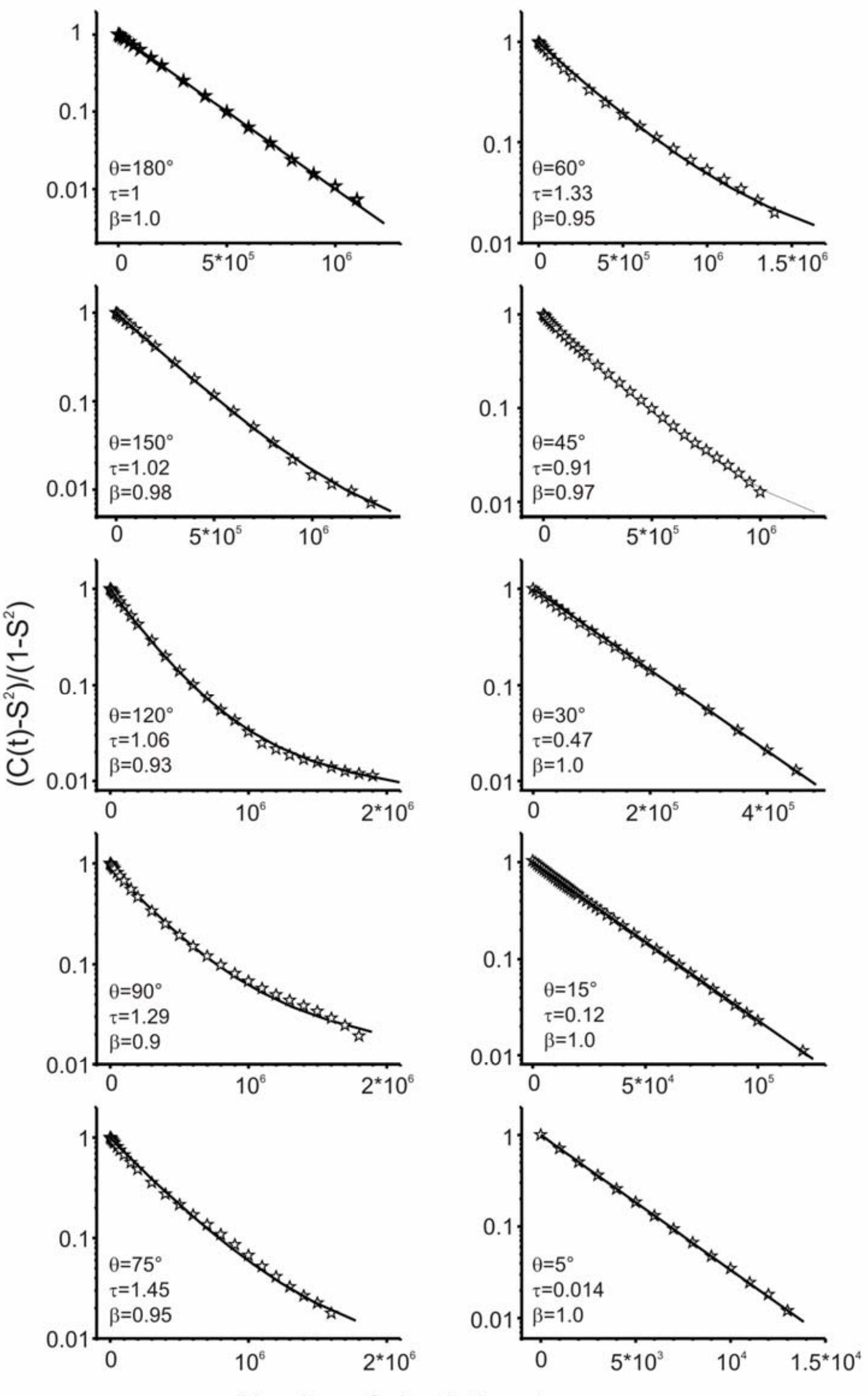

Fig. S2. Comparison of the computer simulations of the internuclear vector diffusion-in-a-cone[92] and numerical calculation of the correlation function using the Fuoss-Kirkwood distribution function. τ is the correlation time, and β represents the distribution width parameter, θ is cone semiangle.

6. *Input files for the SPINEVOLUTION simulations of $T_{1\rho}$ experiments*

a) Input file for the on-resonance ^{15}N-$T_{1\rho}$ relaxation measurements for the CSA mechanism.

The System	
spectrometer(MHz)	400
spinning_freq(kHz)	1
channels	N15
nuclei	N15 N15
atomic_coords	*
cs_isotropic	*
csa_parameters	1 100 0 0 0 0 ppm
csa_parameters	2 100 0 0 60 0 ppm
j_coupling	*
quadrupole	*
dip_switchboard	*
csa_switchboard	*
exchange_nuclei	(1 2)
bond_len_nuclei	*
bond_ang_nuclei	*
tors_ang_nuclei	*
groups_nuclei	*
*****Pulse Sequence*****	
CHN 1	
timing(usec)	5
power(kHz)	50
phase(deg)	0
freq_offs(kHz)	0
******Variables******	
k_1=4.35	
*****Options********	
rho0	I1x+I2x
observables	I1x+I2x
EulerAngles	angles.96b
n_gamma	96
line_broaden(Hz)	*
zerofill	*
FFT_dimensions	*
options	-v1 -re -t -scheck
**********************************	

The exchange in the form of “two-site” jumps occurs between two ^{15}N nuclei. The angle between their CSA tensors is 60°. The anisotropy value is 100 ppm. The exchange rate is defined by the parameter k_1 and is expressed in kHz. Timing defines the duration of the spin-lock pulse. The initial state of the spin system is described by I1x+I2x, the final state is the same. Euler Angles designed for the powder averaging, the same for n_gamma. Powder averaging was performed according to the repulsion scheme.[178] Lines with asterisks are not used by the program. Options:-v1 is the level of verboseness of the output during the calculations; -re is for the outputting only the real part of the signal; -t presents the outcome of the calculations in the command window instead of creating an output file; -scheck prevents the program from checking whether there is a synchronization of the pulses with MAS rotation.

b) Input file for the on-resonance ^{15}N-$T_{1\rho}$ relaxation measurements for the dipolar-coupling mechanism.

The System	
spectrometer(MHz)	400
spinning_freq(kHz)	10
channels	N15 H1
nuclei	N15 N15 H1
atomic_coords	1.015 0 0 0.5075 0.879 0 0 0 0
cs_isotropic	*
csa_parameters	*
j_coupling	*
quadrupole	*
dip_switchboard	nh.dat
csa_switchboard	*
exchange_nuclei	(1 2)
bond_len_nuclei	*
bond_ang_nuclei	*
tors_ang_nuclei	*
groups_nuclei	*
*****Pulse Sequence*****	
CHN 1	
timing(usec)	5
power(kHz)	50
phase(deg)	0
freq_offs(kHz)	0
CHN 2	
timing(usec)	5
power(kHz)	0
phase(deg)	0
freq_offs(kHz)	0
******Variables******	
k_1=1	
*****Options********	
rho0	I1x+I2x
observables	I1x+I2x
EulerAngles	angles.96b
n_gamma	96
line_broaden(Hz)	*
zerofill	*
FFT_dimensions	*
options	-v1 -re -t -scheck
**********************************	

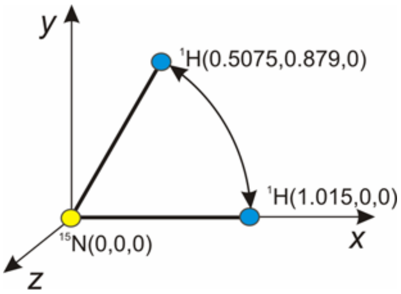

Fig. S3. Motional model for the case of the dipolar mechanism of relaxation.

nh.dat is a file to specify which dipolar interactions must be turned on. It has following lines:

```
*
1    *
1    0    *
```

It turns the interaction between ^{15}N nuclei and both protons.

c) Input file for the off-resonance ^{15}N-$T_{1\rho}$ relaxation measurements for the dipolar-coupling mechanism.

The System	
spectrometer(MHz)	400
spinning_freq(kHz)	10
channels	N15 H1
nuclei	N15 H1 H1
atomic_coords	0 0 0 0.5075 0.879 0 1.015 0 0
cs_isotropic	*
csa_parameters	*
j_coupling	*
quadrupole	*
dip_switchboard	nh.dat
csa_switchboard	*
exchange_nuclei	(1 2)
bond_len_nuclei	*
bond_ang_nuclei	*
tors_ang_nuclei	*
groups_nuclei	*
*****Pulse Sequence*****	
CHN 1	
timing(usec)	3.33 5
power(kHz)	50 50
phase(deg)	15 0
freq_offs(kHz)	0 28.867
CHN 2	
timing(usec)	3.33 5
power(kHz)	0 0
phase(deg)	0 0
freq_offs(kHz)	0 0
******Variables******	
k_1=1	
*****Options********	

rho0	I1x+I2x
observables	I1x+I2x
EulerAngles	angles.96b
n_gamma	96
line_broaden(Hz)	*
zerofill	*
FFT_dimensions	*
options	-v1 -re -t -scheck
********************************	

Frequency off-set of the spin-lock pulse is 28.867 kHz. The first pulse turns the magnetization on the angle 60° and then the spin-lock pulse is applied.

7. *Experimentally measured (violet rows) and simulated relaxation rates and dipolar coupling order parameters with residue resolution.* Signs “I”, “II”, and “III” (second column) correspond to the type of motional model: “one motion”, “two motions”, and “three motions”, respectively.
T_1 (A) - ^{15}N T_1 at 400 MHz, MAS rate 13 kHz, t=12 °C;
T_1 (B) - ^{15}N T_1 at 600 MHz, MAS rate 13 kHz, t=12 °C,
T_1 (C) - ^{15}N T_1 at 900 MHz, MAS rate 13 kHz, t=12 °C;
T_1 (D) - ^{15}N T_1 at 600 MHz, MAS rate 10 kHz, t=14 °C;
T_1 (E) - ^{15}N T_1 at 600 MHz, MAS rate 10 kHz, t=24 °C;
$T_{1\rho}$ (A) - ^{15}N $T_{1\rho}$ at 400 MHz, MAS rate 20 kHz, on-resonance spin-lock 8 kHz (^{15}N resonance frequency in the rotating frame), t=10 °C;
$T_{1\rho}$ (B) - ^{15}N $T_{1\rho}$ at 400 MHz, MAS rate 20 kHz, on-resonance spin-lock 13 kHz, t=27 °C;
$T_{1\rho}$ (C) - ^{15}N $T_{1\rho}$ at 400 MHz, MAS rate 20 kHz, on-resonance spin-lock 8 kHz, t=27 °C;
$T_{1\rho}$ (D)- ^{15}N $T_{1\rho}$ at 600 MHz, MAS rate 10 kHz, off-resonance spin-lock 35 kHz (effective ^{15}N resonance frequency in the tilted rotating frame), the off-resonance angle between B_0 and B_{1e} fields 24°, t=14 °C;
$T_{1\rho}$ (E) - ^{15}N $T_{1\rho}$ at 600 MHz, MAS rate 10 kHz, off-resonance spin-lock 35 kHz, the off-resonance angle between B_0 and B_{1e} fields 24°, t=24 °C;
$T_{1\rho}$ (F) - ^{15}N $T_{1\rho}$ at 600 MHz, MAS rate 10 kHz, off-resonance spin-lock 46.3 kHz, the off-resonance angle between B_0 and B_{1e} fields 24°, t=14 °C.

Residue №		Dip. Coupl. order parameters	T_1 (A)	T_1 (B)	T_1 (C)	T_1 (D)	T_1 (E)	$T_{1\rho}$ (A)	$T_{1\rho}$ (B)	$T_{1\rho}$ (C)	$T_{1\rho}$ (D)	$T_{1\rho}$ (E)	$T_{1\rho}$ (F)
L8	e	0.635±0.108	4.88±2.2	4.65±0.55	5.36±0.75	4.07±0.2		0.046±0.004	0.081±0.005	0.105±0.008	0.27±0.01	0.413±0.024	0.34±0.03
	III	0.636	3.96	4.23	4.75	4.3		0.044	0.087	0.096	0.28	0.415	0.336
V9	e	0.832±0.06	25.71±5.92	34.5±4.4	49.35±3.39		36.1±4.2	0.5±0.05	0.56±0.09	0.962±0.268	2.78±0.78		
	II	0.829	25.75	38.5	47.9		36.1	0.502	0.64	0.66	2.8		
L10	e	0.848±0.049	13.29±2.13	21.95±1.97	25.58±2.42		15.3±1.4	0.415±0.038	0.48±0.08	0.649±0.055			
	IIa	0.851	13.29	20.9	26.6		16	0.385	0.54	0.578			
A11	e	0.846±0.036	17.84±2.57	28.53±6.06	18.47±3.94			0.654±0.14	0.65±0.09	0.66±0.09			
	II	0.844	18.7	21.2	20.5			0.627	0.665	0.665			
L12	e	0.836±0.036	20.86±8.06	19.79±4.09	43.53±13.23			0.769±0.136	0.76±0.21	0.76±0.1			
	II	0.835	18.6	26	33.4			0.756	0.715	0.762			
Y13	e	0.79±0.035	40.51±8.34	49.32±4.26	41.4±5.8	36.9±6.7	42.7±7.8	0.5±0.05	0.5±0.07	0.67±0.12	4.5±1.3		3.57±1.07
	III	0.789	44.2	44.5	41.4	44.5	44.9	0.473	0.6	0.615	2.95		3.56
D14	e	0.766±0.038	13.85±2	15.57±3.75	19.35±1.96			0.46±0.03	0.49±0.05	0.66±0.03	3.85±1.41	3.13±0.5	
	III	0.768	13.8	16	18.8			0.46	0.532	0.535	2.88	2.91	

Residue №		Dip. Coupl. order parameters	T_1 (A)	T_1 (B)	T_1 (C)	T_1 (D)	T_1 (E)	$T_{1\rho}$ (A)	$T_{1\rho}$ (B)	$T_{1\rho}$ (C)	$T_{1\rho}$ (D)	$T_{1\rho}$ (E)	$T_{1\rho}$ (F)
Y15	e	0.8±0.047	23.86±3.93	29.9±1.4	37.56±2.53	19.8±1.9	26.4±2.5	0.53±0.12	0.61±0.07	0.645±0.046			
	III	0.797	19.2	27.5	37.5	24	26.4	0.503	0.645	0.645			
Q16	e	0.754±0.046	10.83±1.72	15.36±1.7	19.73±1.95	12.4±0.8	9±0.57	0.38±0.04	0.614±0.075	0.62±0.06	2.22±0.7		2.44±0.4
	III	0.757	8.77	14.6	19.73	12.3	10.1	0.385	0.6	0.593	2.15		2.39
E17	e	0.772±0.046	16.99±3.28	17.86±2.32	32.2±4			0.38±0.04	0.326±0.033	0.4±0.04	1.22±0.2		1.28±0.27
	II	0.767	14.1	21.6	26.8			0.28	0.326	0.35	1.4		1.4
K18	e	0.816±0.023	15.02±3.35	34.65±2	38.94±4.17	21±1.28	29.7±1.8	0.38±0.04	0.48±0.1	0.465±0.121	2.38±0.5		
	II	0.815	14.5	26.8	40.5	25.5	24.2	0.411	0.461	0.461	2.19		
S19	e	0.71±0.067	10.72±2.28	11.02±0.86	12.74±0.57	8.3±0.5	12.7±0.8	0.19±0.02	0.238±0.018	0.32±0.018	1.18±0.19	1.47±0.15	2.22±0.6
	III	0.701	9.5	10.5	12	10.2	11.1	0.193	0.264	0.264	1.29	1.37	2.06
E22	e	0.814±0.072	24.22±7.75			11.3±0.7	14±0.8	0.25±0.02			1.5±0.2	1.39±0.3	1.54±0.36
	II	0.803	12.7			12.5	15.2	0.244			1.38	1.49	1.54
V23	e	0.779±0.07	8.45±2.33	18.72±0.28	14.61±2.59		12.7±0.7	0.27±0.02	0.446±0.05	0.614±0.07			
	II	0.776	9.3	14.8	18.5		12.2	0.278	0.477	0.489			
T24	e	0.637±0.13	7.51±0.92	10.3±0.4	17.2±1.24	8.3±0.34	8.8±0.36	0.13±0.01	0.215±0.008	0.29±0.027	1.67±0.56		2.5±1
	III	0.639	7.15	10.4	14.6	9.45	8.77	0.138	0.228	0.228	0.966		1.42
M25	e	0.843±0.036	37.67±12.83	30.42±3.06	32.9±2.5	23 ±1.2	31.4±1.7	0.93±0.32	0.71±0.16	1.67±0.6			
	II	0.852	28.1	29.8	28.1	29.8	31.4	0.608	0.967	0.999			
K26	e	0.815±0.036	22.33±3.85	30.68±2.56	33.6±3.13	17±2.4	19.2±2.7	0.47±0.04	0.468±0.053	0.59±0.05			
	II	0.811	13.3	23.5	33.6	22.4	20	0.44	0.555	0.555			
K27	e	0.806±0.047	20.25±5.74	16.2±3.4	22.6±2.5		10.6±0.5	0.52±0.07	0.694±0.058		2.27±0.66		2.6±0.5
	II	0.8	9.51	16.6	22.6		12.6	0.428	0.688		2.31		2.31
G28	e	0.837±0.036	22.47±7.67	27.7±1.13	34.5±2.9	16.8±1.2	18.8±1.3	0.71±0.08	0.752±0.107	0.89±0.09	4.17±1.46		2.86±0.63
	III	0.835	17	22.3	29.2	21.7	20.7	0.627	0.823	0.823	3.2		3.2
D29	e	0.847±0.048	10.87±0.95	18.6±3.3	25.9±3.16			0.58±0.07	0.866±0.21	0.8±0.14			
	II	0.845	10.87	18.6	25.9			0.58	0.811	0.811			
I30	e	0.812±0.047	26.38±9.98	17.27±3.17	34.2±8.3		19.1±2.7	0.46±0.04	0.404±0.075	0.625±0.105			
	II	0.813	12.6	19.9	25.6		18.4	0.388	0.475	0.475			
L31	e	0.866±0.074	22.25±3.9	24.9±3.4	47.74±11.12		44±12	1.43±0.5	1.67±1.08	1.01±0.29			
	II	0.858	17.6	31	49.1		31.4	1.21	1.21	1.21			
T32	e	0.725±0.139	5.85±1.14	5.84±1.09	9.86±1.3		4.8±0.21	0.12±0.008	0.227±0.027	0.214±0.016		0.82±0.068	

Residue №		Dip. Coupl. order parameters	T_1 (A)	T_1 (B)	T_1 (C)	T_1 (D)	T_1 (E)	$T_{1\rho}$ (A)	$T_{1\rho}$ (B)	$T_{1\rho}$ (C)	$T_{1\rho}$ (D)	$T_{1\rho}$ (E)	$T_{1\rho}$ (F)
	II	0.723	4.26	6.73	8.78		5.1	0.111	0.215	0.215		0.088	
L33	e	0.853±0.061	23.63±4.96	39.8±.8	47.67±7.48	20.5±2.4	31.5±3.7	0.21±0.02	0.319±0.051	0.377±0.03	0.763±0.074		0.9±0.15
	II	0.853	20.4	32.9	40.8	28.9	22.9	0.155	0.32	0.32	0.981		0.981
L34	e	0.825±0.072	24.17±6.46	23.97±0.25	23.9±0.66		15.2±1.7	0.28±0.03	0.392±0.046	0.4±0.06			
	II	0.82	15.3	22.1	25.4		18.7	0.28	0.407	0.407			
K39	e	0.756±0.069	7.36±1.71	7.85±0.56	12.88±0.77			0.38±0.06	0.446±0.038	0.76±0.057	2±0.6		
	II	0.756	6.58	9.3	11			0.38	0.534	0.534	1.91		
D40	e	0.815±0.06	22.68±7.94	17.72±8.08	12.54±4.02		21±2.4	0.17±0.008	0.226±0.014	0.28±0.02		0.65±0.05	
	II	0.79	18.6	17	14.9		18.9	0.145	0.175	0.175		0.885	
W41	e	0.799±0.059	12.82±3.08	16.48±2.53	20.76±4.55			0.18±0.013	0.25±0.019	0.392±0.043	0.74±0.12		1.05±0.25
	II	0.795	12.4	18.1	20.1			0.139	0.27	0.27	0.861		0.861
W42	e	0.838±0.036	14.78±5.27	20.25±7.64	23.9±5.1			0.47±0.05	0.34±0.05	0.465±0.065			
	III	0.842	15.6	19.8	25.2			0.475	0.355	0.445			
V44	e	0.867±0.049	29.63±7.7	14.16±3.28	23.7±4.4			0.64±0.11	0.47±0.049	0.543±0.038			
	II	0.863	21.5	18.6	16.9			0.492	0.523	0.523			
E45	e	0.814±0.048	9.12±2.19	18.78±1.31	28.05±2.06		14±1.3	0.27±0.055	0.31±0.02	0.358±0.042			
	II	0.814	10.1	18	28		15	0.257	0.337	0.337			
V46	e	0.782±0.07	13.5±3.8	7.4±0.8	11.09±0.14			0.11±0.03	0.09±0.006	0.097±0.01	0.588±0.112	0.444±0.094	
	II	0.776	8.07	7.65	7.35			0.0967	0.096	0.096	0.5	0.505	
R49	e	0.696±0.044	6.56±3.07	5.18±0.43	7.57±0.94			0.058±0.004	0.087±0.005	0.091±0.007			
	II	0.694	5.95	6.17	6.05			0.059	0.0876	0.0876			
Q50	e	0.686±0.044	4.71±0.72	6.07±0.17	9.8±0.3	4.9±0.1	4±0.1	0.096±0.007	0.133±0.007	0.144±0.005	0.41±0.026	0.56±0.02	0.53±0.04
	II	0.679	3.21	6.17	9.8	5.43	4.25	0.084	0.133	0.133	0.466	0.595	0.466
G51	e	0.775±0.035	14.47±2.62	17.12±1.72	29.71±3.12	19.6±1.2	16.8±1	0.175±0.011	0.274±0.022	0.3±0.03	0.83±0.15	1.33±0.23	
	III	0.78	13.6	19.1	26.7	18.4	16.75	0.14	0.285	0.285	0.896	1.3	
F52	e	0.848±0.036	26.4±7.04	26.64±1.7	39.15±4.27	23 ±2.2	17.2±1.6	0.298±0.023	0.332±0.035	0.35±0.02			1.43±0.15
	II	0.854	14.5	25.6	37	24	20.4	0.248	0.35	0.35			1.43
V53	e	0.836±0.048	32.15±7.83	45.35±2.09	60.2±18.02			0.56±0.06	0.662±0.15	0.72±0.12	2.5±0.65		
	II	0.833	30.8	47.9	59.6			0.496	0.685	0.685	2.74		
A55	e	0.818±0.024	27.85±2.28	27.53±2.65	41.02±2.12	20.5±1.4	18.6±1.3	0.402±0.073	0.458±0.099	0.74±0.1		3.03±0.53	
	II	0.818	15.1	27	37.2	24.7	19.6	0.4	0.641	0.641		2.85	
A56	e	0.797±0.035	12.96±2	15.44±6.45	20.5±3.37			0.138±0.01	0.289±0.032	0.42±0.04			

Residue №		Dip. Coupl. order parameters	T_1 (A)	T_1 (B)	T_1 (C)	T_1 (D)	T_1 (E)	$T_{1\rho}$ (A)	$T_{1\rho}$ (B)	$T_{1\rho}$ (C)	$T_{1\rho}$ (D)	$T_{1\rho}$ (E)	$T_{1\rho}$ (F)
	IIa	0.789	12.8	16.3	18.8			0.167	0.301	0.353			
Y57	e	0.797±0.051	19.91±6.49	11.73±4.94	27.7±4.67			0.36±0.05	0.505±0.21	0.56±0.1			
	II	0.798	16.9	14.7	13.7			0.36	0.53	0.53			
V58	e	0.82±0.048	21.32±7.07	37.33±5.34	53.34±8.46		19.9±1.5	0.6±0.15	0.74±0.16	1.15±0.3			
	II	0.818	18.2	35.2	53.3		22.5	0.51	0.894	0.894			
K60	e	0.77±0.035	5.28±0.74	5.37±0.48	9.3±0.5				0.39±0.03	0.42±0.04	0.65±0.05		0.72±0.03
	III	0.77	5.3	6.7	9				0.39	0.42	0.65		0.7
L61	e	0.731±0.034	3.24±0.37	6.35±0.35	7.62±0.87	3.7±0.12	4.9±0.16	0.113±0.007	0.243±0.018	0.28±0.007	0.78±0.12	0.752±0.072	1.11±0.17
	III	0.73	3.39	5.26	7.31	4.38	4.48	0.116	0.243	0.243	0.73	0.87	1.1
D62	e	0.3	1.12±0.07	1.33±0.11	1.9±0.12	1.18±0.05	1.12±0.05	0.031±0.005	0.058±0.005	0.052±0.002	0.16±0.008	0.22±0.004	0.21±0.004
	III	0.298	0.973	1.36	1.9	1.22	1.17	0.0297	0.0537	0.0537	0.17	0.226	0.2
Side chains													
Q16a	e	0.088±0.01				0.82±0.05	0.766±0.04	0.13±0.02	0.235±0.017	0.235±0.022	0.625±0.084	0.568±0.05	0.645±0.09
	III	0.086				0.85	0.75	0.147	0.239	0.228	0.566	0.57	0.622
Q16b	e	0.088±0.013				0.94±0.07	1.2±0.1	0.14±0.03	0.228±0.031	0.27±0.034	0.787±0.098	0.75±0.11	0.741±0.116
	III	0.085				1.02	1.2	0.16	0.241	0.241	0.596	0.703	0.703
N35s	e	0.735±0.09		19.86±0.53	24.66±1.28	20±2.3	20±2.2	0.56±0.18	0.261±0.048	0.435±0.057	2.13±0.7		
	III	0.734		20.1	24.7	19.7	19.5	0.34	0.275	0.304	2.5		
N38s	e	0.756±0.11		22.41±7.22	33.2±5.1	21±3	27±4	0.27±0.07	0.365±0.053	0.435±0.04			
	III	0.755		23.2	32.2	21.1	27.3	0.265	0.396	0.396			
We41	e	0.768±0.12	5.11±0.27	7.3±0.4	13.3±0.56	5±0.23	2.9±0.13	0.039±0.003	0.021±0.002	0.027±0.002	0.135±0.003	0.114±0.002	0.227±0.008
	II	0.764	3.98	7.7	12.6	5.43	2.86	0.029	0.0217	0.0217	0.135	0.092	0.252
We42	e	0.832±0.012				17.7±2.6	47±7	0.535±0.054	0.366±0.04	0.555±0.096			
	III	0.832				17.7	47	0.535	0.415	0.434			
Q50a	e	0.391±0.005		1.81±0.03	1.88±0.04	1.44±0.14	1.12±0.2	0.225±0.01	0.275±0.027	0.397±0.031	1.23±0.17	0.752±0.05	1.05±0.14
	III	0.389		1.55	2.1	1.35	1.15	0.245	0.275	0.35	0.88	0.86	0.98
Q50b	e	0.394±0.006	1.26±0.12	1.89±0.03	1.88±0.04	1.56±0.07	1.2±0.07	0.248±0.06	0.267±0.024	0.333±0.013	0.82±0.07	0.61±0.06	0.787±0.083
	III	0.393	1.06	1.57	2.1	1.43	1.26	0.231	0.281	0.281	0.755	0.76	0.755

8. *Order parameters and correlation times for "two discrete motions" model.*

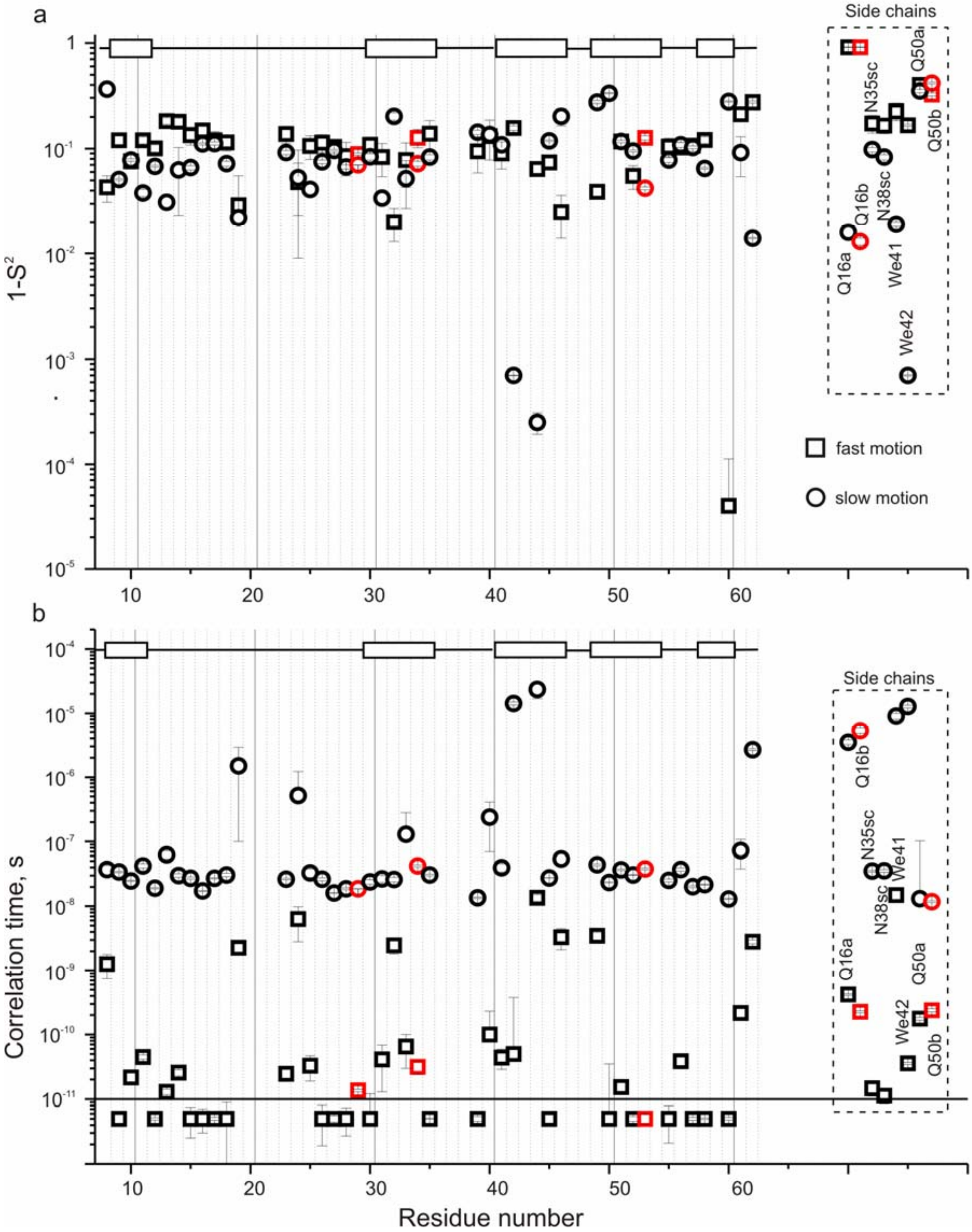

Fig. S4. Red marked residues corresponds to the minimum of AIC.

9. *Order parameters and correlation times for "three discrete motions" model.*

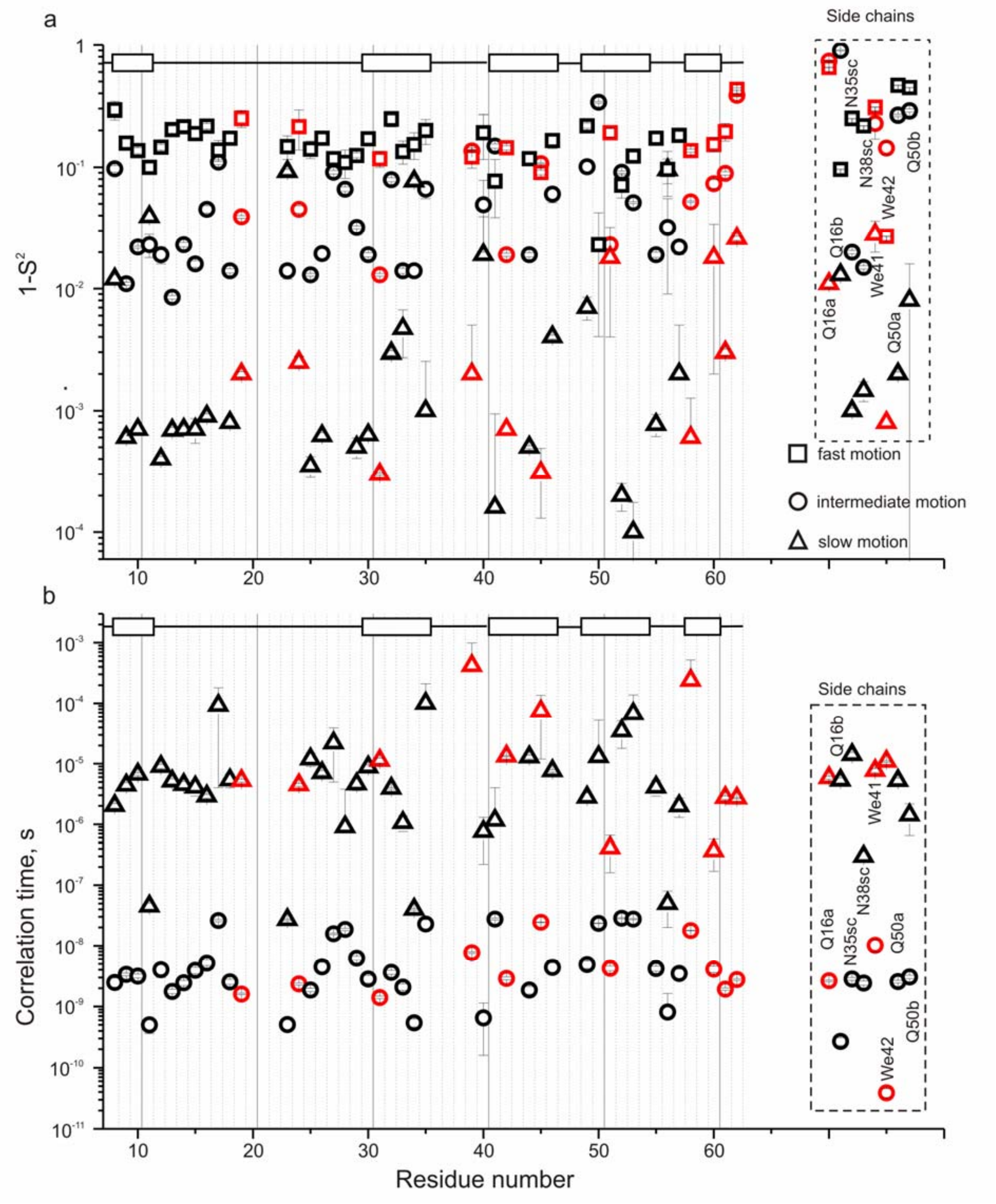

Fig. S5.Red marked residues corresponds to the minimum of AIC.

10. *Order parameters and correlation for "two motions with distribution" model.*

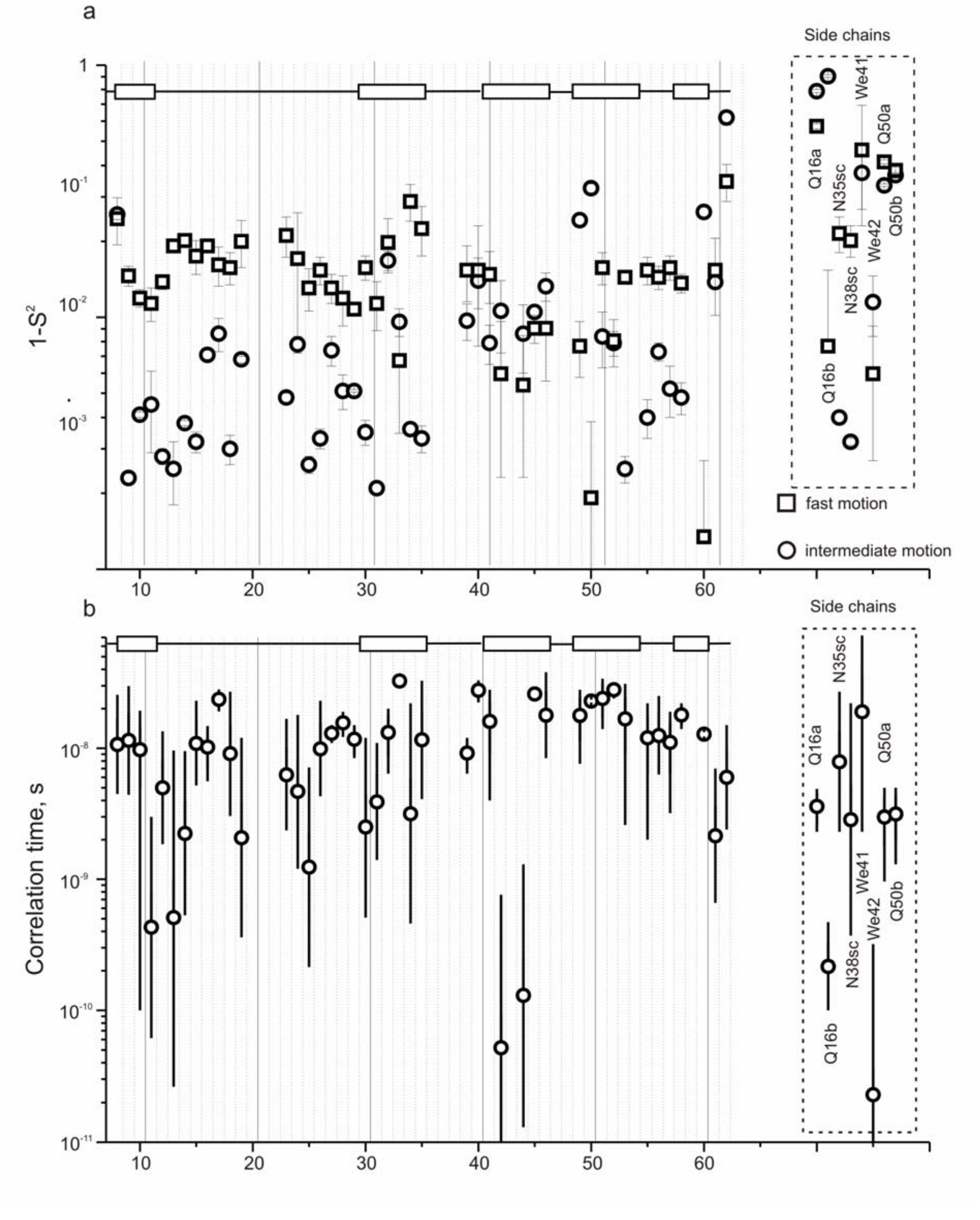

Fig. S6. In the b-plot, error bars denote the width of the distribution of correlation times. This width was calculated for each of the residues at the half of the height of correlation time distribution function (Eq.(2.50) and Fig. 13)

11. *Sum of amplitudes vs. correlation times. "Two motions"*

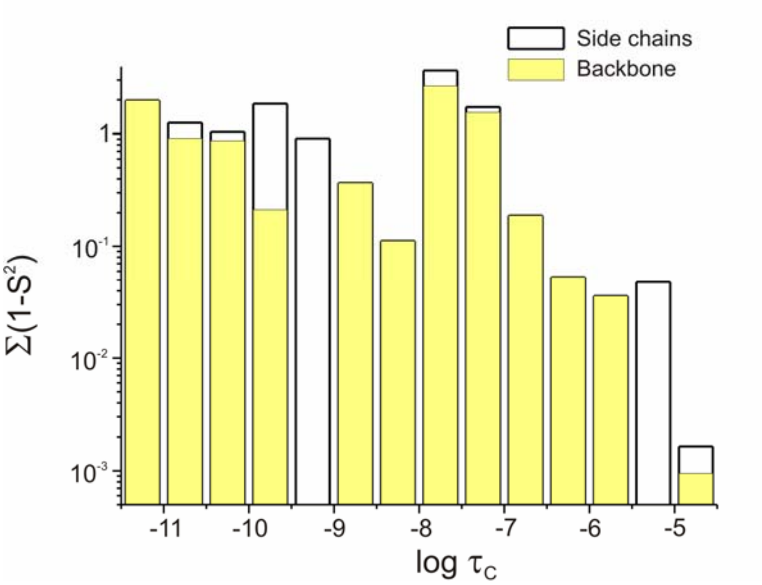

12. *Sum of amplitudes vs. correlation times. "Three motions"*

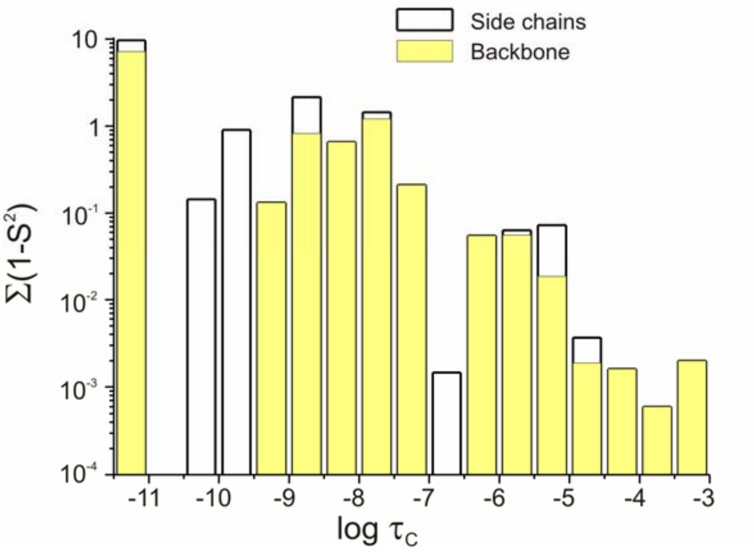

13. *Sum of amplitudes vs. correlation times. “Two motions with distribution”*

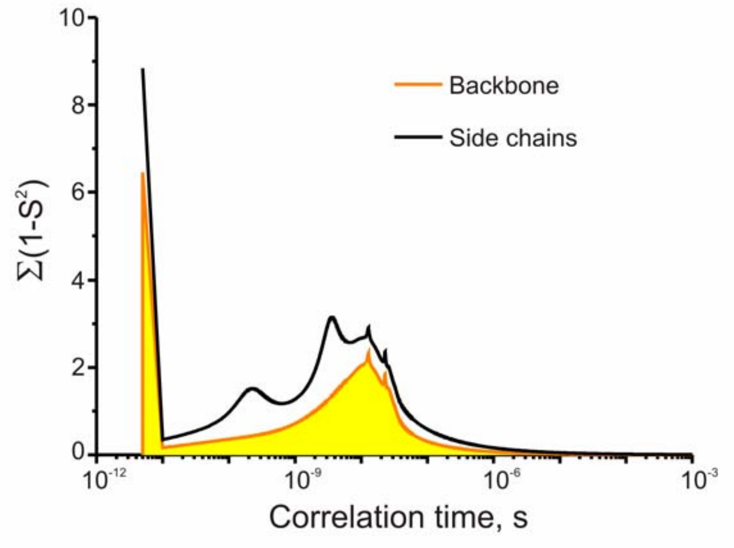

14. *Limitations of SPINEVOLUTION program*

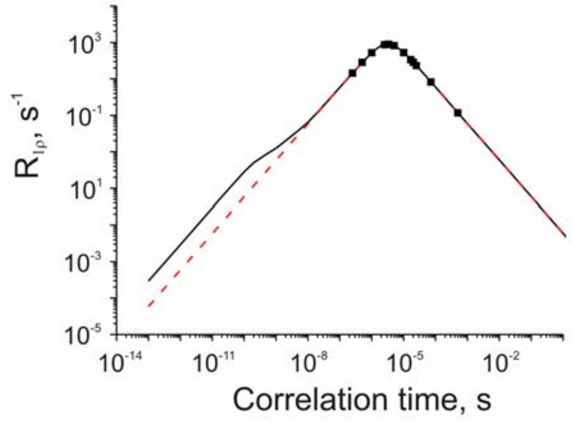

Here, the red line is calculated with just lower frequency spectral density terms of the equation (2.39), while the black one uses all terms including high frequencies. From the picture it is clear that at high frequencies of motions the T_1 contribution becomes more significant, but the SPINEVOLUTION program cannot perform these simulations properly. Simulation details: ^{15}N-^{1}H dipolar relaxation mechanism, on-resonance spin-lock field is 50 kHz, rotation frequency is 1 kHz, and motional model is “two-site” jumps.

15. *Activation energy limits. Alternative minimization protocol.*
The fitting with the minimization function expressed by Eq. (6.11)

Fitting model	Activation energy limitations, kJ/mol	
One motion	20.6±9.5	
Two motions with distribution	29.2±16.4	
Two motions	Fast	20±11
	Slow	23±11
Three motions	Intermediate	27±13
	Slow	46±15

16. *The RMSD and AIC values table. Alternative minimization protocol. (from minimization with a function expressed by Eq.* (6.11)*)*

RL	NP	RMSD 1	*AIC*1	RMSD 2a	*AIC*2a	RMSD 2	*AIC*2	RMSD 3	*AIC*3
L8	11	0.248	-2.2432	0.147	-2.92555	0.248	-1.69774	0.093	-3.47758
V9	9	0.186	-2.69735	0.136	-2.87909	0.141	-2.58466	0.152	-2.21219
L10	8	0.13	-3.33044	0.056	-4.51481	0.081	-3.52661	0.128	-2.36145
A11	7	0.317	-1.44056	0.131	-2.63654	0.146	-2.13401	0.135	-2.00496
L12	7	0.212	-2.2452	0.174	-2.06883	0.205	-1.4552	0.156	-1.7158
Y13	11	0.303	-1.84259	0.128	-3.20236	0.195	-2.1786	0.182	-2.13477
D14	9	0.256	-2.05849	0.125	-3.04777	0.182	-2.07416	0.108	-2.89569
Y15	9	0.206	-2.49309	0.129	-2.98477	0.14	-2.59889	0.117	-2.73561
Q16	11	0.138	-3.41555	0.074	-4.29829	0.106	-3.39772	0.122	-2.93474
E17	9	0.22	-2.36159	0.203	-2.07799	0.198	-1.90564	0.207	-1.59452
K18	10	0.15	-3.19424	0.14	-2.93223	0.146	-2.6483	0.143	-2.48982
S19	12	0.303	-1.88804	0.158	-2.85699	0.151	-2.78095	0.113	-3.19407
V23	8	0.231	-2.18068	0.154	-2.49161	0.135	-2.50496	0.135	-2.25496
T24	11	0.358	-1.50899	0.302	-1.48557	0.335	-1.09634	0.217	-1.78299
M25	9	0.392	-1.20632	0.241	-1.73481	0.235	-1.56301	0.298	-0.86577
K26	9	0.235	-2.22967	0.173	-2.39782	0.204	-1.84594	0.169	-2.00016
K27	9	0.289	-1.81599	0.215	-1.96312	0.231	-1.59734	0.241	-1.29036
G28	11	0.223	-2.45571	0.189	-2.42293	0.204	-2.08836	0.219	-1.76464
D29	9	0.0696	-4.66331	0.029	-5.96981	0.023	-6.21119	0.052	-4.35747
I30	8	0.316	-1.55403	0.223	-1.75117	0.246	-1.30485	0.22	-1.27826
L31	8	0.274	-1.83925	0.249	-1.5306	0.252	-1.25665	0.286	-0.75353
T32	9	0.182	-2.74083	0.129	-2.98477	0.125	-2.82555	0.112	-2.82296
L33	11	0.239	-2.31713	0.236	-1.97876	0.202	-2.10807	0.1995	-1.95115
L34	8	0.299	-1.66462	0.17	-2.29391	0.179	-1.94074	0.167	-1.82952
N35	11	0.366	-1.46479	0.311	-1.42683	0.357	-0.96913	0.233	-1.64071
K39	8	0.216	-2.31495	0.149	-2.55762	0.171	-2.03218	0.159	-1.9277
D40	9	0.461	-0.88205	0.311	-1.22481	0.219	-1.70403	0.233	-1.35788
W41	9	0.224	-2.32555	0.19	-2.21035	0.161	-2.31937	0.16	-2.10961
W42	7	0.23	-2.08221	0.116	-2.87976	0.166	-1.87725	0.071	-3.29015
V44	7	0.454	-0.72217	0.245	-1.38442	0.203	-1.47481	0.2	-1.21888

E45	8	0.056	-5.01481	0.055	-4.55084	0.059	-4.16044	0.028	-5.4011
V46	9	0.393	-1.20122	0.227	-1.8545	0.2	-1.88554	0.179	-1.88518
R49	7	0.307	-1.50467	0.141	-2.48942	0.127	-2.41285	0.107	-2.46985
Q50	12	0.139	-3.44656	0.123	-3.35781	0.14	-2.93223	0.137	-2.80888
G51	11	0.145	-3.31659	0.121	-3.31484	0.104	-3.43582	0.091	-3.52106
F52	10	0.217	-2.45572	0.177	-2.46321	0.198	-2.03898	0.21	-1.7213
V53	8	0.141	-3.16799	0.09	-3.56589	0.071	-3.79015	0.129	-2.34589
A55	10	0.248	-2.18865	0.191	-2.31096	0.223	-1.80117	0.195	-1.86951
A56	7	0.238	-2.01383	0.152	-2.33918	0.126	-2.42866	0.108	-2.45125
Y57	7	0.324	-1.39688	0.247	-1.36816	0.259	-0.98757	0.225	-0.98331
V58	8	0.149	-3.05762	0.132	-2.79991	0.144	-2.37588	0.063	-3.77924
K60	8	0.282	-1.7817	0.23	-1.68935	0.198	-1.73898	0.095	-2.95776
L61	12	0.198	-2.73898	0.184	-2.55231	0.199	-2.2289	0.143	-2.72315
D62	12	0.174	-2.9974	0.083	-4.1445	0.085	-3.93021	0.051	-4.78519
Side chains									
Q16a	9	0.168	-2.90092	0.132	-2.9388	0.119	-2.92393	0.104	-2.97117
Q16b	9	0.226	-2.30777	0.131	-2.954	0.121	-2.8906	0.117	-2.73561
N35	9	0.283	-1.85795	0.201	-2.09779	0.2	-1.88554	0.174	-1.94184
N38	8	0.16	-2.91516	0.11	-3.16455	0.176	-1.97454	0.087	-3.13369
W41	12	0.377	-1.45102	0.342	-1.31256	0.274	-1.58925	0.243	-1.66272
W42	6	0.383	-0.91944	0.286	-0.83686	0.199	-1.2289	0.183	-1.0632
Q50a	11	0.202	-2.65352	0.183	-2.48745	0.184	-2.29473	0.144	-2.60316
Q50b	12	0.175	-2.98594	0.122	-3.37414	0.175	-2.48594	0.122	-3.0408

17. *„One motion“ dynamic parameters. Alternative minimization protocol (from minimization with a function expressed by Eq.* (6.11)*)*

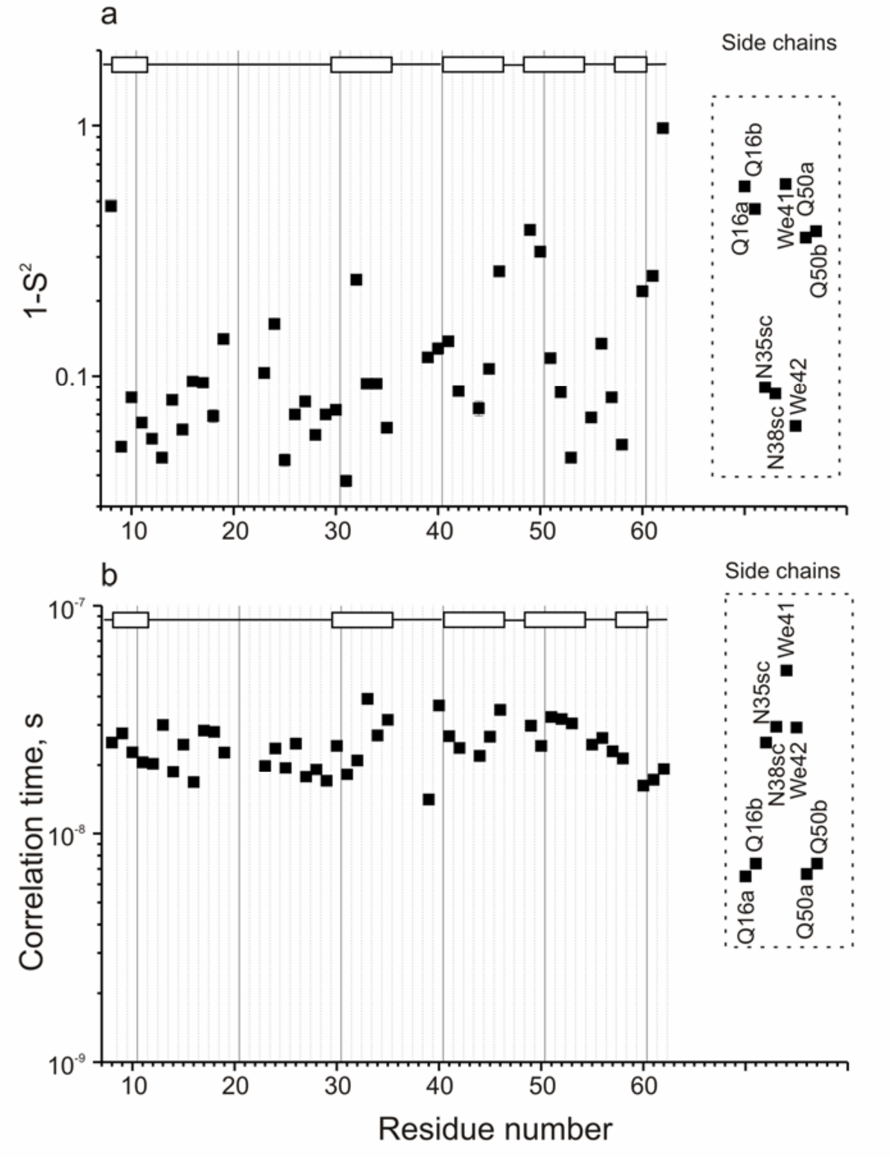

18. *„Two motions“ dynamic parameters. Alternative minimization protocol (from minimization with a function expressed by Eq.* (6.11)*)*

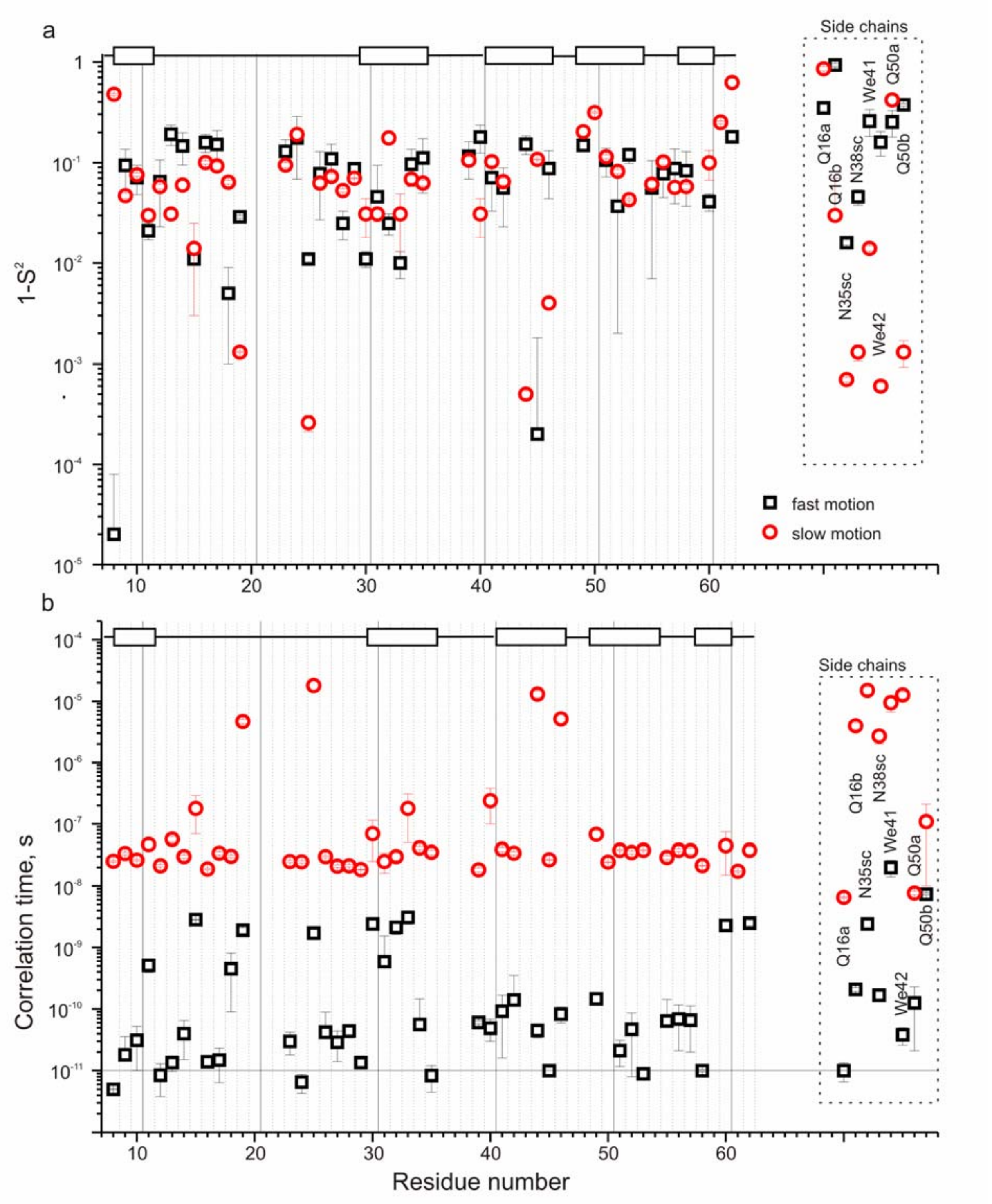

19. *„Three motions“ dynamic parameters. Alternative minimization protocol (from minimization with a function expressed by Eq.* (6.11)*)*

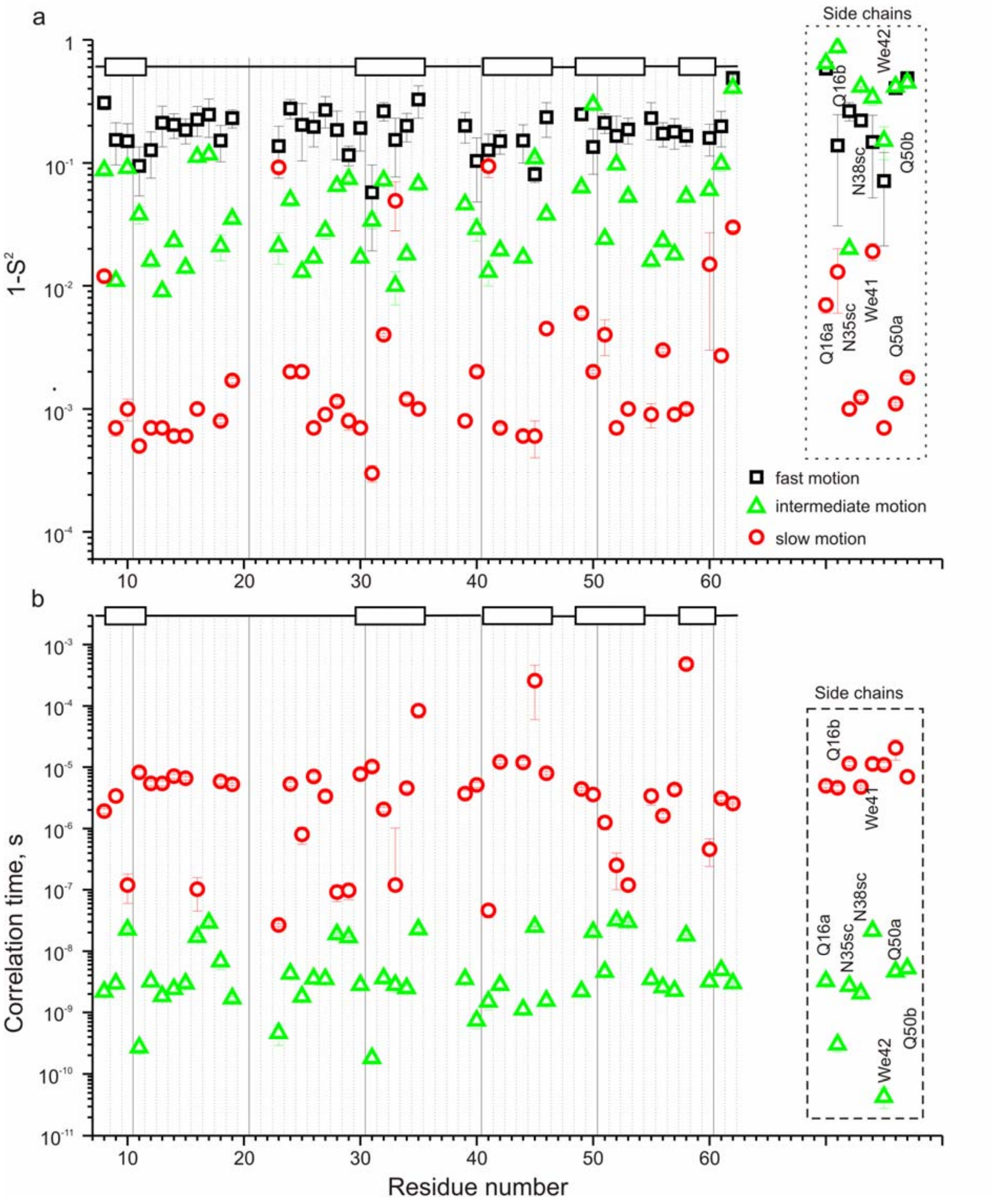

20. *„Two motions with distribution" dynamic parameters. Alternative minimization protocol (minimization with a function expressed by Eq.* (6.11)*)*

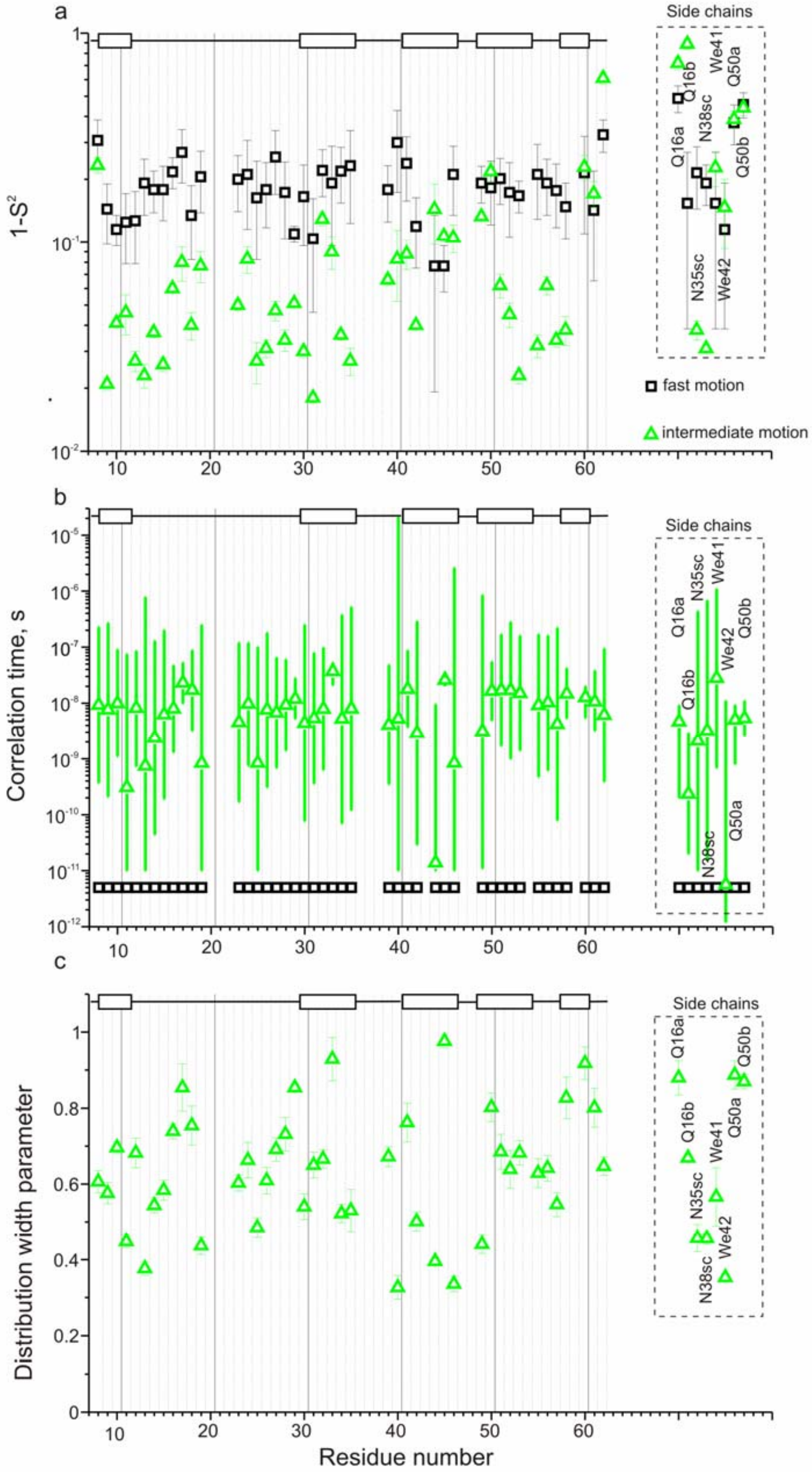

In the middle plot, error bars denote the width of the distribution of correlation times. This width was calculated for each of the residues at the half of the height of correlation time distribution function (Eq.(2.50) and Fig. 13)

21. *Final dynamic parameters. Alternative minimization protocol (best fitted during the minimization with a function expressed by Eq.* (6.11)*)*

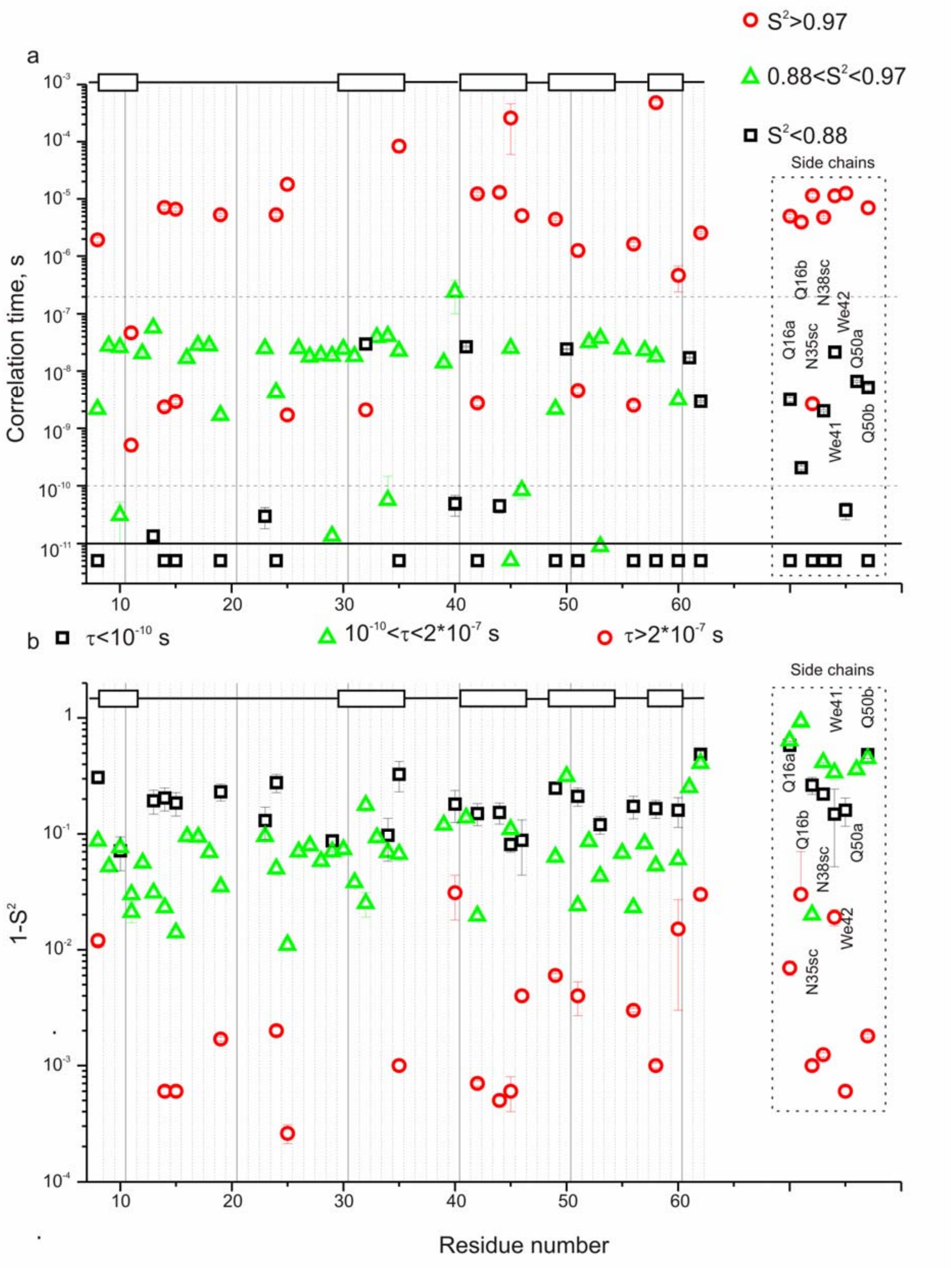

22. *Sum of amplitudes vs. correlation times. "Two motions". Alternative minimization protocol (minimization with a function expressed by Eq.* (6.11)*)*

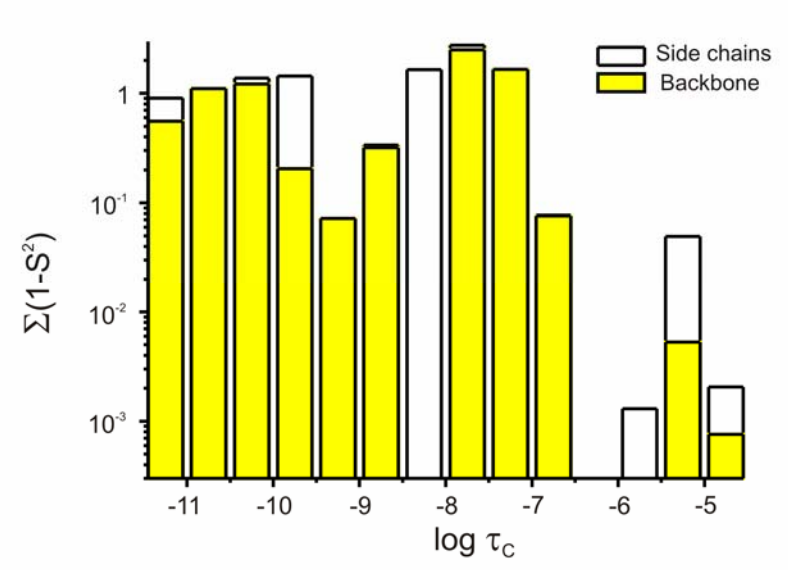

23. *Sum of amplitudes vs. correlation times. "Three motions" Alternative minimization protocol (minimization with a function expressed by Eq.* (6.11)*)*

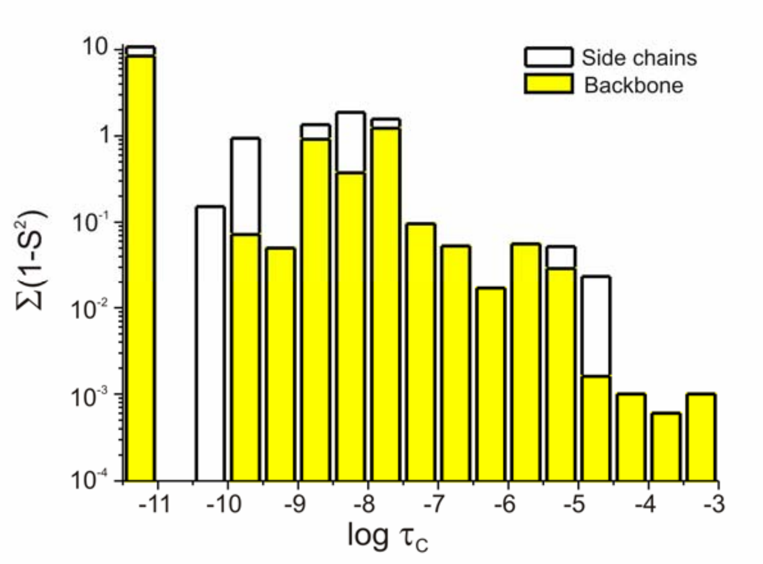

24. *Sum of amplitudes vs. correlation times. Best fitting results. Alternative minimization protocol (minimization with a function expressed by Eq.* (6.11)*)*

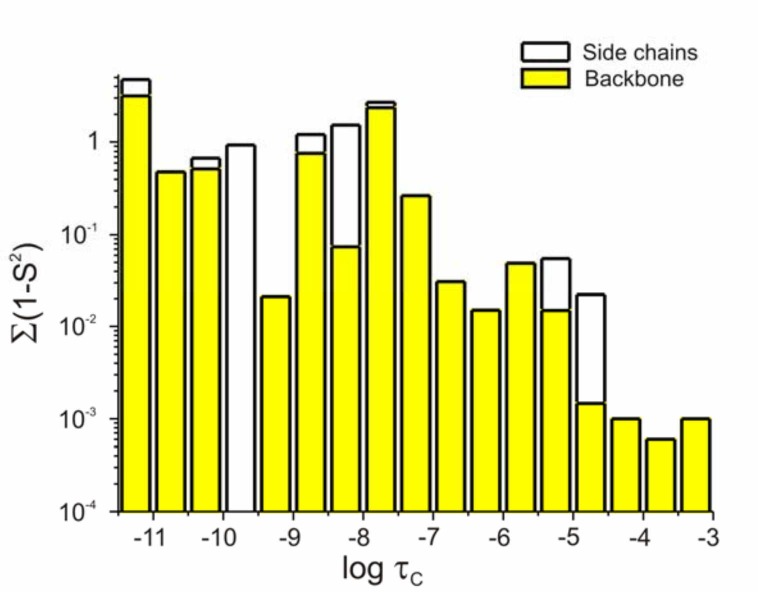

25. *Sum of amplitudes vs. correlation times. "Two motions with distribution". Alternative minimization protocol (from minimization with a function expressed by Eq.* (6.11)*)*

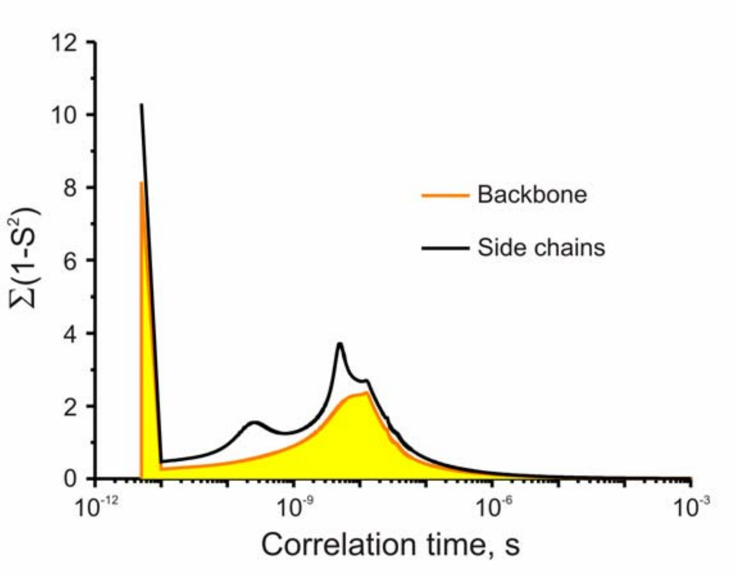

Bibliography

(1) Lange, O. F.; Lakomek, N.-A.; Farès, C.; Schröder, G. F.; Walter, K. F. A; Becker, S.; Meiler, J.; Grubmüller, H.; Griesinger, C.; De Groot, B. L. *Science* **2008**, *320*, 1471–1475.

(2) Gaspari, Z.; Perczel, A. *Annu. Rep. NMR Spectrosc.* **2010**, *71*, 35–75.

(3) Halle, B. *Proc. Natl. Acad. Sci. U. S. A.* **2002**, *99*, 1274–1279.

(4) Henzler-Wildman, K.; Kern, D. *Nature* **2007**, *450*, 964–972.

(5) Henzler-Wildman, K. A; Lei, M.; Thai, V.; Kerns, S. J.; Karplus, M.; Kern, D. *Nature* **2007**, *450*, 913–918.

(6) Parak, F. *Rep. Prog. Phys.* **2002**, *66*, 103-129.

(7) Kleckner, I. R.; Foster, M. P. *Biochim. Biophys. Acta* **2011**, *1814*, 942–968.

(8) Morin, S. *Prog. Nucl. Magn. Res. Spectrosc.* **2011**, *59*, 245–262.

(9) Ringe, D.; Petsko, G. *Prog. Biophys. Mol. Bio.* **1985**, *45*, 197–235.

(10) Williams, J. C.; McDermott, A. E. *Biochemistry* **1995**, *34*, 8309–8319.

(11) Rozovsky, S.; McDermott, A. E. *J. Mol. Biol* **2001**, *310*, 259–270.

(12) Toofanny, R. D.; Daggett, V. *WIRs: Comput. Mol. Sci.* **2012**, *2*, 405–423.

(13) Fisette, O.; Lagüe, P.; Gagné, S.; Morin, S. *J. Biomed. Biotechnol.* **2012**, 254208.

(14) Karplus, M. *Biopolymers* **2003**, *68*, 350–358.

(15) Xu, J.; Xue, Y.; Skrynnikov, N. R. *J. Biomol. NMR* **2009**, *45*, 57–72.

(16) Zhang, Q.; Sun, X.; Watt, E. D.; Al-Hashimi, H. M. *Science* **2006**, *311*, 653–656.

(17) Tolman, J. R. *J. Am. Chem. Soc.* **2002**, *124*, 12020–12030.

(18) Peti, W.; Meiler, J.; Brüschweiler, R.; Griesinger, C. *J. Am. Chem. Soc.* **2002**, *124*, 5822–5833.

(19) Bouvignies, G.; Bernadó, P.; Blackledge, M. *J. Magn. Reson.* **2005**, *173*, 328–338.

(20) Giraud, N.; Blackledge, M.; Böckmann, A.; Emsley, L. *J. Magn. Reson.* **2007**, *184*, 51–61.

(21) Blackledge, M. *Prog. Nucl. Magn. Res. Spectrosc.* **2005**, *46*, 23–61.

(22) Tolman, J. R.; Ruan, K. *Chem. Rev.* **2006**, *106*, 1720–1736.

(23) Guerry, P.; Salmon, L.; Mollica, L.; Ortega Roldan, J.-L.; Markwick, P.; Van Nuland, N. A. J.; McCammon, J. A.; Blackledge, M. *Angew. Chem. Int. Ed.* **2013**, *52*, 3181–3185.

(24) Chevelkov, V.; Rehbein, K.; Diehl, A.; Reif, B. *Angew. Chem. Int. Ed.* **2006**, *45*, 3878–3881.

(25) Castellani, F.; van Rossum, B.; Diehl, A. *Nature* **2002**, *420*, 98–102.

(26) Franks, W. T.; Zhou, D. H.; Wylie, B. J.; Money, B. G.; Graesser, D. T.; Frericks, H. L.; Sahota, G.; Rienstra, C. M. *J. Am. Chem. Soc.* **2005**, *127*, 12291–12305.

(27) Marulanda, D.; Tasayco, M. L.; Cataldi, M.; Arriaran, V.; Polenova, T. *J. Phys. Chem. B* **2005**, *109*, 18135–18145.

(28) Zech, S. G.; Wand, J. A.; McDermott, A. E. *J. Am. Chem. Soc.* **2005**, *127*, 8618–8626.

(29) Baldus, M. *Prog. Nucl. Magn. Res. Spectrosc* **2002**, *41*, 1–47.

(30) Cole, H. B. R.; Torchia, D. A. *Chem. Phys.* **1991**, *158*, 271–281.

(31) Veshtort, M.; Griffin, R. G. *J. Magn. Reson.* **2006**, *178*, 248–282.

(32) Ball, P. *Chem. Rev.* **2008**, *108*, 74–108.

(33) Helms, V. *Chem. Phys. Chem.* **2007**, *8*, 23–33.

(34) Bone, S.; Pethig, R. *J. Mol. Biol.* **1985**, *181*, 323–326.

(35) Mallamace, F.; Corsaro, C.; Baglioni, P.; Fratini, E.; Chen, S.-H. *J. Phys.: Condens. Matter* **2012**, *24*, 064103.

(36) Chevelkov, V.; Faelber, K.; Diehl, A.; Heinemann, U.; Oschkinat, H.; Reif, B. *J. Biomol. NMR* **2005**, *31*, 295–310.

(37) Jansson, H.; Bergman, R.; Swenson, J. *J. Phys. Chem. B* **2005**, *109*, 24134–24141.

(38) Halle, B.; Davidovic, M. *Proc. Natl. Acad. Sci. U. S. A.* **2003**, *100*, 12135–12140.

(39) Zanotti, J. M.; Bellissent-Funel, M. C.; Parello, J. *Biophys. J.* **1999**, *76*, 2390–2411.

(40) Chen, S.-H.; Liu, L.; Fratini, E.; Baglioni, P.; Faraone, A.; Mamontov, E. *Proc. Natl. Acad. Sci. U. S. A.* **2006**, *103*, 9012–9016.

(41) Roh, J. H.; Curtis, J. E.; Azzam, S.; Novikov, V. N.; Peral, I.; Chowdhuri, Z.; Gregory, R. B.; Sokolov, A. P. *Biophys. J.* **2006**, *91*, 2573–2588.

(42) Rupley, J. A.; Gratton, E.; Careri, G. *Trends Biochem. Sci.* **1983**, *8*, 18–22.

(43) Pérez, J.; Zanotti, J.-M.; Durand, D. *Biophys. J.* **1999**, *77*, 454–469.

(44) Yang, P.-H.; Rupley, J. A. *Biochemistry* **1979**, *18*, 2654–2661.

(45) Careri, G.; Giansanti, A.; Gratton, E. *Biopolymers* **1979**, *18*, 1187–1203.

(46) Careri, G.; Gratton, E.; Yang, P.-H.; Rupley, J. A. *Nature* **1980**, *284*, 572–573.

(47) Wüthrich, K. *Acta Crystallogr. D* **1995**, *51*, 249–270.

(48) Makinen, M. W.; Fink, A. L. *Annu. Rev. Biophys. Bioeng.* **1977**, *6*, 301–343.

(49) Drabkin, D. *J. Biol. Chem.* **1950**, *160*, 231–245.

(50) Chen, L.; Rydel, T. J.; Gu, F.; Dunaway, C. M.; Pikul, S.; Dunham, K. M.; Barnett, B. L. *J. Mol. Biol.* **1999**, *293*, 545–557.

(51) Tilton, R. F.; Dewan, J. C.; Petsko, G. A. *Biochemistry* **1992**, *31*, 2469–2481.

(52) Svensson, L. A.; Sjölin, L.; Gilliland, G. L.; Finzel, B. C.; Wlodawer, A. *Proteins* **1986**, *1*, 370–375.

(53) Yang, J.; Tasayco, M. L.; Polenova, T. *J. Am. Chem. Soc.* **2009**, *131*, 13690–13702.

(54) Chevelkov, V.; Xue, Y.; Linser, R.; Skrynnikov, N. R.; Reif, B. *J. Am. Chem. Soc.* **2010**, *132*, 5015–5017.

(55) Agarwal, V.; Xue, Y.; Reif, B.; Skrynnikov, N. R. *J. Am. Chem. Soc.* **2008**, *130*, 16611–16621.

(56) Torchia, D. A. *Annu. Rev. Biophys. Bioeng.* **1984**, *13*, 125–144.

(57) McDermott, A. E. *Curr. Opin. Struc. Biol.* **2004**, *14*, 554–561.

(58) Schanda, P.; Huber, M.; Boisbouvier, J.; Meier, B. H.; Ernst, M. *Angew. Chem. Int. Ed.* **2011**, *50*, 11005–11009.

(59) Lorieau, J. L.; McDermott, A. E. *J. Am. Chem. Soc.* **2006**, *128*, 11505–11512.

(60) Tollinger, M.; Sivertsen, A. C.; Meier, B. H.; Ernst, M.; Schanda, P. *J. Am. Chem. Soc.* **2012**, *134*, 14800–14807.

(61) Diakova, G.; Goddard, Y. A.; Korb, J.-P.; Bryant, R. G. *J. Magn. Reson.* **2007**, *189*, 166–172.

(62) Paciaroni, A.; Cinelli, S.; Cornicchi, E.; Francesco, A.; Onori, G. *Chem. Phys. Let.* **2005**, *410*, 400–403.

(63) Duer, M. *Introduction to solid-state NMR spectroscopy*; Blackwell Science: Oxford, 2004; p. 349.

(64) Schmidt-Rohr, K.; Spiess, H. W. *Multidimensional Solid-state NMR and Polymers*; Academic Press Inc.: San Diego, 1996; p. 478.

(65) Suter, D.; Ernst, R. R. *Phys. Rev. B* **1985**, *32*, 5608–5627.

(66) Dumez, J.-N.; Halse, M. E.; Butler, M. C.; Emsley, L. *Phys. Chem. Chem. Phys.* **2012**, *14*, 86–89.

(67) Kubo, A.; McDowell, C. A. *J. Chem. Soc., Faraday Trans. 1* **1988**, *84*, 3713-3730.

(68) Krushelnitsky, A.; Bräuniger, T.; Reichert, D. *J. Magn. Reson.* **2006**, *182*, 339–342.

(69) Levitt, M. H. *Spin Dynamics: basics of nuclear magnetic resonance*; John Wiley & sons, ltd: west sussex, 2008; p. 714.

(70) Gor'kov, P.; Witter, R.; Chekmenev, E.; Nozirov, F.; Fu, R.; Brey, W. W. *J. Magn. Reson.* **2007**, *189*, 182–189.

(71) Gerstein, B. C.; Chow, C.; Pembleton, R. G.; Wilson,. R. C. *J. Phys. Chem.* **1977**, *81*, 565–570.

(72) Hohwy, M.; Rasmussen, J. T.; Bower, P. V.; Jakobsen, H. J.; Nielsen, N. C. *J. Magn. Reson.* **1998**, *133*, 374–378.

(73) Waugh, J. S.; Huber, L. M.; Haeberlen, U. *Phys. Rev. Let.* **1968**, *20*, 180–183.

(74) Vinogradov, E.; Madhu, P. K.; Vega, S. *Chem. Phys Let.* **2002**, *354*, 193–202.

(75) Marchetti, A.; Jehle, S.; Felletti, M.; Knight, M. J.; Wang, Y.; Xu, Z.-Q.; Park, A. Y.; Otting, G.; Lesage, A.; Emsley, L.; Dixon, N. E.; Pintacuda, G. *Angew. Chem. Int. Ed.* **2012**, *51*, 10756–10759.

(76) Reif, B. *J. Magn. Reson.* **2012**, *216*, 1–12.

(77) Reif, B.; Jaroniec, C. P.; Rienstra, C. M.; Hohwy, M.; Griffin, R. G. *J. Magn. Reson.* **2001**, *151*, 320–327.

(78) Zheng, L.; Fishbein, K. W.; Griffin, R. G.; Herzfeld, J. *J. Am. Chem. Soc.* **1993**, *115*, 6254–6261.

(79) Reif, B.; Griffin, R. G. *J. Magn. Reson.* **2003**, *160*, 78–83.

(80) Chevelkov, V.; Van Rossum, B. J.; Castellani, F.; Rehbein, K.; Diehl, A.; Hohwy, M.; Steuernagel, S.; Engelke, F.; Oschkinat, H.; Reif, B. *J. Am. Chem. Soc.* **2003**, *125*, 7788–7789.

(81) McDermott, A. E.; Creuzet, F. J.; Kolbert, A. C.; Griffin, R. G. *J. Magn. Reson.* **1992**, *98*, 408–413.

(82) Zhou, D. H.; Graesser, D. T.; Franks, W. T.; Rienstra, C. M. *J. Magn. Reson.* **2006**, *178*, 297–307.

(83) Barnes, A. B.; De Paëpe, G.; Van der Wel, P. C. A.; Hu, K.-N.; Joo, C.-G.; Bajaj, V. S.; Mak-Jurkauskas, M. L.; Sirigiri, J. R.; Herzfeld, J.; Temkin, R. J.; Griffin, R. G. *Appl. Magn. Reson.* **2008**, *34*, 237–263.

(84) Maly, T.; Debelouchina, G. T.; Bajaj, V. S.; Hu, K.-N.; Joo, C.-G.; Mak-Jurkauskas, M. L.; Sirigiri, J. R.; Van der Wel, P. C. A.; Herzfeld, J.; Temkin, R. J.; Griffin, R. G. *J. Chem. Phys.* **2008**, *128*, 052211.

(85) Shore, S. E.; Ansermet, J.-P.; Slichter, C. P.; Sinfelt, J. H. *Phys. Rev. Let.* **1987**, *58*, 953–956.

(86) Gullion, T.; Schaefer, J. *J. Magn. Reson.***1989**, *81*, 196–200.

(87) Hong, M.; Gross, J. D.; Griffin, R. G. *J. Phys. Chem. B* **1997**, *101*, 5869–5874.

(88) deAzevedo, E. R.; Hu, W.-G.; Bonagamba, T. J.; Schmidt-Rohr, K. *J. Am. Chem. Soc.* **1999**, 8411–8412.

(89) Li, W.; McDermott, A. *J. Magn. Reson.* **2012**, *222*, 74–80.

(90) Li, W.; McDermott, A. E. *J. Biomol. NMR* **2009**, *45*, 227–232.

(91) Reichert, D.; Zimmermann, H.; Tekely, P.; Poupko, R.; Luz, Z. *J. Magn. Reson.* **1997**, *125*, 245–258.

(92) Kurbanov, R.; Zinkevich, T.; Krushelnitsky, A. *J. Chem. Phys.* **2011**, *135*, 184104.

(93) Krushelnitsky, A.; Kurbanov, R.; Reichert, D.; Hempel, G.; Schneider, H.; Fedotov, V. *Solid State Nucl. Magn. Reson.* **2002**, *22*, 423–438.

(94) Torchia, D. A.; Szabo, A. *J. Magn. Reson.* **1982**, *49*, 107–121.

(95) Daragan, V. A.; Mayo, K. H. *Prog. Nucl. Magn. Res. Spectrosc* **1997**, *31*, 63–105.

(96) Krushelnitsky, A.; Reichert, D. *Prog. Nucl. Magn. Res. Spectrosc* **2005**, *47*, 1–25.

(97) Torchia, D. A. *J. Magn. Reson.* **1978**, *30*, 613–616.

(98) VanderHart, D. L.; Garroway, A. N. *J. Chem. Phys.* **1979**, *71*, 2773–2787.

(99) Akasaka, K.; Ganapathy, S.; McDowell, C. A.; Naito, A. *J. Chem. Phys.* **1983**, *78*, 3567–3572.

(100) Tekely, P.; Canet, D.; Delpuech, J.-J.; Virlet, J. *Magn. Reson. Chem.* **1990**, *28*, 10–14.

(101) Oas, T. G.; Griffin, R. G.; Levitt, M. H. *J. Chem. Phys.* **1988**, *89*, 692-695.

(102) Quinn, C. M.; McDermott, A. E. *J. Biomol. NMR* **2009**, *45*, 5–8.

(103) Lipari, G.; Szabo, A. *J. Am. Chem. Soc.* **1982**, *104*, 4559–4570.

(104) Lipari, G.; Szabo, A. *J. Am. Chem. Soc.* **1982**, *104*, 4546–4559.

(105) Krushelnitsky, A. G.; Hempel, G.; Reichert, D. *Biochim. Biophys. Acta* **2003**, *1650*, 117–127.

(106) Beckmann, P. A. *Phys. Rep.* **1988**, *171*, 85–128.

(107) Schneider, H. *J. Polym. Sci. Pol. Phys.* **1991**, *29*, 1171–1177.

(108) Kroenke, C. D.; Loria, J. P.; Lee, L. K.; Rance, M.; Palmer, A. G. *J. Am. Chem. Soc.* **1998**, *120*, 7905–7915.

(109) Dayie, K. T.; Wagner, G.; Lefèvre, J. F. *Annu. Rev. Phys. Chem.* **1996**, *47*, 243–282.

(110) Palmer, A. *Annu. Rev. Biophys. Biomol. Struc.* **2001**, *30*, 129–155.

(111) Palmer, A. G.; Kroenke, C. D.; Loria, J. P. *Methods in enzymology* **2001**, *339*, 204–239.

(112) Blears, D. J.; Danyluk, S. S. *Biochim. Biophys. Acta* **1968**, *154*, 17–27.

(113) Andrew, E. R.; Gaspar, J. R.; Vennart, W. *Biopolymers* **1978**, *17*, 1913–1925.

(114) Andrew, E. R.; Bone, D. N.; Bryant, D. J.; Cashell, E. M.; Gaspar, R. J.; Meng, Q. A. *Pure Appl. Chem.* **1982**, *54*, 585–594.

(115) Gaspar, R. J.; Andrew, E. R.; Bryant, D. J.; Cashell, E. M. *Chem. Phys. Let.* **1982**, *86*, 327–330.

(116) Buszko, M. L.; Andrew, E. R. *Solid State Nucl. Magn. Reson.* **1992**, *1*, 115–119.

(117) Andrew, E. R.; Jurga, K.; Radomski, J. M.; Reynhardt, E. C. *Solid State Nucl. Magn. Reson.* **1992**, *1*, 121–5.

(118) Andrew, E. R.; Radomski, J. M. *Solid State Nucl. Magn. Reson.* **1993**, *2*, 57–60.

(119) Mack, J. W.; Usha, M. G.; Long, J.; Griffin, R. G.; Wittebort, R. J. *Biopolymers* **2000**, *53*, 9–18.

(120) Yoshioka, S.; Aso, Y.; Kojima, S. *J. Pharm. Sci.* **2002**, *91*, 2203–2210.

(121) Fedotov, V. D.; Obuchov, N. P.; Zadikhanov, R. A.; Spevacek, J.; Straka, J. *Appl. Magn. Reson.* **1993**, *4*, 491–511.

(122) Krushelnitsky, A.; Reichert, D. *Appl. Magn. Reson.* **2004**, *27*, 501–518.

(123) Huster, D.; Xiao, L.; Hong, M. *Biochemistry* **2001**, *40*, 7662–7674.

(124) Krushelnitsky, A.; Reichert, D.; Hempel, G.; Fedotov, V.; Schneider, H.; Yagodina, L.; Schulga, A. *J. Magn. Reson.* **1999**, *138*, 244–255.

(125) Lewandowski, J. R.; Sein, J.; Sass, H. J.; Grzesiek, S.; Blackledge, M.; Emsley, L. *J. Am. Chem. Soc.* **2010**, *132*, 8252–8254.

(126) Chevelkov, V.; Fink, U.; Reif, B. *J. Am. Chem. Soc.* **2009**, *131*, 14018–14022.

(127) Chevelkov, V.; Diehl, A.; Reif, B. *J. Chem. Phys.* **2008**, *128*, 052316.

(128) Giraud, N.; Blackledge, M.; Goldman, M.; Böckmann, A.; Lesage, A.; Penin, F.; Emsley, L. *J. Am. Chem. Soc.* **2005**, *127*, 18190–18201.

(129) Chevelkov, V.; Fink, U.; Reif, B. *J. Biomol. NMR* **2009**, *45*, 197–206.

(130) Chevelkov, V.; Zhuravleva, A. V; Xue, Y.; Reif, B.; Skrynnikov, N. R. *J. Am. Chem. Soc.* **2007**, *129*, 12594–12595.

(131) Lewandowski, J. R.; Sass, H. J.; Grzesiek, S.; Blackledge, M.; Emsley, L. *J. Am. Chem. Soc.* **2011**, *133*, 16762–16765.

(132) Schanda, P.; Meier, B. H.; Ernst, M. *J. Am. Chem. Soc.* **2010**, *132*, 15957–15967.

(133) Mollica, L.; Baias, M.; Lewandowski, J. R.; Wylie, B. J.; Sperling, L. J.; Rienstra, C. M.; Emsley, L.; Blackledge, M. *J. Phys. Chem. Lett.* **2012**, *3*, 3657–3662.

(134) Giraud, N.; Böckmann, A.; Lesage, A.; Penin, F.; Blackledge, M.; Emsley, L. *J. Am. Chem. Soc.* **2004**, *126*, 11422–11423.

(135) Clore, G. M.; Szabo, A.; Bax, A.; Kay, L. E.; Driscoll, P. C.; Gronenborn, A. M. *J. Am. Chem. Soc.* **1990**, *112*, 4989–4991.

(136) DeAzevedo, E. R.; Kennedy, S. B.; Hong, M. *Chem. Phys. Lett.* **2000**, *321*, 43–48.

(137) Kennedy, S. B.; DeAzevedo, E. R.; Petka, W. A.; Russell, T. P.; Tirrell, D. A.; Hong, M. *Macromolecules* **2001**, *34*, 8675–8685.

(138) Krushelnitsky, A.; DeAzevedo, E.; Linser, R.; Reif, B.; Saalwächter, K.; Reichert, D. *J. Am. Chem. Soc.* **2009**, *131*, 12097–12099.

(139) Kossiakoff, A. A.; Randal, M.; Guenot, J.; Eigenbrot, C. *Proteins* **1992**, *14*, 65–74.

(140) Jacobson, M. P.; Friesner, R. A.; Xiang, Z.; Honig, B. *J. Mol. Biol.* **2002**, *320*, 597–608.

(141) Hill, J. J.; Shalaev, E. Y.; Zografi, G. *J. Pharm. Sci.* **2005**, *94*, 1636–1667.

(142) Schinkel, J. E.; Downer, N. W.; Rupley, J. A. *Biochemistry* **1985**, *24*, 352–366.

(143) Lusceac, S. A.; Vogel, M. R.; Herbers, C. R. *Biochim. Biophys. Acta* **2010**, *1804*, 41–48.

(144) Separovic, F.; Lam, Y. H.; Ke, X.; Chan, H.-K. *Pharm. Res.* **1998**, *15*, 1816–1821.

(145) Kurkal, V.; Daniel, R. M.; Finney, J. L.; Tehei, M.; Dunn, R. V.; Smith, J. C. *Chem. Phys.* **2005**, *317*, 267–273.

(146) Bone, S.; Pethig, R. *J. Mol. Biol.* **1982**, *157*, 571–575.

(147) Krushelnitsky, A.; Faizullin, D.; Reichert, D. *Biopolymers* **2004**, *73*, 1–15.

(148) Krushelnitsky, A.; Zinkevich, T.; Mukhametshina, N.; Tarasova, N.; Gogolev, Y.; Gnezdilov, O.; Fedotov, V.; Belton, P.; Reichert, D. *J. Phys. Chem. B* **2009**, *113*, 10022–10034.

(149) McIntosh, L. P.; Wand, A. J.; Lowry, D. F.; Redfield, A. G.; Dahlquist, F. W. *Biochemistry* **1990**, *29*, 6341–6362.

(150) Sun, T. X.; Das, B. K.; Liang, J. J.-N. *J. Biol. Chem.* **1997**, *272*, 6220–6225.

(151) Aliev, A. E.; Harris, K. D. M. *Magn. Reson. Chem.* **1994**, *32*, 366–369.

(152) Kennedy, S. D.; Bryant, R. G. *Biopolymers* **1990**, *29*, 1801–1806.

(153) Gregory, R. B.; Gangoda, M.; Gilpin, R. K.; Su, W. *Biopolymers* **1993**, *33*, 513–519.

(154) Perry, A.; Stypa, M. P.; Tenn, B. K.; Kumashiro, K. K. *Biophys. J.* **2002**, *82*, 1086–1095.

(155) Carver, J. A. *Prog. Retin. Eye Res.* **1999**, *18*, 431–462.

(156) Hackel, C.; Zinkevich, T.; Belton, P.; Achilles, A.; Reichert, D.; Krushelnitsky, A. *Phys. Chem. Chem. Phys.* **2012**, *14*, 2727–2734.

(157) Reichert, D.; Hempel, G.; Zimmermann, H.; Tekely, P.; Poupko, R.; Luz, Z.; Favres, D. E.; Chmelka, B. F. *Appl. Magn. Reson.* **1999**, *17*, 315–327.

(158) Griebenow, K.; Klibanov, A. M. *Proc. Natl. Acad. Sci. U. S. A.* **1995**, *92*, 10969–10976.

(159) Khodadadi, S.; Pawlus, S.; Sokolov, a P. *The journal of physical chemistry. B* **2008**, *112*, 14273–80.

(160) Krushelnitsky, A.; Zinkevich, T.; Reichert, D.; Chevelkov, V.; Reif, B. *J. Am. Chem. Soc.* **2010**, *132*, 11850–11853.

(161) Linser, R.; Fink, U.; Reif, B. *J. Magn. Reson.* **2008**, *193*, 89–93.

(162) Brueschweiler, R.; Wright, P. E. *J. Am. Chem. Soc.* **1994**, *116*, 8426–8427.

(163) Farès, C.; Qian, J.; Davis, J. H. *J. Chem. Phys.* **2005**, *122*, 194908.

(164) Yao, L.; Vögeli, B.; Ying, J.; Bax, A. *J. Am. Chem. Soc.* **2008**, *130*, 16518–16520.

(165) Zinkevich, T.; Chevelkov, V.; Reif, B.; Saalwächter, K.; Krushelnitsky, A. *J. Biomol. NMR* **2013.**

(166) Chekmenev, E. Y.; Zhang, Q.; Waddell, K. W.; Mashuta, M. S.; Wittebort, R. J. *J. Am. Chem. Soc.* **2004**, *126*, 379–384.

(167) Wylie, B. J.; Franks, W. T.; Rienstra, C. M. *The journal of physical chemistry. B* **2006**, *110*, 10926–10936.

(168) Hall, J. B.; Fushman, D. *Journal of the American Chemical Society* **2006**, *128*, 7855–7870.

(169) Wylie, B. J.; Sperling, L. J.; Frericks, H. L.; Shah, G. J.; Franks, W. T.; Rienstra, C. M. *J. Am. Chem. Soc.* **2007**, *129*, 5318–5319.

(170) Herzfeld, J.; Roberts, J. E.; Griffin, R. G. *J. Chem. Phys.* **1987**, *86*, 597-602

(171) Chang, S.-L.; Tjandra, N. *J. Magn. Reson.* **2005**, *174*, 43–53.

(172) Johnson, E.; Palmer, A. G.; Rance, M. *Proteins* **2007**, *66*, 796–803.

(173) Akaike, H. *IEEE Trans. Autom. Contr.* **1974**, *19*, 667–674.

(174) Karplus, M.; McCammon, J. A. *Crit. Rev. Biochem. Mol.* **1981**, *9*, 293–349.

(175) Yoshioka, S.; Aso, Y.; Kojima, S. *Pharm. Res.* **1996**, *13*, 926–930.

(176) Salmon, L.; Bouvignies, G.; Markwick, P.; Lakomek, N.; Showalter, S.; Li, D.-W.; Walter, K.; Griesinger, C.; Brüschweiler, R.; Blackledge, M. *Angew. Chem. Int. Ed.* **2009**, *48*, 4154–4157.

(177) Landau, L. D.; Lifshitz, E. M. *Quantum Mechanics: Non-Relativistic Theory.*; Butterworth-Heinemann, 1981; p. 689.

(178) Bak, M.; Nielsen, N. C. *J. Magn. Reson.* **1997**, *125*, 132–139.

Eidesstattliche Erklärung

Hiermit versichere ich, dass ich die vorliegende Arbeit selbständig und ohne fremde Hilfe verfasst und dabei nur die von mir angegebenen Quellen und Hilfsmittel benutzt habe. Die den benutzten Werken wörtlich oder inhaltlich entnommenen Stellen habe ich als solche kenntlich gemacht.

Die vorliegende Dissertation habe ich weder in der gegenwärtigen noch in einer anderen Fassung einer anderen wissenschaftlichen Einrichtung vorgelegt. Weiterhin bestätige ich hiermit, keine anderweitigen Promotionsversuche unternommen zu haben.

Curriculum vitae

Personal data

Name:	Dipl.-Phys. Tatiana Zinkevich (geb. Vilkova)
Anschrift:	Gr. Ulrichstraße 36 06108 Halle/Saale
Birthdate and -place:	10. April 1984, Kazan, Russia
Family status:	divorsed
Citizenship:	russian

Education

1991-1997	Primary and secondary school N49 (Kazan, Russia)
1997-2001	Physics and Mathematics Lyceum N131 (Kazan, Russia)
2001-2006	Kazan State University (Kazan, Russia). Graduation with the Master of Physics

Professional Activities:

2006-2008	Intern researcher in the Spin-Physics and Spin-Chemistry Laboratory of the Zavoisky Physical-Technical Institute (ZPhTI, Kazan, Russia)
2008-2009	Lecturer in the Electrical Systems and Network Department in Kazan State University of Energy (Kazan, Russia)
2008-2012	Junior researcher in the Spin-Physics and Spin-Chemistry Laboratory of the Zavoisky Physical-Technical Institute (ZPhTI, Kazan, Russia)
2011-till now	PhD student in the Institute of Physics (NMR group) of Martin-Luther University (Halle, Germany)

Acknowledgements

At this point, I would like to thank all the people who supported me during the last several years – all members of the NMR and Biophysics groups in Martin-Luther University.

First, I wish to express appreciation for the valuable contribution to Doctor Alexey Krushelnitsky. That wouldn’t have been possible for me to get here without his help. I would like to thank him for providing comprehensive and outstanding support when studying NMR basics and investigating molecular dynamics in proteins. I am especially thankful for his patience and willingness to share knowledge.

Also I am very grateful to Professor Kay Saalwächter for the practical and useful discussions and ideas. Moreover, his help in formatting of this thesis was enormous. Being an attentive and competent supervisor, he perfectly guided me through the challenges I was faced with.

Another person who was always ready to help was Doctor Detlef Reichert. I would like to express my special thanks for his manifold suggestions and assistance in solving problems and answering questions. His assistance in explanation of different physical processes made my research more productive and interesting. Moreover, he supported me in solving many organizational difficulties.

Invaluable help with technical and experimental difficulties was provided by Christiane Hackel. She is very friendly and has a sympathetic heart, making my operation of the spectrometer as smooth as possible. In addition, Christiane Hackel, Kerstin Schäler and Anja Achilles did all their best to make my residence here pleasant and relaxed. They were always ready to discuss any problems I faced with in my scientific life, along with private. I believe that without this assistance my staying here would have been difficult and joyless. Of course, many other members of NMR and Biophysics groups did what they could to support me morally. Thus, I’m thankful to all of them.

During my time working in Russia, Dr. Oleg Gnezdilov and Rauf Kurbanov helped me in my first steps in NMR spectroscopy. Oleg Gnezdilov gave me a helping hand in experimental part of the work, assisted in performance of first experiments. Rauf Kurbanov’s assistance made it possible to better understand the theory of relaxation process.

I wish to express special thanks to Joshua Damron who helped me to find proper formulation of my thoughts, and tried to do his best to improve my language skills.

Finally, I would like to thank my family and friends, especially Vaidas. Their suggestions, advice and unreserved support made me brave and enduring to finish my work.

List of publications:

[1]. Krushelnitsky, A., Mukhametshina, N., Gogolev, Y., Tarasova, N., Faizullin, D., Zinkevich, T., Gnezdilov, O., Fedotov, V. (2008) Subunit Mobility and the Chaperone Activity of Recombinant alphaB-Crystallin. *Open Biochem. J.*, **2**, 116-120, doi: 10.2174/1874091X00802010116.

[2]. Krushelnitsky, A., Zinkevich, T., Mukhametshina, N., Tarasova, N., Gogolev, Y., Gnezdilov, O., Fedotov, V., Belton, P., Reichert, D. (2009) C-13 and N-15 NMR Study of the Hydration Response of T4 Lysozyme and alpha B-Crystallin Internal Dynamics. *J.Phys. Chem. B*, **113**, 10022-10034, doi: 10.1021/jp900337x.

[3]. Krushelnitsky, A., Zinkevich, T., Reichert, D., Chevelkov, V., Reif, B. (2010) Microsecond Time Scale Mobility in a Solid Protein As Studied by the N-15 R-1 rho Site-Specific NMR Relaxation Rates. *J. Am. Chem Soc.*, **132**, 11850-11853, doi: 10.1021/ja103582n.

[4]. Kurbanov, R., Zinkevich, T., Krushelnitsky, A. (2011) The nuclear magnetic resonance relaxation data analysis in solids: General R-1/R-1 rho equations and the model-free approach. *J. Chem. Phys.*, **135**, doi: 10.1063/1.3658383.

[5]. Hackel, C., Zinkevich, T., Belton, P., Achilles, A., Reichert, D., Krushelnitsky, A. (2012) The trehalose coating effect on the internal protein dynamics. *Phys. Chem. Chem. Phys.*, **14**, 2727-2734, doi: 10.1039/c2cp23098d.

[6]. Reichert, D., Zinkevich, T., Saalwachter, K., Krushelnitsky, A. (2012) The relation of the X-ray B-factor to protein dynamics: insights from recent dynamic solid-state NMR data. *J. Biomol. Struc. Dyn.*, **30**, 617-627, doi: 10.1080/07391102.2012.689695.

[7]. Samiullah, M., Reichert, D., Zinkevich, T., Jörg Kressler. NMR Characterization of PEG Networks Synthesized by CuAAC Using Reactive Oligomers. Submitted in 2013.

[8]. Zinkevich, T., Chevelkov, V., Reif, B., Saalwächter, K., Krushelnitsky, A. Internal protein dynamics on ps to μs timescales as studied by multi-frequency ^{15}N solid-state NMR relaxation. *J. Biomol. NMR* Accepted in 2013.

Abstracts

The comprehensive analysis of the microcrystalline protein dynamics by solid-state NMR relaxation studies is presented on the basis of “model-free” approach. It was found that proteins undergo a wide range of internal motions, which can be divided into three time-scale domains: fast with the correlation time less than 10^{-10} s, intermediate in the range 10^{-9}-$2{\cdot}10^{-7}$ s, and slow with correlation times longer than 10^{-7} s. The latter, occurring between states with very different populations – ground and excited states, is assumed to be responsible for biologically relevant processes. All these motional regimes in the fully hydrated solid and native dissolved states are found to be practically the same. Thus, information derived from the solid-state experiments can be applied to exploring biological properties of globular proteins, which are natively surrounded by water molecules.

Die umfassenden Relaxationsuntersuchunngen der mikrokristallinen Proteindynamik werden auf der Basis des "modellfreien" Ansatzes mit Hilfe der Festkörper-NMR vorgestellt. Es wurde festgestellt, dass Proteine eine Vielzahl von internen Bewegungen aufweisen, die in drei Zeitskalen unterteilt werden können: Schnelle Bewegungen mit der Korrelationszeiten kleiner als 10^{-10} s, intermediäre Bewegungen im Bereich 10^{-9} - $2{\cdot}10^{-7}$ s, und langsame Bewegungen mit den Korrelationszeiten länger als 10^{-7} s. Die letzteren treten zwischen den Zuständen mit sehr unterschiedlichen Zustandsbesetzungen auf; einem Grund- und einem angeregten Zustand, und es wird angenommen, dass diese Bewegungen für biologisch relevante Prozesse verantwortlich sind. Alle Bewegungsbereiche im vollständig hydratisierten Protein und im nativen aufgelösten Zustand sind praktisch identisch. Informationen, die aus den Experimenten an Festkörpern gewonnenen wurden, können damit für die Untersuchungen biologischer Eigenschaften von mit Wassermolekülen umgebenen globulären Proteinen genutzt werden.

Keywords: solid-state NMR relaxation, protein, dynamics, hydration;
Festkörper NMR Relaxation, Protein, Dynamik, Hydratation.